Liquid Crystal Pretilt Angle Control

Mechanism, Electro-Optical Properties and Numerical Analysis

Wei-Ta Wu

Cartoon and cover design by KiKi Lin
ISBN: 978-94-0280-434-8
Printed by Ipskamp Drukkers, Enschede, The Netherlands

Liquid Crystal Pretilt Angle Control

Mechanism, Electro-Optical Properties and Numerical Analysis

Proefschrift

ter verkrijging van de graad van doctor
aan de Radboud Universiteit Nijmegen
op gezag van de rector magnificus prof. dr. J.H.J.M. van Krieken,
volgens besluit van het college van decanen
in het openbaar te verdedigen op donderdag 15 december 2016
om 13.30 uur precies

door

Wei-Ta Wu

geboren op 27 februari 1984
te Changhua, Taiwan

Promotoren: Prof. dr. Th.H.M. Rasing

Prof. dr. Ru-Pin Pan
(National Chiao Tung University, Taiwan)

Manuscriptcommissie:

Prof. dr. H.W.M. Salemink	
Prof. dr. D.J. Broer	Technische Universiteit Eindhoven
Prof. dr. I. Muševič	Inštitut Jožef Stefan, Slovenia

The work in this thesis was financially supported by the Marie-Curie Initial Training Network (ITN) Hierarchy, de Nederlandse Organisatie voor Wetenschappelijk Onderzoek (NWO), National Science Council of the Republic of China (NSC 99-2221-E-009-072- MY3), and Academia Sinica AS-98-TP-A10.

Preface

It is the time to write the last part of my thesis and thank people who contribute for this. On 28 April 2011, it was my first time to meet Theo. He came to Taiwan for a conference, and my Taiwanese boss, who is Theo's good friend Ru-Pin, invited him came to our lab to give a talk. In the next day, Theo asked me to come to join his group for 14 months as a visiting researcher. Surprisingly, we extended my contract every year and now it is the time to finish my thesis at Radboud University.

First of all, I would like to thank my promotor, prof. dr. Theo Rasing, who is a positive and high efficient supervisor. In every meeting and discussion, he always provided a lot of constructive feedback and useful suggestions. In spite of his busy schedule, he always found the time to correct and improve my thesis and publication writings. Theo, thank you to gave me the great freedom to decide and to do my LC studies. It is my great pleasure to work with you.

I am also very grateful to my Taiwanese promotor, prof. dr. Ru-Pin Pan. I started my LC studies with her in 2007 and got my master degree in her group. From her teaching, I learned much about liquid crystal. She enlightened and supported me in the experiments and my life.

Marilou, everyone knows your importance for our group. You always friendly answers my questions and solves them. Thanks for all your kind help for the administrative works and the problems in my life.

Here I would like to introduce the best technical group for the experimental supports of hardware and software. Albert and Sergey taught me how to operate AFM/MFM in my first year. Tonnie taught me how to use ellipsometer and helped me a lot to improve the sputtering machine. He also built the measurement system of electro-optical LC properties in our LC lab. Without all of you, no experimental data can be acquired and analyzed in my thesis.

Next, I would like to thank the manuscript committee prof. dr. H.W.M. Salemink, prof. dr. D.J. Broer and prof. dr. I. Muševič for the helpful comments and suggestions. Especially, Huub put a lot of effort into my thesis and the paper drafts. He urged me to think how to rewrite my manuscript logically and readably for general public.

Thank Andrei and Alexey for the help of magnetic studies, which is not written into this thesis. It is also my pleasure to work and discuss with Laura. She helped a lot with my experiments and the theatrical model, and she also made many improvements in this thesis.

For Taiwanese group, first I would like to thank for the collaborations with Meng-Chiou and Cheng-Wei. A large part of the samples and measurements in Ch. 4 and 5 was done with them. And also thanks for the discussions and ideas from Chao-Yu and Cho-Fan. Thanks Mel and Wen-Chen for English writing and grammar corrections.

I had a lot of fun to work with a big group of nice colleagues: Addis, Albert, Anna, Benny, Bowen, Chenghoon, Davide, Dennis, Diana, Dima, Erwin, Georgy, Ilya, Janas, Johan, Kiran, Lennert, Matteo, Remco, Rostislav, Sam, Sicong, Siebe, Thomas, Valera, Lar, Yulong , Yury, and Yusuke. Working with you will be wonderful memories in my life.

Finally, this thesis is dedicated to my family and I love you so much. Dear papa and mama, thank you for your unconditional Love. You always support and encourage me to do anything I want to do. To my brother GuanDa, it is a difficult period to live in such long distance to you and parents. Thanks for everything you did and the supports in Taiwan. My dear wife Lyn, you complete my life and thanks for your love and care. To lovely and full-energy sons Jimmy and Ray, papa loves you.

Wei-Ta Wu

Nijmegen, October 2016

Contents

CHAPTER 1

Introduction

Nowadays, liquid crystal displays (LCDs) are everywhere. In the office, LCDs provide large and flat screens on your desk to get better working conditions. At home, LCDs bring the possibility to enjoy a movie or play a video game with a large display and they are thin enough to hang on the wall. On the instruments in the laboratory, old pointer indicators are replaced by LCD panels. Moreover, the flatness and compactness of the LCDs and their low energy consumption make portable devices, such as laptop computers and smartphones, smaller and lighter, so you can have a movable office or personal entertainment on a train and an airplane. Despite the maturity of the LCD technology, there are still many points in their performances, such as switching speed, viewing angle and production cost, that can be improved. The latter requires both the development of new methods and a better understanding of the performance mechanisms, which is the motivation for the work described in this thesis.

In the early 70s, the application of LCDs was firstly introduced in segmented displays such as calculators and watches (see Fig. 1.1a) [1]. T. P. Brody et al. reported that every pixel can be driven independently for an active-matrix display by attaching a transistor and a capacitor on substrates of LC layers, to actively maintain the brightness state [2]. This development of active-matrix displays with thin film transistors (TFT) has brought great advances to produce higher resolution colorful LCDs (see Fig. 1.1b) because the sub-pixels can be controlled separately (see Fig. 1.1c). Scientists and engineers aim to design and fabricate an LCD with the lowest cost and the best performance, such as a high contrast ratio, a fast response time and a wide viewing angle. To achieve better performances, nowadays, many LCD modes

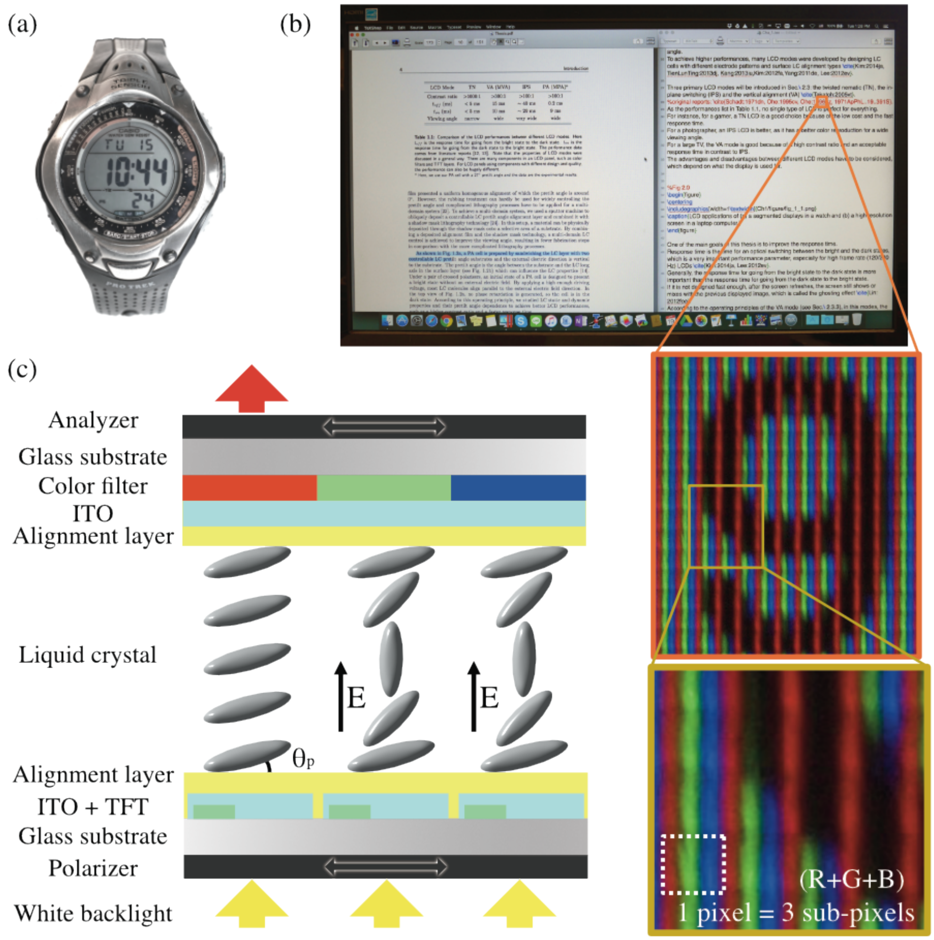

Figure 1.1: LCD applications of (a) a segmented displays in a watch and (b) a high resolution monitor. (c) Cross section of PA LCD layers structure of a single RGB pixel

are still being developed by designing LC cells with different electrode patterns and surface LC alignment types [3–7].

Most LCD modes are based on three primary LCD types: twisted nematic (TN), in-plane switching (IPS) and vertical alignment (VA) [8–10]; these three LCD types will be introduced in detail in Sec. 2.3. As the performances comparison shown in Table 1.1, no single type of LCD is perfect for everything. For instance, for a gamer, a TN LCD is a good choice because of the low cost and the fast response time.

LCD Mode	TN	VA (MVA)	IPS	PA (MPA)
Contrast ratio	>1000:1	>300:1	>100:1	>100:1
$t_{b\to d}$ (ms)	< 5 ms	15 ms	$\sim$ 40 ms	0.2 ms
$t_{d\to b}$ (ms)	< 5 ms	10 ms	$\sim$ 20 ms	9 ms
Viewing angle	narrow	wide	very wide	wide

Table 1.1: Comparison of the LCD performances between different LCD modes. Here $t_{b\to d}$ is the response time for going from the bright state to the dark state. $t_{d\to b}$ is the response time for going from the dark state to the bright state. The performance data comes from literature reports [11, 12]. A PA cell was prepared with a 27° pretilt angle and the data are our experimental results. Note that the properties of LCD modes were discussed in a general way. There are many components in an LCD panel, such as color filters and TFT layers (see Fig. 1.1c). For LCD panels using components with different design and quality, the performance can also be hugely different.

For a photographer, an IPS LCD is better, as it has a better color reproduction for a wide viewing angle. For a large TV, the VA mode is good because of a high contrast ratio and an acceptable response time in contrast to IPS. The advantages and disadvantages between different LCD modes have to be considered, which depend on what the display is used for.

The main goals of this thesis are to improve the contrast ratio, response time and viewing angle by controlling the pretilt angle, i.e. the orientation of the liquid crystal molecules with respect to the LC cell walls. To this aim, as described in Ch. 4, we have developed a new and quite simple method to control the pretilt angle in a wide range from 0° to 45° by depositing Fe_2O_3/Cr_2O_3 on a polyimide-coated substrate. In this thesis, as shown in Fig. 1.1c, we prepared PA cells by sandwiching the LC layer with two controllable LC pretilt angle substrates and the external electric direction is vertical to the substrate. Under a pair of crossed polarizers, an initial state of a PA cell is designed to present a bright state without an external electric field. By applying a high enough driving voltage, most LC molecules align parallel to the external electric field direction. No phase retardation is generated, so the cell is in the dark state. When removing the voltage, the elastic response of the LC medium brings it back to its original bright state. According to this operating principle, we studied LC static and dynamic properties and their pretilt angle dependence to achieve better LCD performances.

The response time is the time for the switching between the bright and the dark states of an LC cell, and is a very important performance parameter, especially for high frame rate (120/240 Hz) LCDs [13, 14]. Generally, the response time for going from the bright state to the dark state is more important than the response time for going from the dark state to the bright state. If it is not designed fast enough, after the screen refreshes, the screen still shows or mixes with the previous displayed image, which is called the ghosting effect [15]. In IPS and VA modes, the response time for going from the bright state to the dark state depends on the time that it takes for the LC molecules to relax back to the initial state after switching off the driving voltage. This response speed is limited by the elastic constants of the material. To overcome this limitation of the response speed, a vertically aligned in-plane-switching (VA-IPS) LCD mode was developed [16]. However, in this kind of in-plane switching mode, the brightness is reduced because the light is blocked by the electrodes and circuits which are designed on the same substrate. In Ch. 6, we will demonstrate a very fast response time ($t_{b\rightarrow d}$ = 0.2 ms) by preparing a parallel alignment (PA) cell with an optimum pretilt angle under a normail driving voltage (see Table 1.1). Comparing to the response times of IPS and VA modes, our PA mode is more suitable for high frame rate LCDs.

Moreover, we aim to design an LCD with a fast response and also a wider viewing angle. The viewing angle is usually defined as the maximum angle at which an LCD has an acceptable visual performance, such as the grayscale and the contrast ratio [17–19]. For compensating the viewing angle dependency of the individual pixels, multi-domain systems have been developed [20–22]. In a multi-domain system, a sub-pixel is divided into four or eight domains. The LC molecules align into different directions on different domains; the viewing angle dependence in each sub-pixel is compensated by averaging the transmittance over domains. Nowadays, a multi-domain vertical alignment (MVA) mode is mostly used in large TVs because it combines the advantages of the faster response time than IPS and the wider viewing angle than TN. By using the same method to compensate the viewing angle dependency as in an MVA, in Ch. 8, we demonstrate a dual-domain parallel alignment LCD based on our new developed alignment method to improve the viewing angle.

In Ch. 8, we used a sputtering machine with a shadow mask lithography technology to obliquely deposit a controllable LC pretilt angle alignment layer onto a selective area of a substrate [23]. A dual-domain LC pretilt angle control is achieved to get both fast response time and wider viewing angle.

Apart from the general LCD applications, such as TVs and laptops, we are also interested in some specific LCD applications. For a reflective black and white LCD watch, a low energy consumption and a driving voltage are more important to save the battery life and reduce the device size [24]. In this thesis, we found that a lower driving voltage is needed for a cell with a higher pretilt angle. This lower driving voltage cell maintains the same contrast ratio and response time compared to a cell with a lower pretilt angle which needs a higher driving voltage. The other specific LCD application is a welding goggle to protect eyes [25]. By detecting the light strength from the welding, an auto shade LCD goggle operates from the transparent state to the blocked state. To protect eyes by preventing a strong exposure during a welding procedure, the key point of this type of LCD is how fast it can be switched to the blocked state. In a PA cell, a high blocking (> 99.91%) and fast response (60 µs) welding goggle can be designed by preparing an LC cell with a ∼25° pretilt angle and a 15 V switching voltage. In addition, to apply the same driving voltage, a cell with a high pretilt angle can have a five times shorter blocking time than a cell with a low pretilt angle.

The theoretical modeling for the observed effects is also an important part of this thesis. A reliable theoretical analysis is crucial to find suitable cell conditions and optimum parameters for the best LCD performance [26, 27]. Also, a proper theoretical study can help us to explain the observed LC effects and confirm experimental results. So far, the existing theoretical analysis of the LCD effects is limited by using computer simulations or calculations using a small angle approximation [28–30]. In Ch. 7, we developed a new calculation method which uses the full LC tilt angle range instead of the small angle approximation and derived the free energy equation with the crossed terms neglected method. This new calculation method can give the static and dynamic LC director distribution for all angles. Moreover, this calculation result shows excellent agreements with the experiments of the pretilt angle dependence shown in Ch. 6. The calculation also gives the explanations of some LC effects, such as the threshold voltage and the time delay of the optical response.

Scope of the thesis

Chapter 2 gives an introduction to LCs and LCDs. We start with a background introduction of LC molecules and their phases. Next, the LC electro-optical properties, from the birefringence to the transmittance, are explained in detail. The theory of curvature-elasticity in LCs is introduced, which is the base of our new calculation method. In the LCD introduction, the description of three typical LCD modes, TN, IPS and VA, briefly shows the role of LC molecules in LCDs and also gives a simple introduction how each type of LCD works. After presenting the advantage of the multi-domain vertical alignment mode, we describe several surface alignment technologies.

Chapter 3 presents all the relevant experimental setups and analytical methods in this thesis. It starts by describing in detail our sample preparation setup and fabrication. The LC texture observation, the pretilt angle and electro-optical effect measurements allow us to investigate the LC and LCD properties. The surface observation methods provide the possibilities for a nanometer-scale topography investigation, a compound identification and a quantitive surface composition analysis.

In Ch. 4, we demonstrate how to control the pretilt angle precisely with an obliquely deposited Fe_2O_3/Cr_2O_3 thin film on a polyimide-coated indium-tin-oxide (ITO) glass. In our study, the pretilt angle can be controlled continuously between

0° and 45° by varying the Fe_2O_3/Cr_2O_3 deposition times. The relation between the pretilt angle and sputtering conditions was also studied and analyzed.

In Ch. 5, we investigated the possible alignment mechanisms by Fe_2O_3/Cr_2O_3 and polyimide layers by studying the chemical and physical surface changes.

In Ch. 6, we use our controllable pretilt angle method to study the static and dynamic LC properties and their pretilt angle dependence. The experimental results showed that better performances, such as a higher contrast ratio and faster response time, was found in a cell with an optimum pretilt angle.

In Ch. 7, we developed a new calculation method which can present the static LC director distribution for all angles. The calculations regarding all the interesting phenomena investigated in Ch. 6 show excellent agreements with the experiments.

In Ch. 8, we prepared a dual-domain cell by combing our pretilt angle controllable method with a shadow mask lithography technology. A wider viewing angle was observed in a dual-domain PA cell in contrast to the single-domain PA cell.

Summarizing the thesis: after systematic studies of the LC properties, both with experiments and a new developed theoretical analysis, a high-performance LCD with a fast response time and a wide viewing angle (see Table 1.1), is achieved by using a dual-domain parallel alignment panel with an optimum pretilt angle.

References

[1] M. Schadt and W. Helfrich, Applied Physics Letters **18**, 127 (1971).

[2] T. P. Brody, F. C. Luo, and Z. P. Szepesi, Electron Devices (1975).

[3] J.-W. Kim, T.-H. Choi, and T.-H. Yoon, Liquid Crystals **41**, 1212 (2014).

[4] T.-L. Ting, C.-Y. Chen, S.-W. Tsao, M.-J. Lu, Y.-Y. Kung, W.-H. Hsu, and J.-J. Su, Journal of Display Technology **9**, 832 (2013).

[5] S.-W. Kang, Y. E. Choi, B. H. Lee, J. H. Lee, S. Kundu, H.-S. Jin, Y. K. Yun, S. H. Lee, and L. Komitov, Liquid Crystals **41**, 552 (2013).

[6] K.-H. Kim, E.-Y. Jeon, B. W. Park, S.-W. Choi, D. H. Song, H. Kim, K.-C. Shin, H. S. Kim, and T.-H. Yoon, Journal of the Optical Society of Korea **16**, 166 (2012).

[7] G. Yang and Y. Sun, Liquid Crystals **38**, 507 (2011).

[8] M. Oh-e and K. Kondo, Applied Physics Letters **67**, 3895 (1995).

[9] M. F. Schiekel and K. Fahrenschon, Applied Physics Letters **19**, 391 (1971).

[10] K. Takatoh, M. Hasegawa, M. Koden, N. Itoh, R. Hasegawa, and M. Sakamoto, *Alignment Technology and Applications of Liquid Crystal Devices* (CRC Press, 2005).

[11] Y. Koike and K. Okamoto, Fujitsu Science Technical Journal **35**, 221 (1999).

[12] M. Oh-e and K. Kondo, Applied Physics Letters **69**, 623 (1996).

[13] D. H. Kim, Y. J. Lim, D. E. Kim, H. Ren, S. H. Ahn, and S. H. Lee, Journal of Information Display **15**, 99 (2014).

[14] S. H. Lee, S. S. Bhattacharyya, H.-S. Jin, and K.-U. Jeong, Journal of Materials Chemistry **22**, 11893 (2012).

[15] C. C. Lin, C. Ye, H. L. Hou, C. Y. Lee, R. Xie, G. Chen, and F. Yang, SID Symposium Digest of Technical Papers **43**, 965 (2012).

[16] T.-L. Ting, C.-Y. Chen, S.-W. Tsao, M.-J. Lu, Y.-Y. Kung, W.-H. Hsu, and J.-J. Su, Journal of Display Technology **9**, 832 (2013).

[17] T. Ishinabe, K. Kusama, and S. Shoshi, ITE Transactions on Media Technology and Applications **4**, 34 (2016).

[18] H. Takemoto, T. Fuchida, and M. Miyatake, SID Symposium Digest of Technical Papers **40**, 514 (2009).

[19] Y.-J. Wang, J.-G. Lu, W.-C. Chao, and H.-P. D. Shieh, Optics express **23**, 21443 (2015).

[20] K. Koike, S. Takaoka, T. Sasaki, H. Chida, H. Tsuda, A. Takeda, and K. Ohmuro, Proceedings of AM-LCD , 25 (1997).

[21] M. Schadt, H. Seiberle, and A. Schuster, Nature (1996).

[22] Y.-K. Moon, Y.-J. Lee, C.-J. Yu, J. Uk Heo, J.-H. Park, H. jin Lee, S. Tae Shin, and J.-H. Kim, Journal of Applied Physics **112**, 014512 (2012).

[23] A. Tixier, Y. Mita, J. P. Gouy, and H. Fujita, Journal of Micromechanics and Microengineering **10**, 157 (2000).

[24] P. Yeh and C. Gu, *Optics of Liquid Crystal Displays* (John Wiley & Sons, 2010).

[25] T. N. McManus and A. N. Haddad, International Journal of Open Scientific Research **1**, 15 (2013).

[26] L. Weng, P.-C. Liao, C.-C. Lin, T.-L. Ting, W.-H. Hsu, J.-J. Su, and L.-C. Chien, AIP Advances **5**, 097218 (2015).

[27] X. Nie, H. Xianyu, R. Lu, T. X. Wu, and S.-T. Wu, Journal of Display Technology **3**, 280 (2007).

[28] D.-K. Yang and S.-T. Wu, *Fundamentals of Liquid Crystal Devices* (John Wiley & Sons, 2014).

[29] G. Meier, E. Sackmann, and J. G. Grabmaier, *Applications of Liquid Crystals* (Springer Science & Business Media, 2012).

[30] S.-T. Wu and C.-S. Wu, Applied Physics Letters **53**, 1794 (1988).

CHAPTER 2

Liquid Crystal Displays

2.1 Introduction

Liquid crystal displays (LCDs) are widely used for display applications because their optical properties can be easily controlled by an external electric field [1]. In general, a layer of liquid crystal (LC) molecules is sandwiched between a pair of crossed polarizers in an LCD. After passing through the LC layer, the polarization of the light is altered and then the transmittance is the percentage of the light passing through the second polarizer, also known as an analyzer. The transmittance is determined according to the cell structure and the LC director distribution [2]. The optical properties of an LC layer can be modified by reorienting the LC director distribution by applying an electric field. Based on an equilibrium between a surface alignment (initial state) and an external electric field, this can correspond to the bright and dark states in LCDs [3, 4].

The unique LC electro-optical properties play an important role in LCDs. This chapter provides a brief overview from the LC material to the LCD application. First, LC properties and the basic idea of the LCD operation are explained in Sec. 2.2. Several LCD technologies which had been developed for achieving higher performances are discussed in Sec. 2.3. In the last part, several surface alignment technologies are introduced in Sec. 2.4.

2.2 Liquid crystals

A liquid crystal is a well-known phase of matter which has properties between liquid and crystal phases [5]. According to the layer structure and chirality, liquid crystals

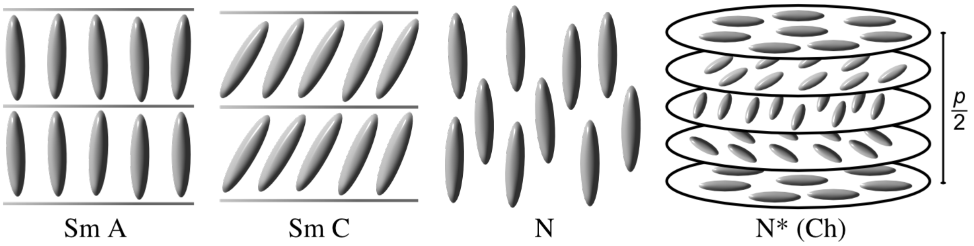

Figure 2.1: Structure of four typical LC phases, Smectic A (Sm A), Smectic C (Sm C), Nematic (N), and Chiral nematic (N*). The molecules of smectic phases are organized into layers. In the smectic A phase, the molecules align vertically to the layers. In the smectic C phase, the molecules tilt inside the layers. In a nematic phase, the molecules have no positional order, but have directional order. The chiral nematic phase, which is also called the cholesteric phase, exhibits a director that is twisted into a helix. The chiral pitch p refers to the distance over which the LC molecules make a 360° twist.

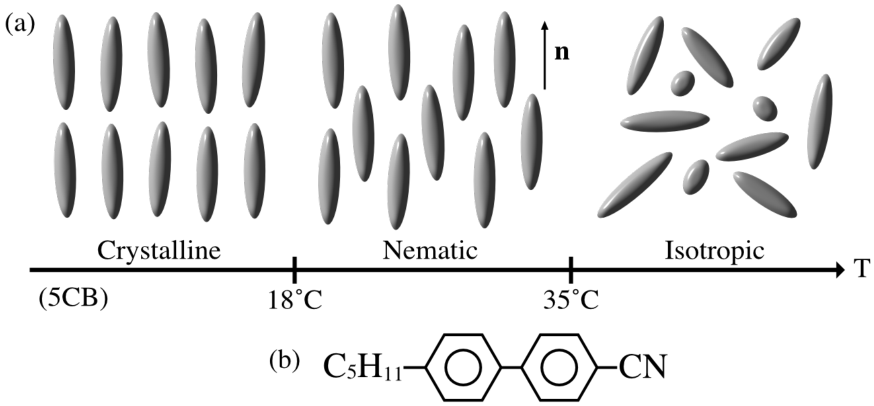

Figure 2.2: (a) Schematic representation and phase transition temperatures of a typical thermotropic nematic liquid crystal. Here we use the example of 5CB which goes from a crystalline to a nematic phase at 18°C and goes from a nematic to a isotropic phase at 35°C. The director **n** is the average orientation of the LC molecules. (b) The structural formula of 5CB.

are further classified into several types of mesophases, such as nematic, smectic, and cholesteric (see Fig. 2.1) [6]. The cholesteric phase was the first discovered liquid crystal by Friedrich Reinitzer in 1888 [7]. Nowadays, most of LCDs use the nematic liquid crystal which is described by Georges Friedel in 1922 [8]. In a nematic phase, molecules flow as a liquid, that means there is no positional order, but they tend to orient in the same direction called LC director $\mathbf{n}$ (see Fig. 2.2a) resulting in an orientational order with crystal-like properties such as birefringence.

The only molecule used in this thesis is 4'-n-pentyl-4-cyanobiphenyl (5CB, Merck) which is a typical thermotropic LC molecule firstly synthesized by Gray *et al* in 1973 [9]. As the structural formula shown in Fig. 2.2b indicates, 5CB is formed of a uniaxial rod-like molecule. With increasing temperature, 5CB goes from the crystalline, nematic, to the isotropic phase (see Fig. 2.2a). In this study, all the experiments of the 5CB cells were performed at room temperature of 25°C, which is in the nematic phase.[1]

In following sections, 5CB properties are basically introduced into three parts: (1) the LC orientation control via the balance between the surface alignment and the external electric field. (2) The optical properties from the LC birefringence to the transmittance. (3) The free energy model for the theoretical investigation.

---

[1] Note that though the 5CB molecule is non-centrosymmetric (see Fig. 2.2b), in the nematic phase the 5CB molecules are on average in an antiparallel arrangement. The director $\mathbf{n}$ is therefore not a vector and the schematic representation of the 5CB molecules in Fig. 2.2a actually represent pairs of antiparallel molecules. Here, $\mathbf{n} = -\mathbf{n}$.

2.2.1 Electric properties

In a parallel alignment (PA) cell (see Fig. 2.3a), the LC molecules are confined with two glass substrates. In our study, the glass substrate surface is coated with an indium tin oxide (ITO) layer as a transparent electrode and an LC planar alignment layer, in that order (see Fig. 2.3b).[2] The LC aligns horizontally without an external electric field (see 0 V cell of Fig. 2.3a). The 5CB molecule has a positive electrical permittivity due to the large dipole moment along the LC long axis from the cyano end group (see Fig. 2.2b) [10]. Because of the positive anisotropic electrical permittivity ($\Delta\epsilon = 10$), 5CB molecules prefer to align parallel to an external electric field. Two parallel ITO layers generate an electric field $\mathbf{E}$ in the normal direction of the substrate. The LC molecules align along the field with a high enough driving voltage (see high V_d cell of Fig. 2.3a). Based on this cell structure, the LC orientation can be controlled by the balance between the surface alignment (horizontal) and the external electric field (vertical).

2.2.2 Optical properties

A birefringent material has different refractive indices for different polarization and propagation directions of light [11]. As shown in Fig. 2.3e, the uniaxial symmetry of the 5CB molecule results in birefringence which is presented as two different refractive indices for the ordinary n_o and extraordinary rays n_e. Applying an external electric field, the effective refractive index n_{eff} for arbitrary LC tilt angle θ (see Fig. 2.3f) can be derived by the following equation [12].

$$n_{eff}(\theta) = (\frac{\cos^2\theta}{n_e^2} + \frac{\sin^2\theta}{n_o^2})^{-\frac{1}{2}} \tag{2.1}$$

Under a pair of crossed polarizers oriented over 45° with respect to the surface alignment direction (see Fig. 2.3a), the integration of the birefringence over the whole cell gives the phase retardation $\Delta\phi$ which can be written as

$$\Delta\phi = \int_0^d \Delta n_{eff}\; k\; dz \tag{2.2}$$

where $\Delta n_{eff} = n_o - n_{eff}$ and $k = 2\pi/\lambda$ is the wave number. As shown in Fig. 2.3c, the initial phase retardation is the maximum of the phase retardation which appears while all the LC molecules are aligned by a surface treatment ($V_d = 0$). As the driving voltage increases, the phase retardation decreases due to the reduction of the refractive indices difference Δn_{eff} for the high LC tilt angle. The phase retardation decreases

---

[2] If the LCD is used with a high resolution, the electrode layer has to be made with a TFT device to control the voltage of each sub-pixel. Moreover, each RGB sub-pixel has to be attached with a color filter to produce colorful images.

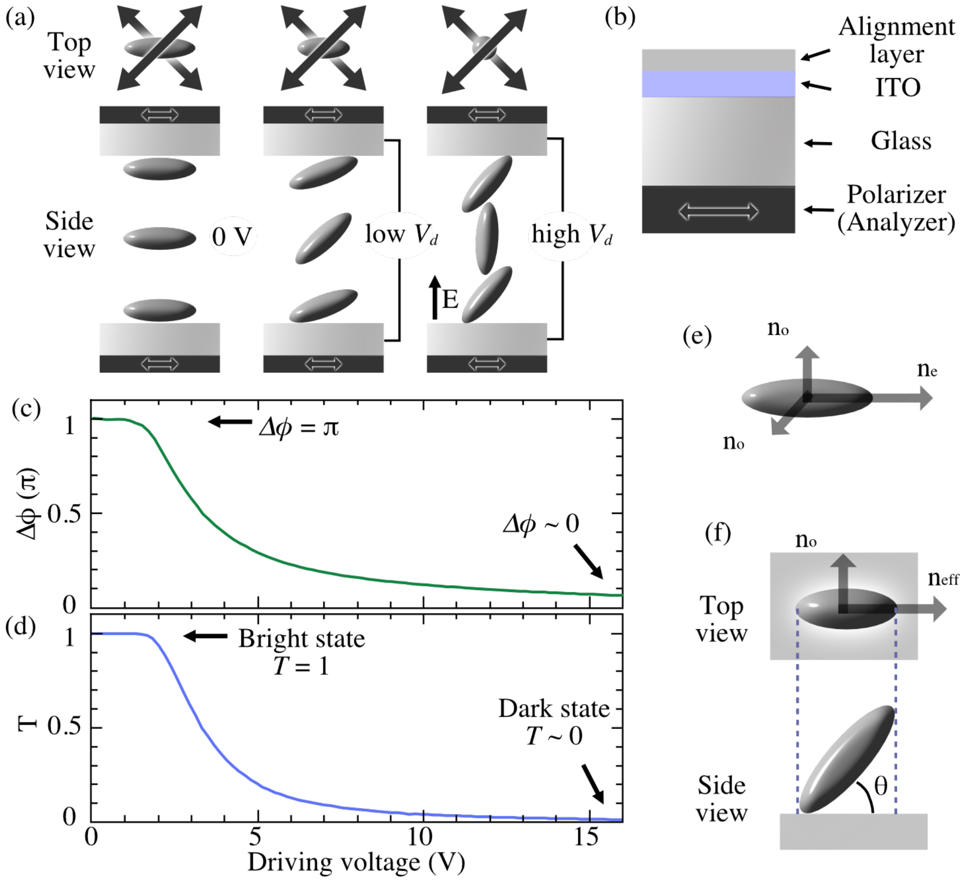

Figure 2.3: (a) The top and (b) side views of the schematic LC distribution under different driving voltages. Here the cell is demonstrated with a planar alignment and a vertical external electric field $\mathbf{E}$. (c) The phase retardation $\Delta\phi$ and (d) the transmittance T as a function of the driving voltage for the planar cell (rubbed PI sample). (e) The refractive indices in rod-like LC molecules for the ordinary n_o and extraordinary rays n_e. (f) The relation between the effective LC refractive index n_{eff} and tilt angle θ.

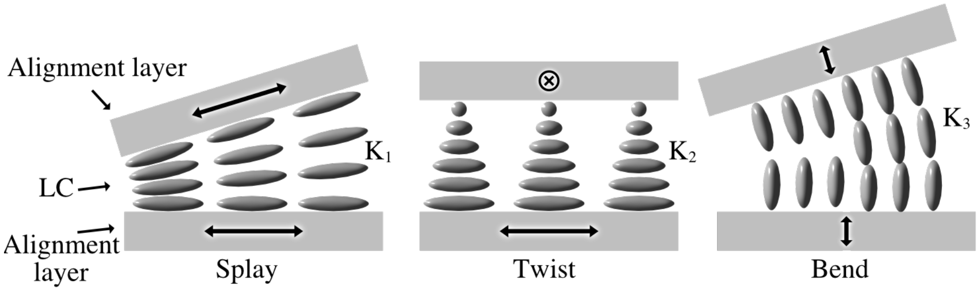

Figure 2.4: Three types of nematic LC distortion and their notations of the Frank elastic constants, K_1, K_2, and K_3.

to zero when all the LC molecules align vertically on the substrate. Furthermore, the phase retardation $\Delta\phi$ presents on the relative transmittance T and the light intensity I which can be written as

$$T = \frac{I}{I_0} = \mathrm{T}_0 \sin^2(\frac{\Delta\phi}{2}) \tag{2.3}$$

Here, I_0 is the maximum of the light intensity.

The external electric field can control the LC director distribution and then, as shown in Fig. 2.3a, influences the phase retardation and the transmission. According to the above LC electric and optical properties, an LCD can be achieved by switching the bright ($T = 1$) and dark ($T = 0$) states in each pixel by tuning the strength of the driving voltage.

2.2.3 Distortion free energy

Previous sections showed that the LC orientation can be controlled by the balance between the surface alignment and the external electric field. However, the LC director distribution is still unquantified. In 1958, Frank reported a general theory of curvature-elasticity in a nematic LC which can be used to express the LC director distribution under an external field [13]. Here the Frank elastic constants are classified into three types: splay K_1, twist K_2, and bend K_3 (see Fig. 2.4) [14]. The distortion free energy density can be expressed as

$$F_d = \frac{1}{2}\mathrm{K}_1 \left(\nabla \cdot \mathbf{n}\right)^2 + \frac{1}{2}\mathrm{K}_2 \left(\mathbf{n} \cdot \nabla \times \mathbf{n}\right)^2 + \frac{1}{2}\mathrm{K}_3 \left(\mathbf{n} \times \nabla \times \mathbf{n}\right)^2 \tag{2.4}$$

where $\mathbf{n}$ is the LC director. Then we add the electric field free energy F_{E}.

$$F_E = -\frac{1}{2}\epsilon_\perp \mathbf{E}^2 - \frac{1}{2}\Delta\epsilon \left(\mathbf{n} \cdot \mathbf{E}\right)^2 \tag{2.5}$$

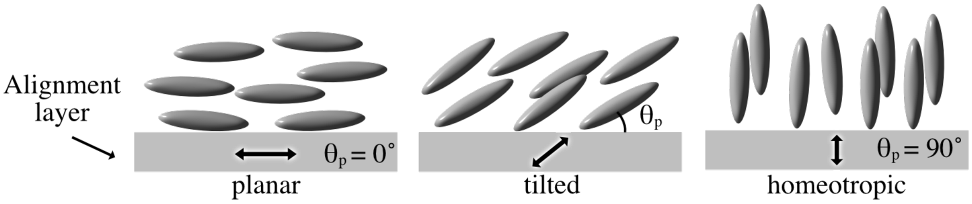

Figure 2.5: Three surface alignment types of nematic LC between substrates. The types are classified according to the pretilt angle θ_p. The pretilt angle is defined as the angle between the substrate and the LC long axis in the surface layer.

where $\Delta\epsilon = \epsilon_{\|} - \epsilon_{\perp}$ is the anisotropic electrical permittivity and $\mathbf{E}$ is the externally applied electric field. By solving the minimum of the total free energy $F = F_d + F_E$, the LC director $\theta(z)$ distribution can be obtained from both calculations and simulations following the time-dependent Ericksen-Leslie's equation, where back-flow and inertial effects are neglected for the cell structure used in this thesis (see Fig. 2.3a) [15, 16]:

$$\left(K_1 \sin^2\theta + K_3 \cos^2\theta\right)\frac{\partial^2\theta}{\partial z^2} + (K_3 - K_1)\sin\theta\cos\theta\left(\frac{\partial\theta}{\partial z}\right)^2 + \epsilon_0\Delta\epsilon \mathrm{E}^2 \sin\theta\cos\theta = \gamma\frac{\partial\theta}{\partial t} \tag{2.6}$$

Here K_1 and K_3 are the splay and bend distortion constants, respectively, and E is the strength of the external applied electric field. The LC director $\theta(z)$ is defined as the angle between the LC long axis at position z and the substrate plate. Based on this equation, the LC director can be numerically derived and the electro-optical properties of LCDs can be analyzed [17–19].

2.3 Liquid crystal display modes

Several specifications of LCDs are very important, including the screen size, resolution, contrast ratio, brightness, response time, energy consumption and viewing angle [20, 21]. To reach higher performances, LCDs are designed with different cell structures and alignment types. As shown in Fig. 2.5, the LC surface alignment types can be briefly classified as planar, tilted and homeotropic alignment, according to the pretilt angle θ_p [3]. The surface alignment technologies are further introduced in Sec. 2.4.

By designing various electrode patterns and alignment layers, several common LCD modes were developed to achieve higher LCD performance. However, as described in the introduction of Ch. 1, no single LCD mode is perfect for everything. Three main LCD modes and their performances are introduced in the following, including twisted nematic (TN), in-plane switching (IPS), and vertical alignment (VA) [3, 22]. In fact, each LCD mode can be further classified into several improved types by using different technologies for better performances [23–28]. In this thesis, the properties of LCD modes are discussed in a general way.

2.3.1 Twisted nematic mode

The twisted nematic mode, which was introduced in 1971 [29], occupies an important place in LCDs. Fig. 2.6 shows a schematic diagram of a normal-white TN-LCD in which the LC layer is sandwiched between a pair of crossed polarizers. Nematic liquid crystal molecules are twisted from the top to the bottom substrates over a 90° angle. In the OFF state, the polarization of the light adiabatically follows the molecular twist and is rotated over 90° while passing through the LC cell. It appears as a bright state because the polarized light can pass through the analyzer set at 90° to the polarizer. In the ON state, the positive dielectric anisotropy of the LC molecules makes them align vertically to the substrates along the externally applied electric field. The light is now blocked by the analyzer because the polarization of the light is not rotated while passing through the LC cell.

Under a pair of crossed polarizers, a TN LCD can be switched between the bright and dark states because the polarization of the light is rotated or not while passing the LC cell, respectively. The TN mode is operated in a low driving voltage (less than 5 V) [24] because the optical switching does not depend on the phase retardation as in the VA mode, but on the rotation of the polarization. Moreover, a TN cell can be designed with a narrower cell gap to achieve a faster response time because it does not need to keep a certain cell gap (~ 4 µm) as in the VA mode to achieve the phase retardation of π. According to the Maugain limit for maintaining a valid waveguiding behavior of a TN cell, the minimum of the cell gap is ~ 2 µm if we use 5CB LC molecules [30]. With a cell gap of 2 µm, the TN cell has a fast response time less than 5 ms [3]. The shortcoming of a TN LCD is the narrow viewing angle. Overall, a TN LCD is a good LCD mode for some personal devices which do not need a wide viewing angle, for instance a watch, a calculator and an ATM screen.

2.3.2 In-plane switching mode

In 1995, the in-plane switching (IPS) mode was developed by Hitachi in order to improve the contrast ratio and viewing angle [31, 32]. Fig. 2.7 shows a schematic diagram of an IPS-LCD. In the OFF state, the LC molecules are parallel to the polarization axis of the polarizer which appears as a dark state. In the IPS panel, the electrodes are designed on one substrate so most of the LC molecules are switched parallel to the substrate. In the ON state, the LC molecules are rotated to a 45° angle with respect to the polarizer and the analyzer by applying an external electric field. The transmission increases because of the generated phase retardation.

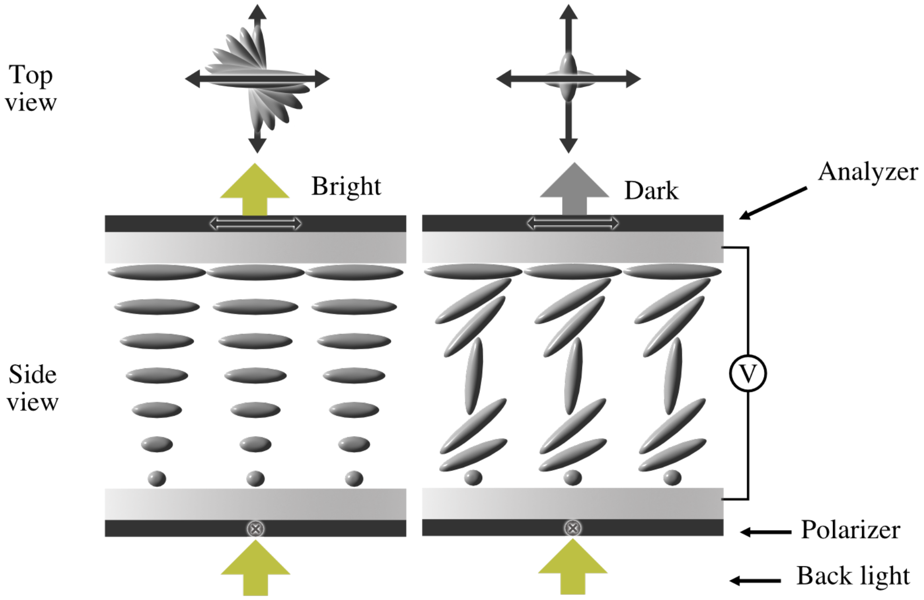

Figure 2.6: Schematic representations of bright and dark states for the TN mode.

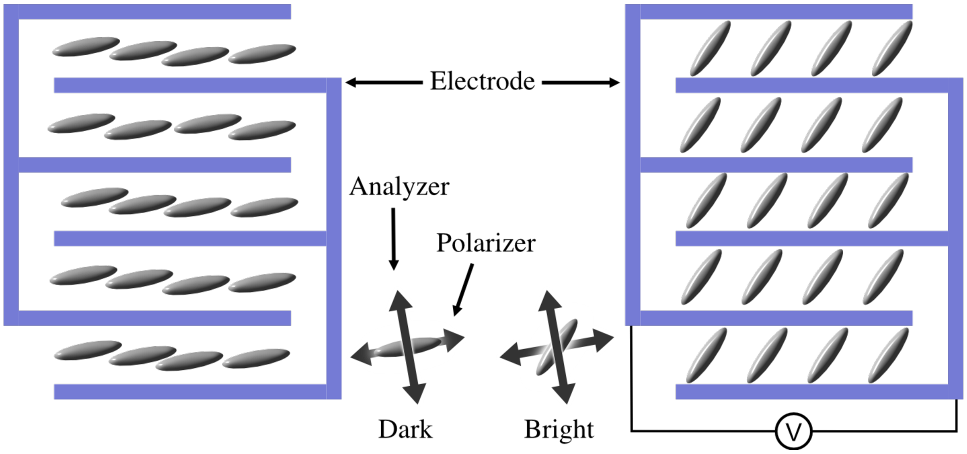

Figure 2.7: Schematic representations of dark and bright states for the IPS mode in top views.

The main advantage of an IPS LCD is that it provides a better color reproduction in a very wide viewing angle because the LC molecules rotate in-plane under the applied electric field. However, an IPS LCD has the disadvantage of a slow response speed. As a whole, an IPS LCD is suitable for the application of static image representations.

2.3.3 Vertical alignment mode

In 1971, M. F. Schiekel et al. reported a new LCD mode which is called the vertical alignment mode [33]. As the schematic diagram of the VA mode shown in Fig. 2.8, nematic LC molecules vertically align between two homeotropic alignment glass plates. In the OFF state, it is a dark state because the polarization of the light is not changed while passing through LC cell and the polarized light is blocked by the analyzer. In the ON state, a negative dielectric anisotropy of the LC molecules makes them rotate to planar or tilted forwards with respect to the substrates under the externally applied electric field. The LC molecules alter the polarization state of the light because of the phase retardation effect from the LC birefringence. The transmission depends on the amount of tilt generated by the electric field.

For a dark state of a VA LCD, all LC molecules align vertically which means that it is totally black because no any phase retardation was generated. Therefore a VA LCD has a very high contrast ratio. Comparing with a TN mode, a VA LCD has a wider viewing angle. Comparing with an IPS mode, a VA LCD presents a faster response speed, but its viewing angle is not as wide as an IPS mode. To obtain a wider viewing angle, a multi-domain mode was developed as the description in the following section.

2.3.4 Multi-domain vertical alignment mode

As shown in Fig. 2.9a, for the VA mode, no light passes through the analyzer while we observe the display from the normal direction. However, at a larger viewing angle, the light passes through the analyzer because of the generated phase retardation. For the VA mode, the transmission depends on the viewing angle.

For compensating the viewing angle dependency of the individual pixels, the multi-domain vertical alignment (MVA) mode has been developed [34]. As shown in Fig. 2.9b, the LC pretilt angles are controlled in each domain by adding protrusions on the alignment layers [26]. The viewing angle dependency is compensated by averaging the transmission in the multi-domain system. Furthermore, the MVA mode not only provides a wide viewing angle, but also a good color reproduction and fast response times which is suitable and commonly used in large size TVs.

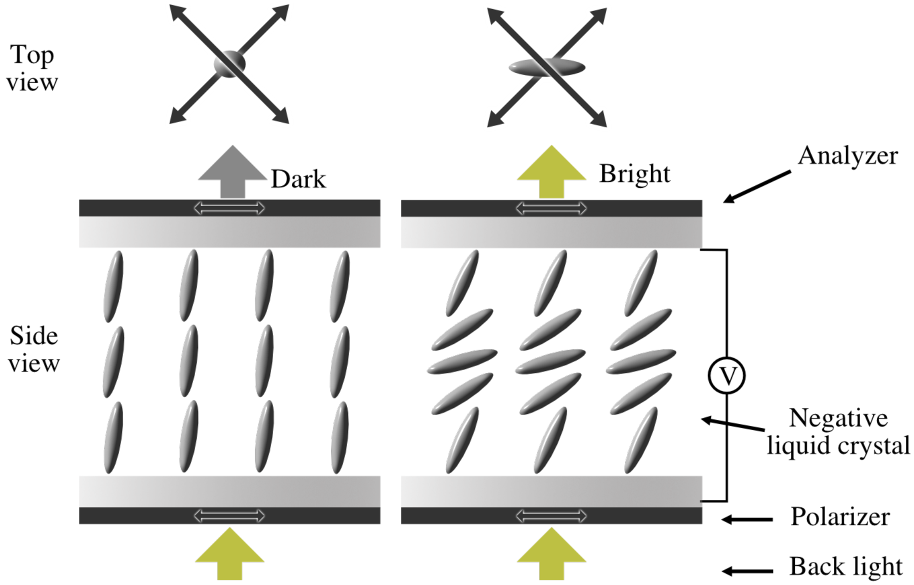

Figure 2.8: Schematic representations of dark and bright states for the VA mode.

2.4 Surface alignment technologies

The surface alignment layer plays an extremely important role in an LCD structure [3, 4]. The rubbed polyimide is a wide-used homogeneous alignment technology with a high transparency and chemical stability [30, 35]. However, these LC cells may have some defects which come from the dust and static electricity generated during the rubbing process. Moreover, the rubbing treatment can hardly be used for locally controlling the pretilt angle and complicated lithography processes have to be applied for a multi-domain system [36].

To avoid the defects generated by the rubbing process, several non-contact alignment technologies were developed: photo alignment [37–39], ion beam alignment [40, 41], and oblique evaporation [42–44]. A shadow mask lithography technology provides another solution for a multi-domain system [45]. As a stencil method, a material can be physically deposited by evaporation [42] or sputtering [40, 46] through a shadow mask onto a selective area of a substrate. By combining a deposited alignment film and the shadow mask technology, a small domain LC pretilt angle control can be achieved.

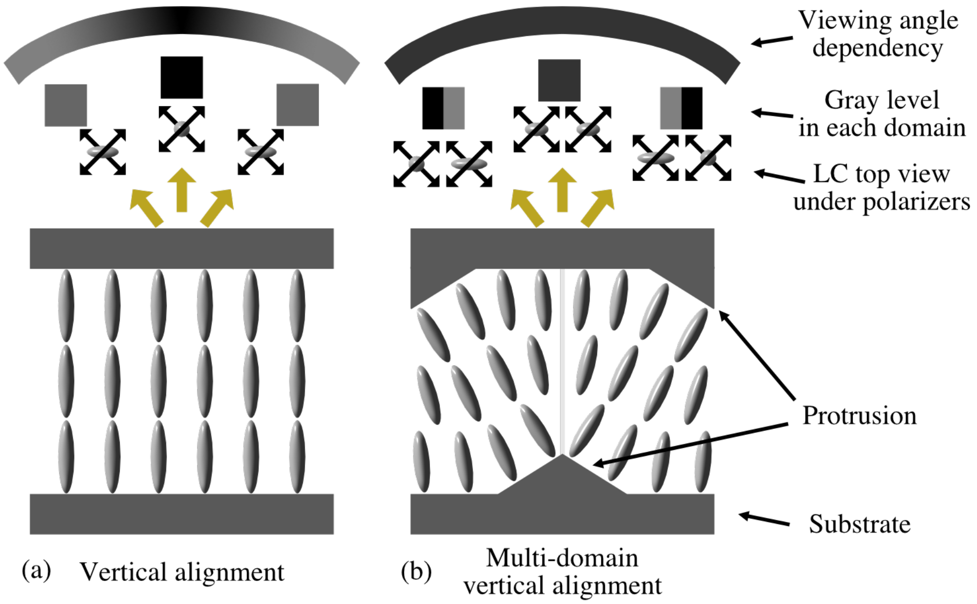

Figure 2.9: (a) The vertical alignment and (b) multi-domain vertical alignment.

2.5 Conclusion

Liquid crystal displays are widely used based on mature surface alignment and external field control technologies. The key technological challenge of a multi-domain mode is how to control the liquid crystal (LC) pretilt angle precisely in each individual domain. In Ch. 4, we present a new surface treatment method for the pretilt angle control. By combining this method with a shadow mask technique, a multi-domain pretilt angle control is achieved and demonstrated in Ch. 8. The elastic free energy theory provides a calculation method to predict the general behavior of LC media and the calculation results are discussed in Ch. 7.

References

[1] F. J. Kahn, Applied Physics Letters **20**, 199 (1972).

[2] I. Dierking, *Textures of Liquid Crystals* (John Wiley & Sons, 2006).

[3] K. Takatoh, M. Hasegawa, M. Koden, N. Itoh, R. Hasegawa, and M. Sakamoto, *Alignment Technology and Applications of Liquid Crystal Devices* (CRC Press, 2005).

[4] T. Rasing and I. Musevic, *Surfaces and Interfaces of Liquid Crystals* (Springer Science & Business Media, 2013).

[5] P. G. de Gennes and J. Prost, *The Physics of Liquid Crystals* (Oxford University Press, 1993).

[6] H. Kitzerow and C. Bahr, *Chirality in Liquid Crystals* (Springer Science & Business Media, 2006).

[7] F. Reinitzer, Monatshefte für Chemie und verwandte Teile anderer Wissenschaften **9**, 421 (1888).

[8] M. G. Friedel, Annales de Physique **18**, 273 (1922).

[9] P. J. Collings and M. Hird, *Introduction to Liquid Crystals*, Chemistry and Physics (CRC Press, 1997).

[10] B. R. Ratna and R. Shashidhar, Pramana **6**, 278 (1976).

[11] V. Belyaev, A. Solomatin, and D. Chausov, Optics express **21**, 4244 (2013).

[12] T. Scharf, *Polarized Light in Liquid Crystals and Polymers* (John Wiley & Sons, 2007).

[13] F. C. Frank, Discussions of the Faraday Society **25**, 19 (1958).

[14] J. D. Bunning, T. E. Faber, and P. L. Sherrell, Journal de Physique **42**, 1175 (1981).

[15] J. L. Ericksen, Transactions of The Society of Rheology **5**, 23 (1961).

[16] F. M. Leslie, Archive for Rational Mechanics and Analysis **28**, 265 (1968).

[17] L. Weng, P.-C. Liao, C.-C. Lin, T.-L. Ting, W.-H. Hsu, J.-J. Su, and L.-C. Chien, AIP Advances **5**, 097218 (2015).

[18] X. Nie, H. Xianyu, R. Lu, T. X. Wu, and S.-T. Wu, Journal of Display Technology **3**, 280 (2007).

[19] D.-K. Yang and S.-T. Wu, *Fundamentals of Liquid Crystal Devices* (John Wiley & Sons, 2014).

[20] H.-S. Kwok, S. Naemura, and H. L. Ong, *Progress in Liquid Crystal Science and Technology*, In Honor of Shunsuke Kobayashi's 80th Birthday (World Scientific, 2013).

[21] G. Meier, E. Sackmann, and J. G. Grabmaier, *Applications of Liquid Crystals* (Springer Science & Business Media, 2012).

[22] S. J. Elston and J. R. Sambles, *The Optics of Thermotropic Liquid Crystals* (CRC Press, 1998).

[23] T.-L. Ting, C.-Y. Chen, S.-W. Tsao, M.-J. Lu, Y.-Y. Kung, W.-H. Hsu, and J.-J. Su, Journal of Display Technology **9**, 832 (2013).

[24] D. H. Kim, Y. J. Lim, D. E. Kim, H. Ren, S. H. Ahn, and S. H. Lee, Journal of Information Display **15**, 99 (2014).

[25] S.-W. Kang, Y. E. Choi, B. H. Lee, J. H. Lee, S. Kundu, H.-S. Jin, Y. K. Yun, S. H. Lee, and L. Komitov, Liquid Crystals **41**, 552 (2013).

[26] K.-H. Kim, E.-Y. Jeon, B. W. Park, S.-W. Choi, D. H. Song, H. Kim, K.-C. Shin, H. S. Kim, and T.-H. Yoon, Journal of the Optical Society of Korea **16**, 166 (2012).

[27] G. Yang and Y. Sun, Liquid Crystals **38**, 507 (2011).

[28] S. H. Lee, S. S. Bhattacharyya, H.-S. Jin, and K.-U. Jeong, Journal of Materials Chemistry **22**, 11893 (2012).

[29] M. Schadt and W. Helfrich, Applied Physics Letters **18**, 127 (1971).

[30] C. Mauguin, Bulletin de la Société Française de Minéralogie et de Crystallographie **34**, 71 (1911).

[31] M. Oh-e and K. Kondo, Applied Physics Letters **67**, 3895 (1995).

[32] M. Oh-e and K. Kondo, Applied Physics Letters **69**, 623 (1996).

[33] M. F. Schiekel and K. Fahrenschon, Applied Physics Letters **19**, 391 (1971).

[34] Y. Koike and K. Okamoto, Fujitsu Science Technical Journal **35**, 221 (1999).

[35] M. K. Ghosh and K. L. Mittal, *Polyimides: fundamentals and applications* (CRC Press, 1996).

[36] Y. Koike, T. Kamada, K. Okamoto, M. Ohashi, I. Tomita, and M. Okabe, SID92 DIGEST **23**, 798 (1992).

[37] W. M. Gibbons, P. J. Shannon, S. T. Sun, and B. J. Swetlin, Journal de Physique **42**, 1175 (1991).

[38] M. Schadt, H. Seiberle, and A. Schuster, Nature **381**, 212 (1996).

[39] J. Lu, S. V. Deshpande, E. Gulari, J. Kanicki, and W. L. Warren, Journal of Applied Physics **80**, 5028 (1996).

[40] P. Chaudhari, J. Lacey, J. Doyle, E. Galligan, S. Lien, J. Lacey, J. Doyle, E. Galligan, S.-C. A. Lien, A. Callegari, G. Hougham, N. D. Lang, P. S. Andry, R. John, K.-H. Yang, M. Lu, C. Cai, J. Speidell, S. Purushothaman, J. Ritsko, M. Samant, J. S. hr, Y. Nakagawa, Y. Katoh, Y. Saitoh, K. Sakai, H. Satoh, S. Odahara, H. Nakano, J. Nakagaki, and Y. Shiota, Nature **411**, 56 (2001).

[41] J. Stöhr, M. G. Samant, J. Lüning, A. C. Callegari, P. Chaudhari, J. P. Doyle, J. A. Lacey, S. A. Lien, S. Purushothaman, and J. L. Speidell, Science **292**, 2299 (2001).

[42] J. L. Janning, Applied Physics Letters **21**, 173 (1972).

[43] T. Uchida, M. Ohgawara, and M. Wada, Japanese Journal of Applied Physics **19**, 2127 (1980).

[44] L. A. Goodman, J. T. McGinn, C. H. Anderson, and F. DiGeronimo, Electron Devices, IEEE Transactions on **24**, 795 (1977).

[45] A. Tixier, Y. Mita, J. P. Gouy, and H. Fujita, Journal of Micromechanics and Microengineering **10**, 157 (2000).

[46] H.-Y. Wu and R.-P. Pan, Applied Physics Letters **91**, 074102 (2007).

CHAPTER 3

Experimental Methods

3.1 Introduction

For achieving higher liquid crystal display (LCD) performances, a variety of LC cell modes had been developed which are detailedly described in Sec. 2.3 [1]. During the same time period, many techniques have been developed for investigating liquid crystal (LC) molecules and LCD properties. Some well-known methods to observe the LC behaviors in a cell are LC texture characterization [2, 3], pretilt angle measurement [4], and electric-optical effect [1]. The texture characterization and pretilt angle measurement are used to observe the LC surface alignment condition. The study of the electric-optical effect allows us to examine the LCD performance, such as contrast ratio and optical response speed.

The different LCD modes are designed by using different LC surface alignment types and electrode patterns (see Sec. 2.3). Therefore, many LC surface alignment technologies had been developed, such as photo alignment [5–7], ion beam alignment [8, 9], and oblique evaporation [10–12]. In this thesis, we found that by combining a deposited LC alignment film and the shadow mask technology, the LC pretilt angle can be controlled in a small selected domain. To investigate the LC alignment mechanism, the surface can be examined physically and chemically by two surface analyzing methods as follows [13]. Nanometer scale particle sizes and surface roughness can be observed by using atomic force microscopy (AFM). X-ray photoelectron spectroscopy (XPS) is a surface quantitative investigation technique which can give surface information, including elemental compositions and the chemical state of the elements.

This chapter presents all the relevant experimental setups and analytical methods. First, it starts with detailedly describing our sample preparation setup and process. Then, the observation methods of LC static and dynamic properties are introduced, including the LC texture, the pretilt angle and electric-optical effect measurements. In the last section, we describe two surface investigation techniques, AFM and XPS. According to our sample preparation method, we can control the LC pretilt angle by choosing different LC alignment thin film deposition conditions. Then, for investigating the dependence of the LCD properties on the pretilt angle, samples were studied by using the above-mentioned experimental and analytical methods.

3.2 Cell preparation

The preparation of a pretilt angle controlling parallel alignment (PA) cell contains several steps: ITO-glass cleaning, polyimide coating, sputtering thin film deposition, and cell confinement. Here, we start with the introduction of the sputtering machine.

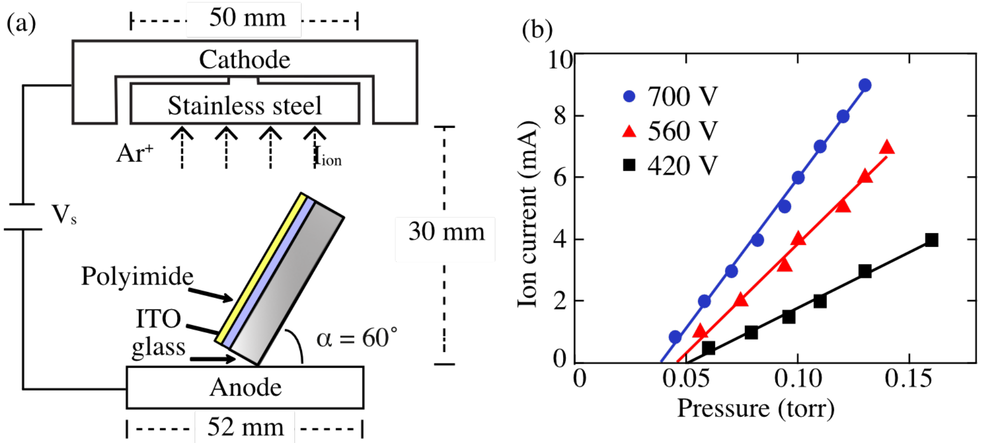

Figure 3.1: (a) Schematic setup with its dimensions and (b) Chamber pressures for corresponding ion beam currents.

3.2.1 Ion beam sputter machine

A direct-current ion-coater (model IB-3, EIKO Engineering Co., Ltd.) was used to deposit a thin film on the substrate as an LC alignment layer (see Fig. 3.1a). The diameters of the top and bottom electrodes are 50 mm and 52 mm, respectively, and they were 30 mm spaced apart. They were placed in a glass chamber with two tubes: one was connected to an air pump, while the other was linked to an argon gas source via a flow valve for chamber-pressure control. After the chamber pressure was pumped down till 30 mTorr, the sputtering voltage control was switched and fixed at V_s. Then, the argon valve was opened and kept at a specific pressure P for a corresponding ion beam current I_{ion} (see Fig. 3.1b). The argon ion beam machine IB-3 could be set in the etching mode or coating mode by switching the voltage polarity. In the etching mode, the substrates were placed on the bottom electrode (cathode). In the coating mode, the top electrode was chosen as the cathode so that the target pad mounted on top would be bombarded by argon ions produced from the collision of electrons with argon atoms. As shown in Fig. 3.1a, the substrates set on the bottom were coated with a thin film. The material of the deposited thin film is sputtered from the target due to the bombardment with argon ions which are accelerated by the external electric field. The thickness th strongly correlated with the ion beam current I_{ion} and coating time t_c [14]:

$$th = \mathrm{C}\, I_{ion}\, t_c \tag{3.1}$$

where C is a coefficient corresponding to the target material and the sputtering energy which is varied by the sputtering voltage V_s.

3.2.2 Substrate preparation and cell confinement

The substrates were prepared in three steps, (1) ITO-glass cleaning, (2) polyimide coating and (3) Fe_2O_3/Cr_2O_3 deposition by sputtering the stainless steel target. The first step is the substrate cleaning. The 1×2 cm^2 ITO-glasses were put into ultrasonic baths for four different solvents in the following order, clean water with neutral liquid detergent, acetone, methanol, and deionized water. The bath time is 5 minutes for each solvent. Between the process of the solvent change, the substrates were dried by blowing nitrogen gas. After an hour baking in a 100°C oven, the substrates were ready for the next step, polyimide coating.[1]

We spin-coated polyimide SE-130B (PI, Nissan Chemical Industries, Ltd.) on a cleaned substrate. The spin speed is controlled at 2000 rpm for the first 15 seconds and then increased up to 4000 rpm for another 25 seconds. The substrates were prebaked at 80°C for 5 minutes and then cured at 170°C for an hour. Note that we have no velvet rubbing process in our cell preparation. The spin coating is a reliable PI coating technology.

As shown in Fig. 3.1a, the PI-coated substrate was placed on the bottom (anode) with a glass stand for keeping the sample at $\alpha = 60°$ with respect to the horizontal. A stainless steel pad was mounted on the top electrode (cathode) as the sputtering target. After pumping down the chamber pressure till 30 mTorr, the argon gas was entered and kept at a specific pressure to keep the sputtering voltage V_s and ion beam current I_{ion} constant. Several pairs of substrates were prepared under various conditions, including coating time $t_c = 0 \sim 120$ min, ion beam current $I_{ion} = 3$ and 5 mA, and sputtering voltage $V_s = 420$, 560, and 700 V. The composition of the deposited thin film from the sputtered stainless steel target was identified as Fe_2O_3/Cr_2O_3 by XPS (The details are presented in Sec. 5.3.1).

For each sputtering condition, we prepared three samples. As shown in Fig. 3.2a, based on the size of the bottom electrode, only two substrates can be coated at once and the substrates were marked as “R” (right) and “L” (left), respectively. For one sample, we coated two pairs of substrates and marked them as 1R, 1L, 2R, and 2L. As shown in Fig. 3.2b, substrates 1R and 2L were combined as an anti-parallel (AP) alignment cell and sandwiched with mylar films or µm size glass balls as spacers.[2] The empty cells were filled with 4’-n-pentyl-4-cyanobiphenyl (5CB, Merck) at 60°C

---

[1] In addition, the room humidity has to be controlled below 40%. Otherwise, the polyimide cannot be coated uniformly on the ITO glass.

[2] In Ch. 4, we used 23 µm mylar as a spacer for the high accurate pretilt angle measurement. In Ch. 6, different thickness of the glass ball were chosen for the electric-optical effect investigation of PA cells with different pretilt angle.

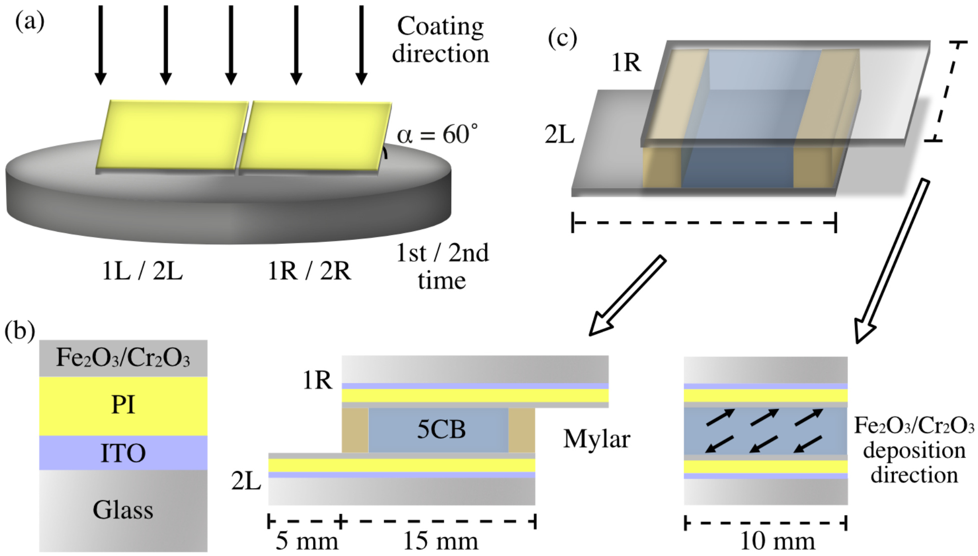

Figure 3.2: (a) Substrates identification in sputtering deposition. The coating direction is defined as perpendicular to the electrode plates. Two substrates were coated at once and marked as "R" (right) and "L" (left), respectively. For each sample, we coated two pairs of substrates, 1R, 1L, 2R, and 2L. (b) The layer structure after coating process. Here, the schematic figure of the layer structure presents the coating order without the interaction between layers. (b) Cell confinement with mylar thin films as spacers.

and annealed to room temperature. The other two substrates, 1L and 2R, were used for the surface investigations in Ch. 5.

3.3 Measurement of LC alignment and dynamic properties

LCs can be applied for displays because LCs can be easily aligned by the balance between the alignment surface and the external field. The bright and dark states can be achieved because the polarization can be changed while the light passes through the LC cell. Several optical observation technologies were developed [1]. Three technologies are introduced in the following sections.

3.3.1 Polarizing optical microscope

A polarizing optical microscope (POM) is widely used for the LC alignment investigation. By observing the texture of the LC cell between a pair of crossed polarizers (see

Fig. 3.3a), the LC surface alignment types can be identified [3, 15]. In our study, 5CB behaves as a nematic liquid crystal (NLC) phase at room temperature. The textures of three well-known NLC alignment types are introduced, including (1) vertical, (2) planar or tilted, and (3) random planar.

In a vertical NLC alignment cell, LC molecules are vertically aligned. As shown in Fig. 3.3b, the projection of the rod-like NLC onto the substrate plane is a circle. No matter the orientation of the cell at 0° or 45° relative to the crossed polarizers, the cell only exhibits the dark state (see Fig. 3.3b) because the cell cannot induce any phase retardation. This texture can be found in a vertical LC cell which is prepared with the substrate coated with a homeotropic layer, for instance, DMOAP [16].

In a planar NLC alignment cell, the LC molecules align uniformly parallel the substrate. In a tilted NLC alignment cell, the LC molecules are parallel to each other and have a tilt angle with respect to the substrate. In the above two NLC alignment types, dark and bright states correspond to the relative LC orientation at 0° and 45° with respect to the crossed polarizers (see Fig. 3.3c) because of the phase retardation acquired by the linearly polarized light rotation after passing through the sample. Actually, a planar cell can be regarded as a special case of a tilted cell with a zero tilt angle. This texture can be found in LC cells which are shown in the following chapters.

One of the other well-known textures of nematic LC is random planar (see Fig. 3.3d). In this alignment, the LC molecules lie down on the substrate. In the short-order range, LC molecules align parallel with their neighbors. In the long-order range, LC directors are parallel to the substrate but in random directions. This texture can be found in a cell with a non-rubbed polyimide substrate.

In Ch. 4, POM is used to characterize the LC surface alignment types of cells which are prepared with different alignment layer structure. Moreover, in Ch. 8, POM images provide good evidence of our multi-domain cell and show the high uniformity in each domain.

So far, POM is a simple method to characterize the alignment types and uniformity of the LC cells. However, the long and short axes cannot be distinguished and the LC director cannot be determined in a planar or tilted texture.

3.3.2 Pretilt angle measurement

In the tilt alignment cell, we want to investigate the angle between the surface LC long axis and the substrate which is called pretilt angle θ_p. There are several well-known pretilt angle measurement techniques, for instance, the crystal rotation method, the capacitive method , and the magnetic null method [4]. We choose the crystal rotation method which does not need an external field during the pretilt angle measurement.

As shown in Fig. 3.4a, due to the LC birefringence property, an incident ray with the incident angle ψ is separated into two rays, the ordinary ray (o-ray) and the

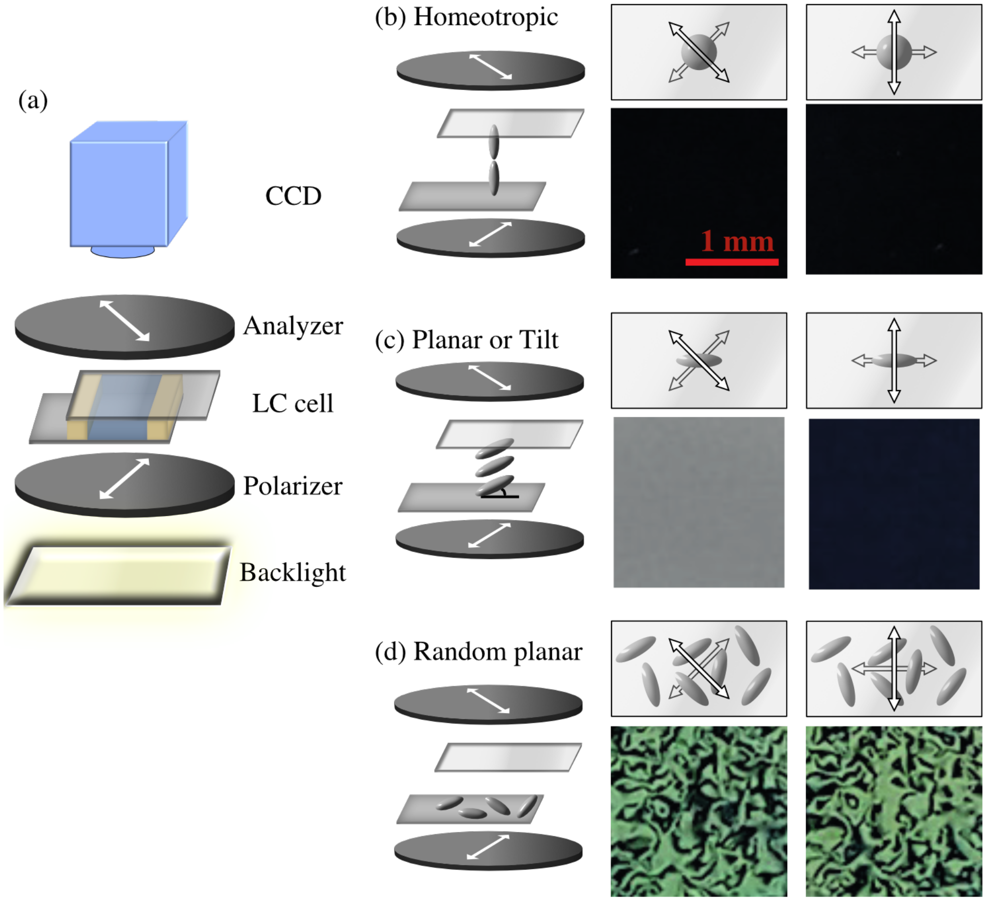

Figure 3.3: (a) Schematic setup of the polarising optical microscope (POM). The white arrows are the polarization directions of polarizer and analyzer. 3D and top view of the schematic setup with the LC alignment direction and the textures of (b) vertical, (c) planar/tilted, and (d) random planar alignments.

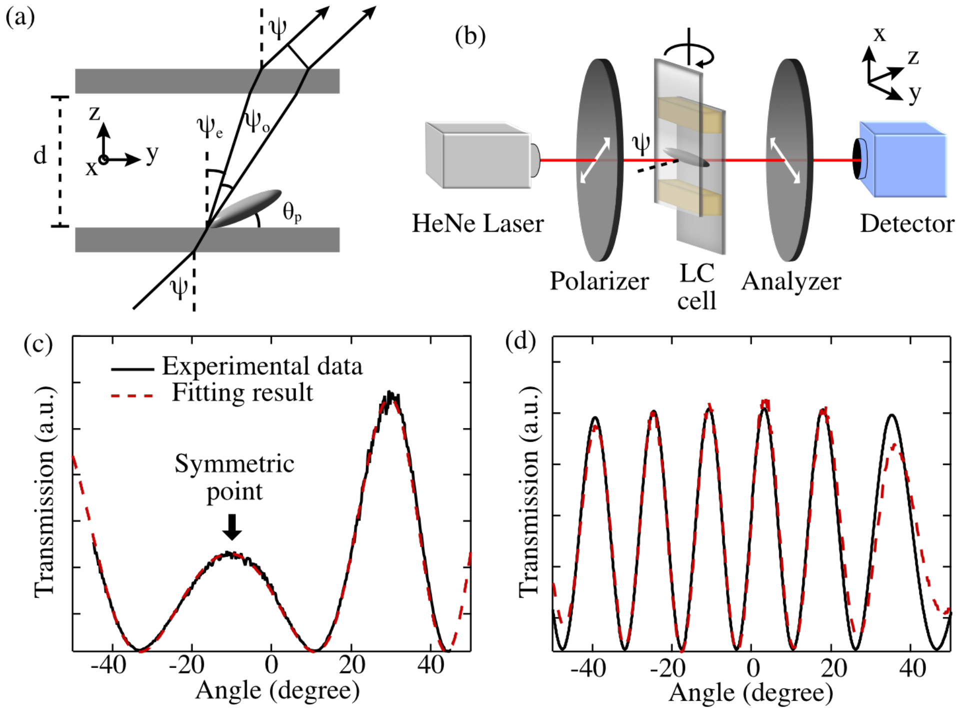

Figure 3.4: (a) The birefringence effect in a cell. (b) Schematic setup of the pretilt angle measurement. The experimental (red line) and fitting results (black line) of (c) the low pretilt angle cell and (d) the high pretilt angle cell.

extraordinary ray (e-ray) with the angles ψ_o and ψ_e, respectively. The optical path difference (OPD) can be written as

$$OPD = [n_{eff}(\frac{d}{\cos\psi_e}) + (\tan\psi_o - \tan\psi_e)d\sin\psi] - n_o(\frac{d}{\cos\psi_o}) \tag{3.2}$$

According to Snell's law, $\sin\psi = n_o\sin\psi_o = n_e\sin\psi_e$, the OPD can be simplified as [17]

$$OPD = d[\frac{1}{c^2}(a^2-b^2)\sin\theta_p\cos\theta_p\sin\psi+\frac{1}{c}(1-\frac{a^2b^2}{c^2}\sin^2\psi)^{\frac{1}{2}}-\frac{1}{b}(1-b^2\sin^2\psi)^{\frac{1}{2}}] \tag{3.3}$$

where $a = \frac{1}{n_e}$, $b = \frac{1}{n_o}$, and $c = (a^2\cos^2\theta_p + b^2\sin^2\theta_p)$.

By using the setup as shown in Fig. 3.4b, the transmission as a function of angle can be measured. The angle ψ dependence of the transmission T can be derived from the phase retardation $\Delta\phi$ (see Sec. 2.2.2).

$$T = T_0 \sin^2(\frac{\Delta\phi}{2}) = T_0 \sin^2(\frac{2\pi}{\lambda} OPD) \tag{3.4}$$

In general, as shown in Fig. 3.4c, the pretilt angle can be derived from the angle of the symmetry point of the angular dependence of the transmittance and the cell thickness d. However, as shown for the example of a large pretilt angle cell in Fig. 3.4b, the symmetry point can be out of the measured range, -55° to 55°. As shown in Fig. 3.4c and d, the pretilt angle can be obtained by finding the best agreement of the angle dependent transmissions between the calculation (black solid line) and the experiment result (red dashed line).

3.3.3 Electro-optical effect

LCDs operate by switching between bright and dark states in each pixel by the particular LC electric-optical effect. By applying the driving voltage, the brightness can be controlled because of the change of the LC orientation distribution (see Sec. 2.2). The LC orientation distribution can not be directly measured in an experiment, only its effects on the light which present itself as a phase retardation in the transmission. Therefore, the transmittance and the phase retardation of the external electric field dependence needs a further investigation.

With the setup shown in Fig. 3.5a, we apply a 1 kHz square-wave driving voltage and then record the transmission as a function of the driving voltage (see Fig. 3.5b). The optical time response can also be acquired by connecting the detector and the voltage switching signals to an oscilloscope. This can help us for the further studies of LCD performances, such as contrast ratio and response time, in Ch. 6. Moreover, by rotating the LC cell with a rotating stage, the effect of the viewing angle dependence for a multi-domain LC cell can be examined in Ch. 8.

3.4 Surface studies

To investigated the LC alignment mechanism, we introduce two surface investigation techniques as follows.

3.4.1 Topography - AFM

Atomic force microscopy (AFM) is a nanometer scale surface topography scan technology. The AFM (Dimension 3100 AFM, VEECO) we used can be operated under two modes depending on different tip motion types, contact and tapping modes. In this thesis, all the AFM images and data are acquired under the tapping mode. In the tapping mode, the cantilever with a tip is driven over the surface and the oscillator

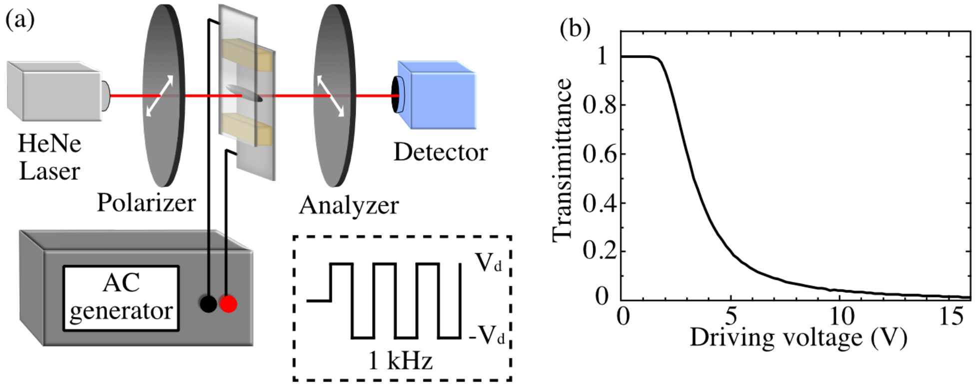

Figure 3.5: (a) Schematic setup and (b) Experimental result of an electric-optical effect experiment. The LC cell is driven by an 1 kHz square wave with voltage amplitude V_d.

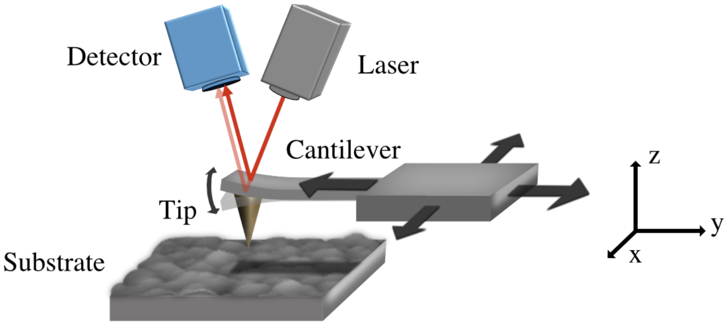

Figure 3.6: Schematic of AFM tapping mode. The amplitude change of this oscillation of the cantilever is measured by detecting a laser reflection from the top surface of the cantilever.

is set near its resonance frequency (see Fig. 3.6). While the tip comes closer to the surface, the amplitude of this oscillation of the cantilever decreases because of the forces between the tip and the surface. The interaction forces include Van der Waals forces, dipole-dipole interactions, electrostatic forces, etc. The amplitude change of the oscillation of the cantilever is measured by detecting a laser reflection from the top surface of the cantilever.

As shown in Fig. 3.7a, after a 2D scan of the substrate surface by moving the tip, the topography can be reproduced as a height image with 1×1 nm^2 scan resolution. A 2D height image allows us to investigate the surface morphology and the structure dimensions. The height image can also be presented as a 3D surface profile (see Fig.

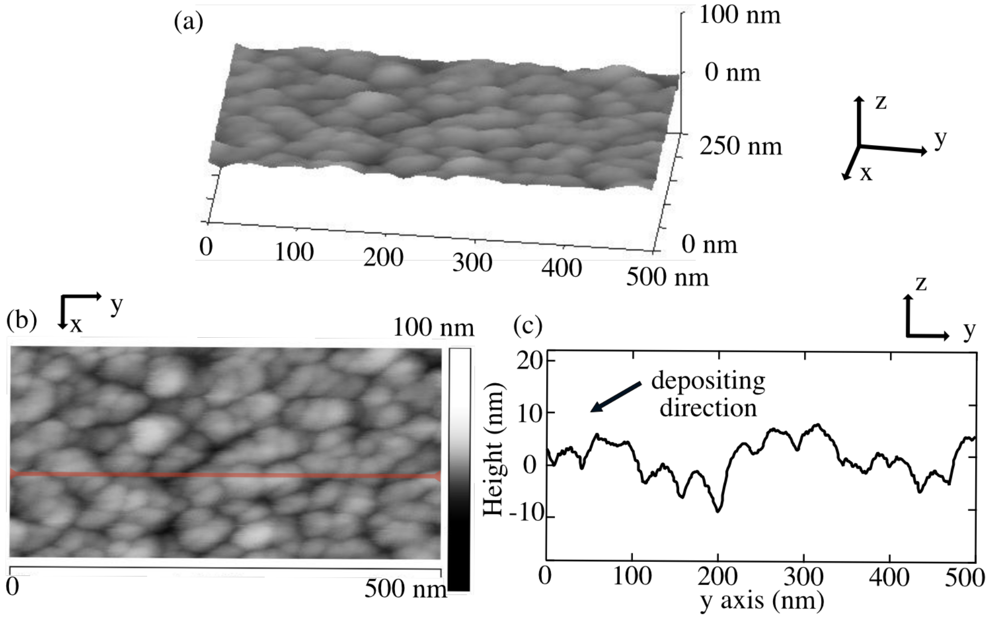

Figure 3.7: (b) A 3D image, (c) height image and (d) cross section of the AFM scan. The image (c) is the cross section of the red line in (b). The 2D height image is obtained by scanning, with the tip moving in the **x** and **y** direction in Fig. 3.6.

3.7a) to observe the structure and the topography perceptively. Fig. 3.7c shows the cross section of the red line in Fig. 3.7b. We can observe that the topography has a structure or a pattern along the depositing direction. Furthermore, the roughness can be calculated as the arithmetic average of the absolute height of the AFM profile. The baseline is the average height (see the zero level in Fig. 3.7c). The experimental results of the AFM are presented in Sec. 5.3.

3.4.2 Surface element analysis - XPS

X-ray photoemission spectroscopy (XPS) is a quantitative surface chemical spectroscopic technique which can be used to investigate the chemical composition, the bond type, and the electron configuration of the top layer of a material.[3] As shown in Fig. 3.8, in a typical XPS experiment, X-rays irradiate the substrate surface and the photo-emitted electrons escaping from the top surface layer (1∼10 nm, few electron mean free paths) are detected. By counting the number of electrons and measuring

---

[3] XPS is also known as ESCA (Electron Spectroscopy for Chemical Analysis).

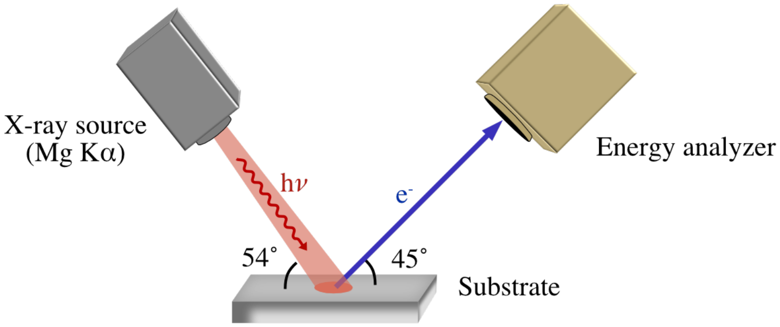

Figure 3.8: Schematic setup of XPS experiment.

their kinetic energies (see Fig. 3.9a and b), the chemical and electronic state can be characterized by the peak positions of the binding energy (BE) spectrum.

In this thesis, all spectra were obtained by using a PHI-1600 (Physical Electronics, Inc.) with a monochromatic source for X-ray irradiation of MgKα (1253.60 eV) and a precision energy analyzer (PHI 10-360). The X-ray incident angle and photoelectrons detection angle are 54° and 45°, respectively, from the substrate. The wide-scan XPS spectrum was scanned as a function of the binding energy from 0 to 1100 eV in the survey mode with 1 eV step size (see Fig. 3.9a). To further investigate the main peaks, we rescanned the spectra of five main peak ranges with a 0.2 eV step size (see Fig. 3.10).

Binding energy calibration

Due to the surface charging effect, the measured binding energy will be shifted c.a. 5 eV. Before the analysis, the XPS spectrum has to be calibrated with respect to a specific BE reference. In this study, all of our measured BE spectra were shifted to set the C 1s peak at 284.8 eV.

We collected many XPS peak data for compound identification from literature (see Ch. 5). However, in the literature, different BE reference elements and peak positions were chosen.[4] So we have to reshift properly all the collected BE peak position data (see Table 5.3∼5.5) to match our BE reference (C 1s at 284.8 eV). For instance, Ektessabi et al. [18] calibrated their XPS spectrum by C 1s at 284.7 eV so the peak position data from this literature (see Table 5.5) would be shifted +0.1 eV to match our BE reference (C 1s at 284.8 eV).

Some of the reports in the literature chose the O 1s and N 1s as the BE references. Based on our spectrum, these data would be shifted to map O 1s at 530.3 eV (in

---

[4] In general, authors choose one of the elements (C, O, N, and Au) as the reference.

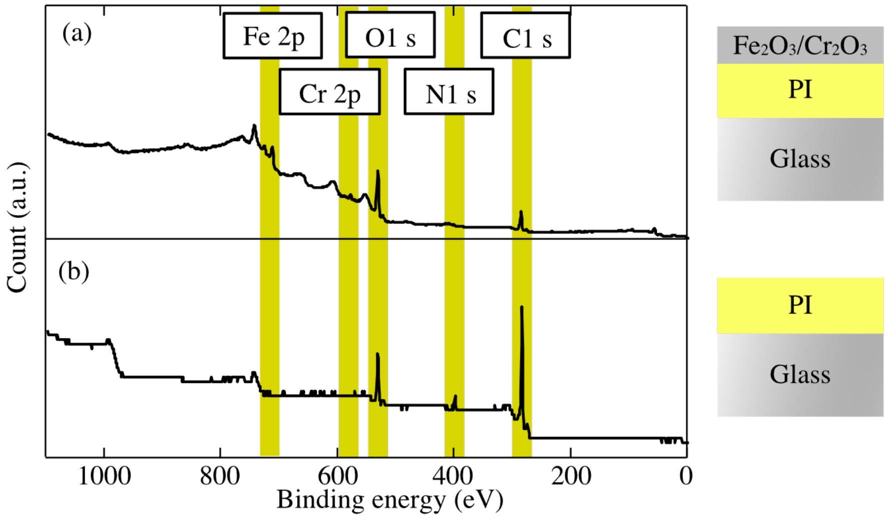

Figure 3.9: Experimental results of XPS experiment from (a) Fe_2O_3/Cr_2O_3 deposited and (b) PI coated substrate.

Cr_2O_3 [19]) and N 1s at 400.3 eV. A few literature studies chose Au $4f_{7/2}$ as the BE reference, but we had no gold signal in our substrate to calibrate these spectra. Harvey et al. [20] corrected the spectrum with Au $4f_{7/2} = 83.8$ eV and C 1s = 284.6 eV at the same time. Comparing to our reference C 1s at 284.8 eV, the BE reference from these literature studies can be set as Au $4f_{7/2} = 84.0$ eV.

Element characterization

After the BE calibration, the elements can be characterized roughly by identifying the peak positions of the binding energy spectrum. As the examples of Fig. 3.9b show, in the polyimide substrate, the peaks of C 1s, O 1s and N 1s signals were found at 284, 531 and 400 eV, respectively, which come from the polyimide layer. In the Fe_2O_3/Cr_2O_3 dposited substrate (see Fig. 3.9a), the C 1s and N 1s became relatively small and the signals of Fe 2p and Cr 2p appeared because the surface is covered with a thin Fe_2O_3/Cr_2O_3 film by sputtering the stainless steel target.

Detailed analysis methods

Furthermore, the XPS signal can be used to identified the chemical compounds and quantitatively analyze the compositions by the following steps: (1) background subtraction and (2) sub-peak fitting. To obtain a better analytical result, the spectra of

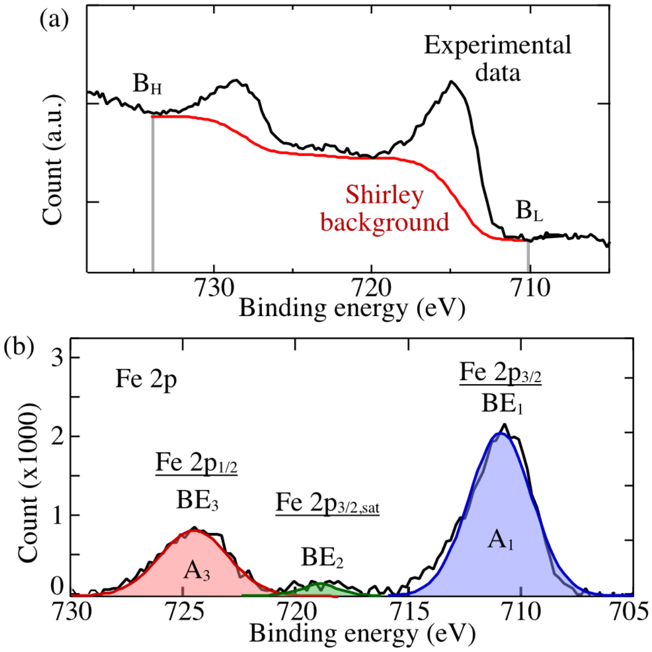

Figure 3.10: (a) A Shirley background (red line) with the given BE boundaries B_H and B_L. The black line is the raw Fe 2p data of the XPS measurement. (b) The experimental result and the fitting peaks of a Fe 2p spectrum. Fe 2p peaks were fitted separately by three sub-peaks which correspond to Fe $2p_{3/2}$ (blue), Fe $2_{p3/2,sat}$ (green), and Fe $2p_{1/2}$ (red). Not only the peak positions can be used to identify the compound type, but also the peak areas can also be used for a quantitative analysis which is presented in Ch. 5.

the main peak ranges were rescanned with a higher resolution (0.2 eV step size).

We chose the Fe 2p peak signal for chemical composition analysis and calculation. First, the background signal has to be subtracted. As shown in Fig. 3.10a, the Shirley background is computed with given BE boundaries (B_L and B_H) by using the package software MultiPak (ULVAC-PHI, Inc.) [21]. After the Shirley background subtraction, as shown in Fig. 3.10b, the precise peak positions (BE_1, BE_2 and BE_3) and the integrated areas (A_1, A_2 and A_3) are determined by using another software package (XPSPEAK 4.1).

In our substrate, there are several possible Fe chemical configurations, such as Fe (metal), FeO, Fe_2O_3, Fe_3O_4, $FeCO_3$ and FeOOH. The binding energy peak position is shifted (∼eV) depending on the different neighboring atoms. All the corresponding BE peak positions were collected from literature (see Table 5.3) and the compound can be identified by comparing the peak positions. In the experiment, Fe 2p peaks

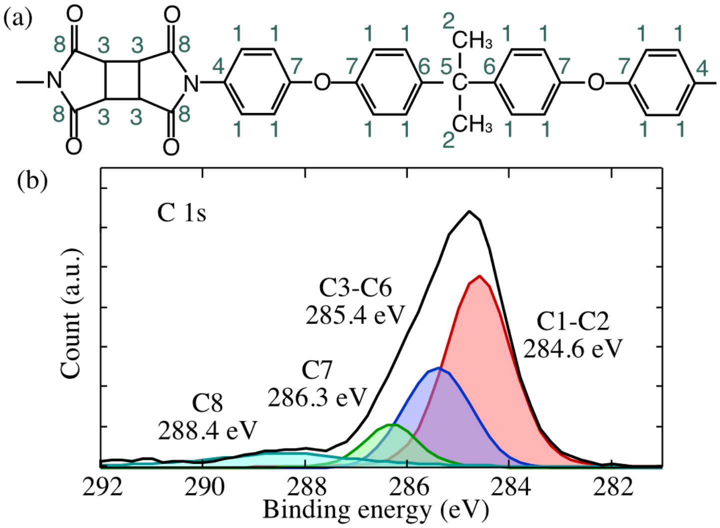

Figure 3.11: For a XPS case, the sub-peaks are too close to be separated by a peak fitting method [23] due to the full widths at half maximum of sub-peaks. (a) Polyimide repeated unit and the binding states of the carbon atoms (C1-C8). (b) XPS spectra of C 1s peak before and after Fe_2O_3/Cr_2O_3 coating process. Black line is the C 1s peaks which can be separated into four carbon groups. The coloured areas are the peaks of each carbon group (see Table 5.6).

(see Fig, 3.9b) were fitted separately by three sub-peaks which correspond to Fe $2p_{3/2}$ (BE_1 = 711.1 eV), Fe $2p_{3/2,sat}$ (BE_2 = 719.0 eV), and Fe $2p_{1/2}$ (BE_3 = 724.5 eV). By matching the sub-peak positions with the data from the literature, the Fe 2p peak signal can be identified as Fe_2O_3. The detailed discussions will be presented in Ch. 5.

The XPS can also be used for a quantitative analysis. For different elements, the quantitative composition n can be obtained by the following equation

$$n = \mathrm{c}A/S \tag{3.5}$$

Here, c is a constant, A is the integrated peak area in the XPS spectrum, and S is the relative sensitivity factor for each element [22]. In this thesis, the composition of Fe_2O_3 and Cr_2O_3 were quantified by this method. The XPS relative sensitivity factors were chosen as 2.0 (Fe $2p_{3/2}$) and 1.5 (Cr $2p_{3/2}$) in relation to F 1s = 1.00 [22]. According to the present measurements, the normalized compositions of the deposited thin film ($t_c = 10 \sim 120$ min) were $74.6 \pm 3.4\%$ Fe_2O_3 / $25.4 \pm 3.7\%$ Cr_2O_3.

In some cases, the sub-peaks are too close to be separated by peak fitting [23] due to the full widths at half maximum (FWHM) of the sub-peaks. In our experiment, the C 1s XPS spectrum contains eight types of carbon compounds (see Fig. 3.11a) which come from the polyimide. The detected C 1s line is the superposition of sub-peaks from various carbon compounds. Because several sub-peaks are closer than the FWHM of the C 1s peak of a specific compound (0.9 to 1.2 eV) [18], eight carbon compound types were classified into four groups, Carbon A to D (see Table 5.6) [23]. As shown in Fig. 3.11b, sub-peaks were convolutions of Gaussian and Lorentzian functions with the corresponding FWHM.[5] In Sec. 5.4, this analytical method will be used to study the surface chemical change during the thin film deposition process.

3.5 Conclusion

In the whole thesis, LC cells are prepared following the sample preparation method in Sec. 3.2. In Ch. 4, we investigate the relation between the pretilt angle and the sputtering conditions. The optical measurement methods introduced in Sec. 3.3 allow us to understand the LC static and dynamic behavior of the cell for different pretilt angles with an external electric field. These measurement methods are used in Ch. 4, 6 and 8. The surface investigation methods in Sec. 3.4 provide the possibilities for the investigations of a nanometer-scale topography and a quantitive surface composition analysis. These surface investigation techniques are used in Ch. 5.

---

[5] The FWHM of each group is given by the contained compound types. For instance, the Carbon B group gave a wide FWHM because the binding states (C3 to C6) have wider BEs (285.2 to 285.5 eV).

References

[1] K. Takatoh, M. Hasegawa, M. Koden, N. Itoh, R. Hasegawa, and M. Sakamoto, *Alignment Technology and Applications of Liquid Crystal Devices* (CRC Press, 2005).

[2] P. J. Collings and M. Hird, *Introduction to Liquid Crystals*, Chemistry and Physics (CRC Press, 1997).

[3] I. Dierking, *Textures of Liquid Crystals* (John Wiley & Sons, 2006).

[4] T. J. Scheffer and J. Nehring, Journal of Applied Physics **48**, 1783 (1977).

[5] W. M. Gibbons, P. J. Shannon, S. T. Sun, and B. J. Swetlin, Journal de Physique **42**, 1175 (1991).

[6] M. Schadt, H. Seiberle, and A. Schuster, Nature **381**, 212 (1996).

[7] J. Lu, S. V. Deshpande, E. Gulari, J. Kanicki, and W. L. Warren, Journal of Applied Physics **80**, 5028 (1996).

[8] P. Chaudhari, J. Lacey, J. Doyle, E. Galligan, S. Lien, J. Lacey, J. Doyle, E. Galligan, S.-C. A. Lien, A. Callegari, G. Hougham, N. D. Lang, P. S. Andry, R. John, K.-H. Yang, M. Lu, C. Cai, J. Speidell, S. Purushothaman, J. Ritsko, M. Samant, J. S. hr, Y. Nakagawa, Y. Katoh, Y. Saitoh, K. Sakai, H. Satoh, S. Odahara, H. Nakano, J. Nakagaki, and Y. Shiota, Nature **411**, 56 (2001).

[9] J. Stöhr, M. G. Samant, J. Lüning, A. C. Callegari, P. Chaudhari, J. P. Doyle, J. A. Lacey, S. A. Lien, S. Purushothaman, and J. L. Speidell, Science **292**, 2299 (2001).

[10] J. L. Janning, Applied Physics Letters **21**, 173 (1972).

[11] T. Uchida, M. Ohgawara, and M. Wada, Japanese Journal of Applied Physics **19**, 2127 (1980).

[12] L. A. Goodman, J. T. McGinn, C. H. Anderson, and F. DiGeronimo, Electron Devices, IEEE Transactions on **24**, 795 (1977).

[13] T. Rasing and I. Musevic, *Surfaces and Interfaces of Liquid Crystals* (Springer Science & Business Media, 2013).

[14] *Sputter Coating Technical Brief*, Quorum Technologies Ltd. (2002).

[15] T. Scharf, *Polarized Light in Liquid Crystals and Polymers* (John Wiley & Sons, 2007).

[16] F. J. Kahn, Applied Physics Letters **22**, 386 (1973).

[17] M. Françn, *Handbuch der Physik XXIV*, edited by S. Flügge, Grundlagen der Optik (Springer-Verlag, Berlin, 1956).

[18] A. M. Ektessabi and S. Hakamata, Thin Solid Films **377-378**, 621 (2000).

[19] M. Aronniemi, J. Sainio, and J. Lahtinen, Surface Science **578**, 108 (2005).

[20] D. T. Harvey and R. W. Linton, Analytical Chemistry (1981).

[21] D. A. Shirley, Physical Review B **5**, 4709 (1972).

[22] C. D. Wagner, L. E. Davis, M. V. Zeller, J. A. Taylor, R. H. Raymond, and L. H. Gale, Surface and Interface Analysis **3**, 211 (1981).

[23] D. Wolany, T. Fladung, L. Duda, J. W. Lee, T. Gantenfort, L. Wiedmann, and A. Benninghoven, Surface and Interface Analysis **27**, 609 (1999).

CHAPTER 4

LC Alignment by Obliquely Sputtered Fe_2O_3/Cr_2O_3 on Polyimide

4.1 Introduction

In liquid crystal displays (LCDs), several specifications are important, such as contrast ratio, and response time and viewing angle [1–3]. Response time is the time for an optical switching between the bright and the dark states. In general, the response time for going from the bright state to the dark state is more important than the response time for going from the dark state to the bright state. If it is not designed fast enough, after the screen refreshes, the screen still shows or mixes with the previous displayed image, which is called the ghost image effect [4]. In both in-plane switching (IPS) [5] and vertical alignment (VA) [6] modes, the response time for going from the bright state to the dark state depends on the time that is taken for the LC molecules to relax back to the initial state after switching off the driving voltage. This response speed is limited by the elastic relaxation of the LC molecules back to their initial state. In contrast to IPS and VA modes, in our parallel alignment (PA) cell (see Sec. 2.2.2), the response time to go from the bright state to the dark state can be faster by just giving a higher driving voltage. Moreover, F S Yeung et al. and X Nie et al. reported the dependence of the response time on the pretilt angle [7, 8]. Here the pretilt angle is the angle between the substrate and the LC long axis in the surface layer. Therefore, a faster response time can be achieved by designing a PA cell with a proper pretilt angle. This response time property is experimentally investigated and theoretically discussed in Ch. 6 and 7, respectively.

The viewing angle is one of the important properties, in particular for large screen applications. To reach the maximum angle at which a display can be observed with proper contrast ratio and gray scale, the viewing angle has to be designed as wide as possible [2]. For improving the viewing angle dependency of the individual pixels, multi-domain LC alignment technologies had been developed (see Sec. 2.3.4) [9–12]. In a multi-domain mode, the liquid crystal (LC) pretilt angles are controlled in a sub-pixel and the viewing angle dependency in each pixel is compensated by averaging the transmission of sub-pixels. The key technological challenge of this kind of multi-domain LCD mode is how to control the liquid crystal pretilt angle precisely in each sub-pixel.

The LC surface alignment layer which determines the LC pretilt angle is a crucial part of an LCD [13]. Nowadays, in single-domain LCDs manufacturing, the velvet rubbing treatment is the simplest and low-cost alignment technology with advantages of high transparency and chemical stability [14]. By rubbing the substrate which is spin coated with a polyimide (PI) thin film, a liquid crystal molecule can be oriented by this surface. The rubbed polyimide thin film presents a planar alignment in which the LC molecules are parallel to the substrate and along to the rubbing direction. However, the rubbing treatment cannot be applied to control the pretilt angle widely. Moreover, for a multi-domain system, complicated lithography processes have to be applied to control different LC alignment directions in sub-pixels [15].

Therefore, we aim to find an LC surface alignment method to be useful for a pretilt angle control multi-domain system. Oblique deposition of a thin film is a suitable LC alignment technology [16–18] which can also be applied to a multi-domain system by using a shadow mask lithography technology [19]. A LC alignment layer can be physically deposited by evaporation [16] or sputtering [20, 21] through the shadow mask onto a selective area of a substrate. The multi-domain preparation method is introduced in detail in Ch. 8. By combining deposition film and shadow mask lithography technologies, a selected local domain LC control can be achieved, resulting in a simpler fabrication comparing with a complex photolithographic process in a multi-domain PI mode system.

In earlier studies, a homeotropic alignment (see Sec. 2.3) was achieved by depositing a thin film by sputtering from a stainless steel target. However, it did not provide a wide pretilt angle control [21]. In this chapter, we demonstrate how to control the pretilt angle precisely with an obliquely deposited Fe_2O_3/Cr_2O_3 thin film on a polyimide-coated indium-tin-oxide (ITO) glass.[1] In Sec. 4.3.1, we found that the pretilt angle can be controlled continuously between 0° and 45° by varying the Fe_2O_3/Cr_2O_3 deposition times. In Sec. 4.3.2, to examine the essential of the roles of Fe_2O_3/Cr_2O_3 on polyimide and the oblique deposition, two cells were compared and their pretilt angle changes were observed. In Sec. 4.3.3, the relation between the pretilt angle and sputtering conditions was also studied and analyzed, based on the electric field distribution of the sputter system. According to the experimental results, to get a higher fabrication productivity, a shorter deposition time for a cell has the same pretilt angle by applying a higher sputtering voltage and a higher ion beam current.

4.2 Sample

Following the sample preparation steps in Sec. 3.2, we first spin-coated polyimide on a cleaned 1×2 cm^2 ITO-glass and the thickness of the PI layer measured by ellipsometer was c.a. 300 nm. Then we obliquely deposited a thin film on the PI-coated substrate by sputtering the stainless steel target (SUS 304, EIKO Engineering Co., Ltd.). The composition of the deposited thin film was identified as Fe_2O_3/Cr_2O_3 by X-ray photoemission spectroscopy in Sec. 5.3.1. As shown in Fig. 4.1a, the PI-coated substrate was set on the anode (bottom electrode) with a stand for keeping the sample at $\alpha = 60^\circ$ with respect to the horizontal.[2] A stainless steel pad was mounted

---

[1] Several materials were tested for LC surface alignment in early studies. For instance, a deposited film from gold pad presents a homogeneous alignment (see Sec. 4.3.2). Only a deposited film from a stainless steel target had a precise LC pretilt angle controllable property.

[2] The pretilt angle changes under various deposition angle were studied. In this thesis, all cells for the LC studies and surface investigations were prepared at $\alpha = 60^\circ$, which can control the pretilt angle in a parallel alignment region ($\theta_p = 0^\circ \sim 45^\circ$).

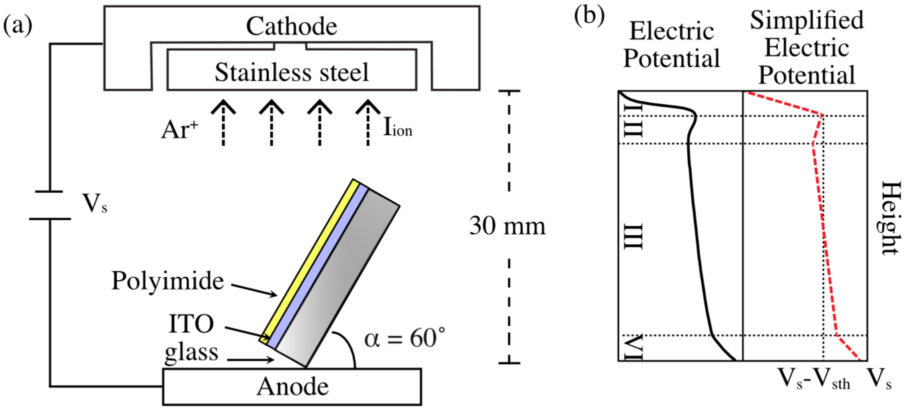

Figure 4.1: The ion beam sputter (a) setup and (b) the electric potential distribution between anode and cathode [22]. The electric potential distribution (black solid line) is linearly simplified (red dash lines) in four regions (I, II, III, and IV) which is used for calculating the sputtering electric potential energy in Sec. 4.3.3.

on the cathode (top electrode) as the sputtering target. Several pairs of substrates were prepared under various conditions, including deposition times t_d (5 ~ 120 min), ion beam currents I_{ion} (3 and 5 mA), and sputter voltages V_s (420, 560, and 700 V).

Two Fe_2O_3/Cr_2O_3-deposited substrates were combined as an anti-parallel (AP) alignment cell and sandwiched with 23 µm mylar spacers (see Fig. 3.2).[3] The empty cells were filled with 4'-n-pentyl-4-cyanobiphenyl (5CB, Merck) at 60°C and annealed to room temperature.

4.3 Results and discussions

4.3.1 Alignment and pretilt angle

To characterize the LC alignment, we first used a polarizing optical microscope (POM) which is widely used for LC alignment investigations (see Sec. 3.3.1). At the setup in Fig. 3.3a, by observing the texture of the cell between a pair of crossed polarizers, the LC orientation can be identified [24, 25]. In our study, the 5CB cell is in the nematic phase at room temperature. In a planar or tilted nematic liquid crystal (NLC) alignment cell, dark and bright states correspond to the relative LC orientation

---

[3] Most of the commercial LCDs use from 4 to 10 µm as the LC thickness to get a fast optical response speed [23]. In our case, it is hard to determine precisely high pretilt angles ($\theta_p > 20°$) for such thin thickness. Therefore, in only this Ch. 4, we made the cell 23 µm thick for precise pretilt angle measurement.

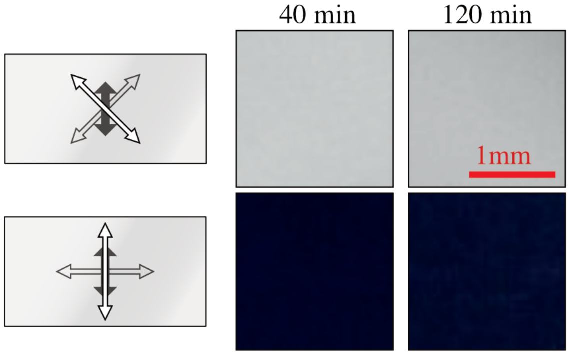

Figure 4.2: The POM textures of the cells prepared with 40 and 120 minutes Fe_2O_3/Cr_2O_3 deposition times. The white arrows are the polarization directions of polarizer and analyzer. The black arrows are the projection of the depostion direction on the substrate.

at 0° and 45° with respect to the crossed polarizers, because of the phase retardation acquired by the linear polarized light after passing through the sample. On the other hand, in a homeotropic NLC alignment cell, no matter the orientation of the cell at 0° or 45° relative to the crossed polarizers, the cell only exhibits the dark state because there is no induced phase retardation since the LC molecules align vertically.

The LC cells were prepared keeping constant the sputtering voltage $V_s = 560$ V and ion beam current $I_{ion} = 5$ mA and varying the Fe_2O_3/Cr_2O_3 deposition times t_d from 5 to 120 min. All samples presented a uniform planar or tilted alignment (see the texture types in Fig. 3.3). Figure 4.2 shows two POM images of the 5CB cells corresponding to two different Fe_2O_3/Cr_2O_3 deposition times. The projection of the LC director on the substrate is along the projection of the deposition direction on the substrate. It is visible that, despite of the fact that the substrate is prepared by obliquely depositing Fe_2O_3/Cr_2O_3 on a "non-rubbed" polyimide thin film, the cells also presented a uniform director just as a "rubbed" polyimide cell. Furthermore, the pretilt angles of these 5CB cells were measured and analyzed by using the "crystal rotation method" (see Sec. 3.3.2) [26]. As shown in Fig. 4.3, the pretilt angle was directly proportional to the Fe_2O_3/Cr_2O_3 deposition time up to 80 minutes and then it saturated at about 45° for longer deposition times.

So far, the POM images and the pretilt angle changes showed that the oblique deposition Fe_2O_3/Cr_2O_3 thin film presents a homogenous or tilted alignment layer and the pretilt angle could be controlled by tuning the deposition time. It provides a valid method to simply control the LC alignment along both azimuthal and polar angle.

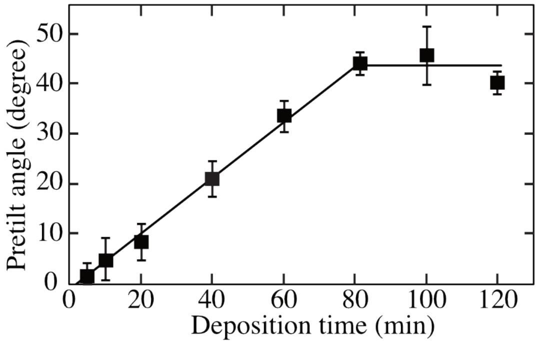

Figure 4.3: The pretilt angle measurements of different LC cells as a function of the Fe_2O_3/Cr_2O_3 deposition time. The squares are the experimental data while the line is a linear fit, resulting from the short deposition time region ($t_d \leq 80$ min), and the height of the flat part is the average of the pretilt angle after 80 minutes deposition time. For each Fe_2O_3/Cr_2O_3 deposition time, we prepared three samples and measured their pretilt angles. The data and the error bar are the average and the standard deviation, respectively, of three samples of each deposition time.

4.3.2 Roles of Fe_2O_3/Cr_2O_3 on polyimide and oblique deposition

In order to investigate the roles of each coated layer and the oblique deposition process, we prepared three kinds of samples (see Fig. 4.4), namely, (1) gold sample, (2) non-polyimide sample and (3) vertically deposited sample, respectively, under the standard sputtering conditions of $V_s = 560$ V and $I_{ion} = 5$ mA.

Gold sample: After replacing the stainless steel target by a gold pad, the "gold sample" was prepared by the standard procedure with the same sputter machine. Gold obliquely deposited on a PI-coated substrate was investigated to see if we could obtain the same control of the LC pretilt angle. However, as shown in Fig. 4.4a, the POM images indicate that the gold sample only gives a homeotropic alignment. This demonstrates the fact that the surface composition of the deposited layer has an essential role in controlling the pretilt angle.

Non-polyimide sample: In this sample, Fe_2O_3/Cr_2O_3 was directly obliquely deposited on an ITO glass. There was no polyimide layer in this substrate. Fig. 4.4b presents the POM images of the cell with a 20 minutes deposition time. It shows a uniform homeotropic alignment.

Vertically deposited sample: In this sample the substrates were set horizontally on the bottom electrode plate ($\alpha = 0°$, see Fig. 4.1a). This means that the Fe_2O_3/Cr_2O_3 thin film was deposited vertically on the PI-coated substrate. As shown in Fig. 4.4c, for the cell with 20 minutes deposition time, a clear random planar texture was ob-

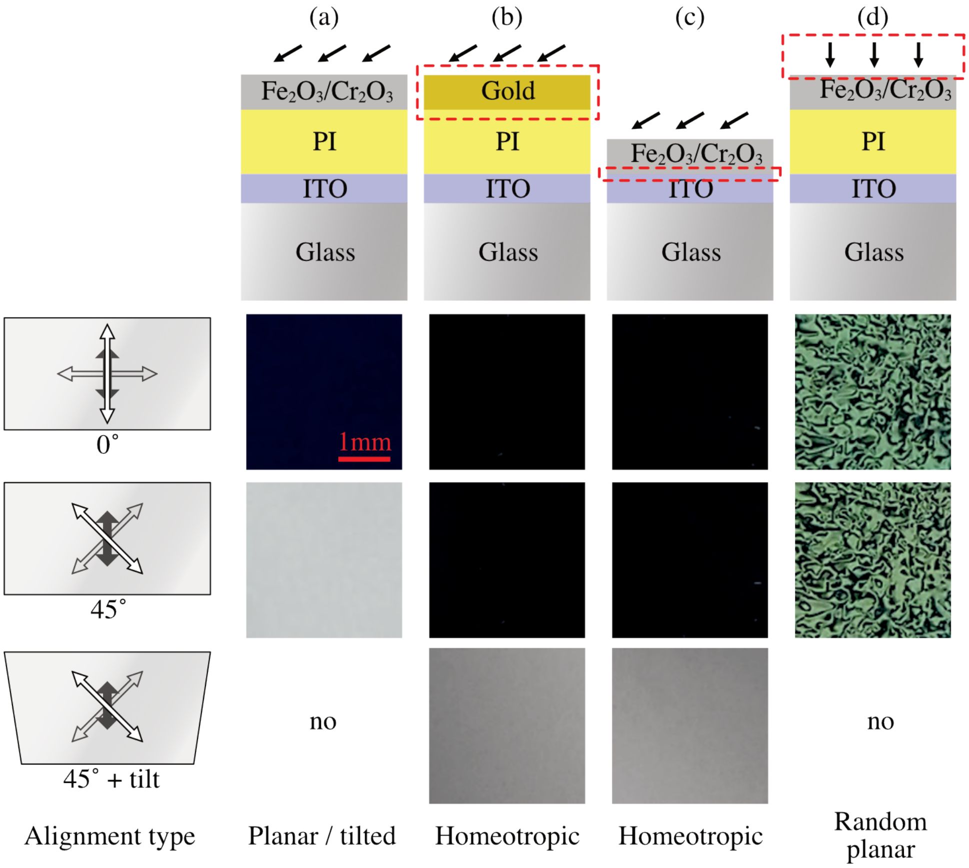

Figure 4.4: The POM images of (a) standard sample, (b) gold sample, (c) non-polyimide sample, and (c) vertically deposited sample. The red dashed rectangles point out the difference between the cell and the standard cell. The white arrows are the polarization directions of polarizer and analyzer. The black arrows are the projection of the deposition direction on the substrate. "no" means that the POM image is unnecessary to be taken for LC alignment characterization. In (b) and (c), the cells only exhibit dark states which means the cell cannot induce any phase retardation. In this case, there are two possible alignments, homeotropic and isotropic, in which the LC molecules orient vertically and randomly, respectively, to the substrate. To distinguish these two types, the cell was observed with a small tilt angle with respect to the substrate. The brightness state will be acquired because the phase retardation generated from the tilted LC. In this study, only standard cell in (a) present a pretilt angle controlled alignment.

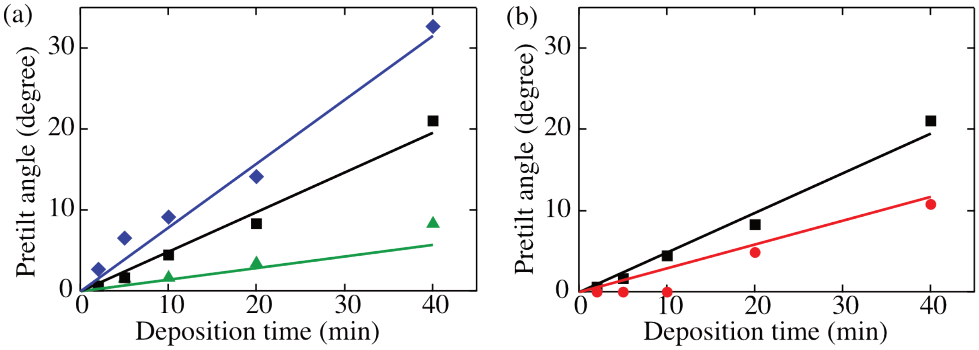

Figure 4.5: The pretilt angle as function of deposition time of the substrates prepared under different (a) sputtering voltages and (b) ion beam current. Symbols are the experimental data and lines are the predicted pretilt angles from Eq. 4.6 by using coefficients $C_1 = 0.047$ deg/J and $V_{sth} = 333$ V.

served by using POM.

According to the above-mentioned different alignment behaviours[4], the two main parameters of the pretilt angle control are: (1) Fe_2O_3/Cr_2O_3 on polyimide and (2) oblique deposition.

4.3.3 Pretilt angles under various sputtering conditions

To get more insight into the sputtering process, we studied the relations between the pretilt angles and various sputtering conditions, including sputtering voltages V_s and ion beam currents I_{ion}. Moreover, this study can help us to shorten the deposition time which is very important to improve the fabrication productivity in the LCD industry. In this section, several sets of cells were prepared for three different sputtering voltages $V_s = 420$, 560 and 700 V and two different ion beam currents $I_{ion} = 3$ and 5 mA, respectively.

Figure 4.5 shows that the pretilt angle was proportional to the deposition time, either for various sputtering voltages or ion beam currents. The higher pretilt angle always corresponds to the higher sputtering voltage $V_s = 700$ V and ion beam current $I_{ion} = 5$ mA. In an attempt to determine the relation between pretilt angle and various sputtering conditions, the concept of the electric potential energy U_E was introduced. We will use the electric potential energy as a bridge to connect the pretilt angle and various sputtering conditions.

---

[4] In fact, for each kind of samples, we prepared and observed many cells with various deposition times. But no dependence of the pretilt angle control on the pretilt angle was found. Therefore, we only show three examples in this Sec. 4.3.2.

Sputtering electric potential energy U_E

As shown in Fig. 4.1b, the black solid line is the electric potential distribution at different heights in the plasma sputter chamber [22]. The red dashed line is the linearly simplified electric potential distribution in four regions. The electric potential distribution shows that the argon ion on the boundary between region I & II is in a local maximum of the electric potential close to the target. It means that the argon ions will accelerate within region I. Thus, the sputtering electric potential energy U_E can be written as

$$U_E = \int_0^L q \, E(z) \, \mathrm{d}z = \int_0^L i(z) \, t_d \, E \, \mathrm{d}z \tag{4.1}$$

where E is the electric field , t_d is the deposition time which is equal to the sputtering time, L is the length of region I, q is the total amount of argon ions sputtering the target during the deposition process, and $i(z)$ is the current distribution at the height z in the chamber. The electric field E and the current distribution $i(z)$ can be written as

$$i(z) = I_{ion} \, e^{-z/l}, \quad E = \frac{(V_s - V_{sth})}{L} \tag{4.2}$$

where V_s and I_{ion} are the sputtering voltage and ion beam current, V_{sth} is the sputtering threshold voltage which is the voltage difference between the cathode and the boundary between region I & II (see Fig. 4.1b)[5], L is the length of region I which is comparable to the mean free path l. [6] The relation between the sputtering electric potential energy and the sputtering conditions (Eq. 4.1) can be derived as

$$U_E = U_{E,0} \, (V_s - V_{sth}) \, I_{ion} \, t_d \tag{4.3}$$

where $U_{E,0}$ is a constant which will be used to normalize the electric potential energy U_E in Fig. 4.6b. Here, the problem is how to obtain the value of V_{sth}.

Sputtering threshold voltage V_{sth}

Sputtering Threshold Voltage V_{sth} can be estimated by examining the relation between the sputter machine parameters, sputtering voltage V_s and ion beam current I_{ion}. In the sputter chamber, the current density distribution $J(z)$ can be written as [27]

$$J(z) = (\frac{n \, f(z) \, \lambda \, q^2}{2 \, m \, v_{thermal}}) \, E \tag{4.4}$$

where n is the number of molecules per unit volume and f is the number of free electrons per molecule, each molecule is characterized by a charge q and a mass m,

---

[5] Here we called “sputtering threshold voltage” and noted it as V_{sth} for distinguishing from the threshold voltage V_{th} which will be discussed in Ch. 6 and 7.

[6] According the operating pressure P∼ 0.1 torr, the electron mean free path can be estimated to be c.a. 1 mm.

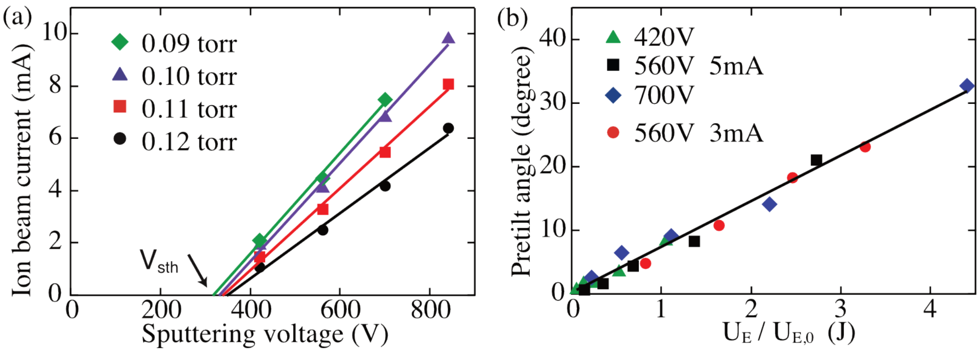

Figure 4.6: (a) The ion beam current as function of sputtering voltage at four different chamber pressures. Here $V_{sth} = 333 \pm 13$ V. (b) The experimental result of the pretilt angle as function of the sputtering electric potential energy. We can obtain $C_1 = 0.047$ in Eq. 4.6 by determining the slope of the fitting line.

λ is the mean free path, $v_{thermal}$ is the thermal velocity, and E is the electrical field which can be derived as $E = (V_s - V_{sth})/L$. Based on the above equation, the relation between the current I_{ion}, the chamber pressure P, and the sputtering voltage V_s can be derived as

$$I_{ion} \propto P\,(V_s - V_{sth}). \tag{4.5}$$

As shown in Fig. 4.6a, by fitting the I_{ion}-V_s curves for four different chamber pressures P, we obtained $V_{sth} = 333 \pm 13$ V.

After the determination of V_{sth}, we return to the beginning observation of the relation between the pretilt angle and sputtering conditions As shown in Fig. 4.6b, by expressing U_E as a function of V_s and I_{ion} (Eq. 4.3), the experimental results show that the pretilt angle is perfectly proportional to the normalized sputtering electric potential energy. In Fig. 4.6b, different sputtering conditions are presented as different colors and shapes. Furthermore, based on the analyzed experimental results and Eq. 4.3, the pretilt angle can be approximated as

$$\theta_p = \mathrm{C}_1\, I_{ion}\, (V_s - V_{sth})\, t_d \tag{4.6}$$

where $\mathrm{C}_1 = 0.047\mathrm{deg/J}$ is a constant which can be derived from the slope in Fig. 4.6b. In this equation, the sputtering threshold voltage V_{sth} depends on the design and the structure of the sputtering machine. It can be obtained directly from the I_{ion}-V_s curve of the sputtering machine (see Fig. 4.6a). The constant C_1 is the only fitting parameter in the pretilt angle experiment.

As shown in Fig. 4.5, the predicted pretilt angles which are derived by using Eq. 4.6 (lines) are in perfect agreement with the experimental results (symbols) by using the fitting parameter $C_1 = 0.047$ deg/J. Therefore, according to Eq. 4.6, for a cell with the same pretilt angle θ_p, a shorter deposition time t_d can be achieved by applying a high sputtering voltage V_s and ion beam current I_{ion} for the Fe_2O_3/Cr_2O_3 thin film deposition process.

4.4 Conclusion

In this chapter, we demonstrated that the single-domain pretilt angle could be controlled by an obliquely deposited Fe_2O_3/Cr_2O_3 thin film on a PI-coated ITO substrate. Pretilt angles between 0° and 45° were obtained by finely tuning the Fe_2O_3/Cr_2O_3 deposition time and sputtering conditions. The two main mechanisms of the pretilt angle control were found as: (1) Fe_2O_3/Cr_2O_3 on polyimide and (2) oblique deposition. Furthermore, the relation between the pretilt angle and the sputtering conditions was derived and investigated. We found that to get a higher fabrication productivity, a shorter deposition time can be achieved while we apply a higher sputtering voltage and ion beam current. Since sputtering is a well-known and mature technique, these results present a simple and practical solution to achieve a precise control of the pretilt angle in LC devices.

References

[1] K. Takatoh, M. Hasegawa, M. Koden, N. Itoh, R. Hasegawa, and M. Sakamoto, *Alignment Technology and Applications of Liquid Crystal Devices* (CRC Press, 2005).

[2] H.-S. Kwok, S. Naemura, and H. L. Ong, *Progress in Liquid Crystal Science and Technology*, In Honor of Shunsuke Kobayashi's 80th Birthday (World Scientific, 2013).

[3] G. Meier, E. Sackmann, and J. G. Grabmaier, *Applications of Liquid Crystals* (Springer Science & Business Media, 2012).

[4] C. C. Lin, C. Ye, H. L. Hou, C. Y. Lee, R. Xie, G. Chen, and F. Yang, SID Symposium Digest of Technical Papers **43**, 965 (2012).

[5] M. Oh-e and K. Kondo, Applied Physics Letters **69**, 623 (1996).

[6] M. F. Schiekel and K. Fahrenschon, Applied Physics Letters **19**, 391 (1971).

[7] F. S. Yeung, Y. W. Li, and H.-S. Kwok, Applied Physics Letters **88**, 041108 (2006).

[8] X. Nie, H. Xianyu, R. Lu, T. X. Wu, and S.-T. Wu, Journal of Display Technology **3**, 280 (2007).

[9] J.-W. Kim, D. H. Song, K.-H. Kim, S. T. Shin, and T.-H. Yoon, Applied optics **52**, 5256 (2013).

[10] Y.-K. Moon, Y.-J. Lee, C.-J. Yu, J. Uk Heo, J.-H. Park, H. jin Lee, S. Tae Shin, and J.-H. Kim, Journal of Applied Physics **112**, 014512 (2012).

[11] Y. Koike and K. Okamoto, Fujitsu Science Technical Journal **35**, 221 (1999).

[12] K.-H. Kim, E.-Y. Jeon, B. W. Park, S.-W. Choi, D. H. Song, H. Kim, K.-C. Shin, H. S. Kim, and T.-H. Yoon, Journal of the Optical Society of Korea **16**, 166 (2012).

[13] T. Rasing and I. Musevic, *Surfaces and Interfaces of Liquid Crystals* (Springer Science & Business Media, 2013).

[14] M. K. Ghosh and K. L. Mittal, *Polyimides: fundamentals and applications* (CRC Press, 1996).

[15] Y. Koike, T. Kamada, K. Okamoto, M. Ohashi, I. Tomita, and M. Okabe, SID92 DIGEST **23**, 798 (1992).

[16] J. L. Janning, Applied Physics Letters **21**, 173 (1972).

[17] T. Uchida, M. Ohgawara, and M. Wada, Japanese Journal of Applied Physics **19**, 2127 (1980).

[18] L. A. Goodman, J. T. McGinn, C. H. Anderson, and F. DiGeronimo, Electron Devices, IEEE Transactions on **24**, 795 (1977).

[19] A. Tixier, Y. Mita, J. P. Gouy, and H. Fujita, Journal of Micromechanics and Microengineering **10**, 157 (2000).

[20] P. Chaudhari, J. Lacey, J. Doyle, E. Galligan, S. Lien, J. Lacey, J. Doyle, E. Galligan, S.-C. A. Lien, A. Callegari, G. Hougham, N. D. Lang, P. S. Andry, R. John, K.-H. Yang, M. Lu, C. Cai, J. Speidell, S. Purushothaman, J. Ritsko, M. Samant, J. S. hr, Y. Nakagawa, Y. Katoh, Y. Saitoh, K. Sakai, H. Satoh, S. Odahara, H. Nakano, J. Nakagaki, and Y. Shiota, Nature **411**, 56 (2001).

[21] H.-Y. Wu and R.-P. Pan, Applied Physics Letters **91**, 074102 (2007).

[22] *Sputter Coating Technical Brief*, Quorum Technologies Ltd. (2002).

[23] E. Jakeman and E. P. Raynes, Physics Letters A **39**, 69 (1972).

[24] T. Scharf, *Polarized Light in Liquid Crystals and Polymers* (John Wiley & Sons, 2007).

[25] I. Dierking, *Textures of Liquid Crystals* (John Wiley & Sons, 2006).

[26] T. J. Scheffer and J. Nehring, Journal of Applied Physics **48**, 1783 (1977).

[27] D. J. Griffiths, *Introduction to Electrodynamics*, 3rd ed. (Prentice-Hall, 1999).

CHAPTER 5

LC Alignment Surface Investigations

5.1 Introduction

Surface alignment layers play an major role in liquid crystal displays (LCDs). As introduced in Sec. 2.3.5, many surface studies have focused on new liquid crystal (LC) alignment layers and their alignment mechanisms. In Ch. 4, we have demonstrated how to control the pretilt angle precisely with an obliquely deposited Fe_2O_3/Cr_2O_3 thin film on a polyimide-coated indium-tin-oxide (ITO) glass. The pretilt angle can be controlled continuously between 0° and 45° by varying the Fe_2O_3/Cr_2O_3 deposition time. However, the microscopic origin of the alignment effect was still not clear.

In previous studies, several physical and chemical LC alignment mechanisms were reported; for instance, the effects of microgrooves [1–5], sp/sp2 chemical bonds [6, 7], polymer long chains [8], and the layer structure of the alignment substrate [9, 10]. It is hard to determine the LC alignment mechanism because the LC molecules are too small (∼nm) to control and observe individually. So, we prepared several substrates under the same Fe_2O_3/Cr_2O_3 deposition condition. For each deposition condition, two of the substrates were used to make an LCD cell for the pretilt angle measurements. The rest of the substrates were used for detailed surface studies. With this, we tried to find a correlation between the pretilt angle and the surface conditions.

Two surface investigation techniques were used: atomic force microscopy (AFM) and X-ray photoemission spectroscopy (XPS) [11]. The AFM images show the morphology on a nanometer scale which involves the surface groove structure and roughness. The XPS is widely used for surface chemical quantitative analysis which can provide information to identify the deposited material types and analyze their compositions [12].

In this chapter, the LC alignment effects were investigated by comparing the surface changes with the pretilt angle changes. Several aspects were taken into consideration: the topography, the surface chemical nature, the chemical bond changes, and the surface composition. The study target of each section is listed in Table 5.1.

Method	Scale	Observation target	Section
AFM	nm	Topography	5.3
XPS	Surface	Surface chemical nature	5.4.1
	(1-10 nm depth)	Chemical bond change	5.4.2
		Surface composition	5.4.3

Table 5.1: Surface observation methods and their observation targets in this study.

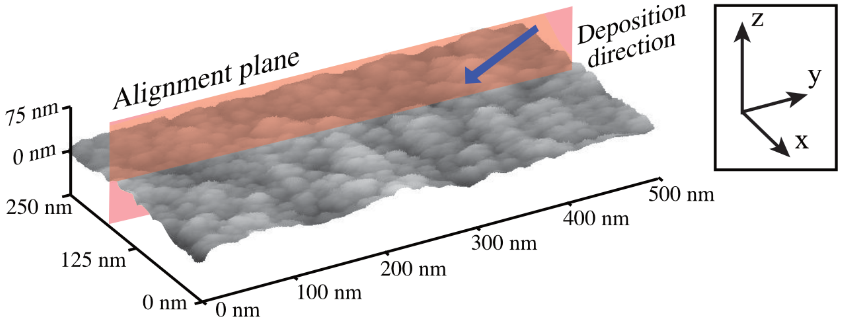

Figure 5.1: AFM 3D image and the geometrical structure of the deposition direction (blue arrow). It is a substrate with 60 minutes Fe_2O_3/Cr_2O_3 deposition time. The red plane is called the alignment plane because the pretilt angle changes on this plane.

5.2 Sample and substrate

Following the preparation steps described in Sec. 3.2, the substrates were spin-coated with a polyimide thin film and then a Fe_2O_3/Cr_2O_3 thin film was obliquely deposited by sputtering from the stainless steel target. The sputtering voltage and ion beam current were fixed at 560 V and 5 mA, respectively. The substrates were prepared under various deposition times ($t_d = 0 \sim 120$ minutes). The surface of the substrate was observed directly without the cell combination process as reported in Ch. 4.

5.3 Topography and roughness - AFM

The surface morphology, for instance, the surface structures and grooves, might influence the LC alignment [13, 14]. In our substrate preparation, substrates were coated with polyimide and Fe_2O_3/Cr_2O_3 thin film, in that order. For the polyimide layer, Pidduck et al. reported the effect of the induced LC alignment by the grooves that are created by rubbing the polymer surface [15]. For the oxide layer, Goodman et al. reported the LC alignment to originate from the surface shape which was generated by the self-shadowing mechanism of the silicon oxide layer [16]. Both above described LC alignment effects of the polymer and oxide layer were referred to achieve the minimum elastic energy.

The topography of the substrates were studied by using an AFM (Dimension 3100 AFM, Veeco) under the tapping mode (see Sec. 3.4.1) to investigate the relation between morphology and the LC pretilt angle. As shown in Fig. 5.1, the scan size is 250 nm × 500 nm with a 1 nm × 1 nm scan resolution. All the substrates were prepared by following the standard steps as described in Sec. 3.2.2.

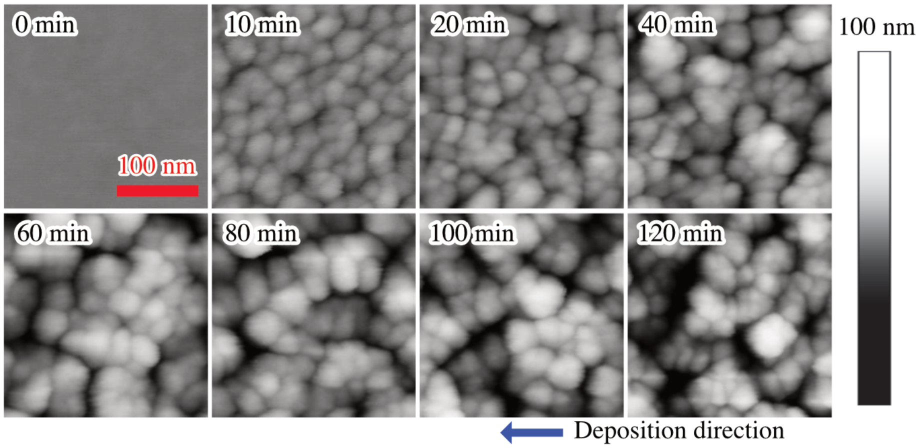

Figure 5.2: AFM height images of the substrates with different Fe_2O_3/Cr_2O_3 deposition times. "0 min" is a non-rubbed polyimide substrate.

As shown in Fig. 5.2, the PI-coated substrate (0 min) is relatively flat. As the Fe_2O_3/Cr_2O_3 deposition time increases, the AFM image shows that the deposited layer is not flat but characterized by a rough surface. On rubbed surfaces, the grooves had been founded [1, 3] and the LC molecules orient along to grooves to reach the minimum of the free energy. However, no groove was found on our PI-coated substrate because there was no rubbing process in our sample preparation. For each deposition time, we scanned at least three areas on the different locations of the substrates and tried with different scan sizes to few µm, but also no groove was found on the sputtered substrate.

According to the observation in the pretilt angle measurement (see Sec. 4.3.1), the LC molecules were found to align in the alignment plane which is vertical to the substrate and parallel to the deposition direction (the red plane in Fig. 5.1). Therefore, we further studied the cross section of the alignment plane (see the red plane in Fig. 5.1). In Fig. 5.3a and b, to get better surface information, the scale of the **z**-axis is expanded. According to the surface composition study in the following Sec. 5.4.3, a 60 minutes deposited substrate is already fully covered with an Fe_2O_3/Cr_2O_3 layer. However, no directional surface structures or specific shapes appeared on the deposited substrate (see Fig. 5.3b).[1] So far, it seems that there are no grooves or surface structures which can influence the LC molecules on our substrate.

Furthermore, we analyzed the roughnesses of these surfaces by using the AFM software (nanoscope, Veeco). The roughness is calculated as the arithmetic average

---

[1] We also analyzed the slope distributions, but no geomorphologic asymmetries were found.

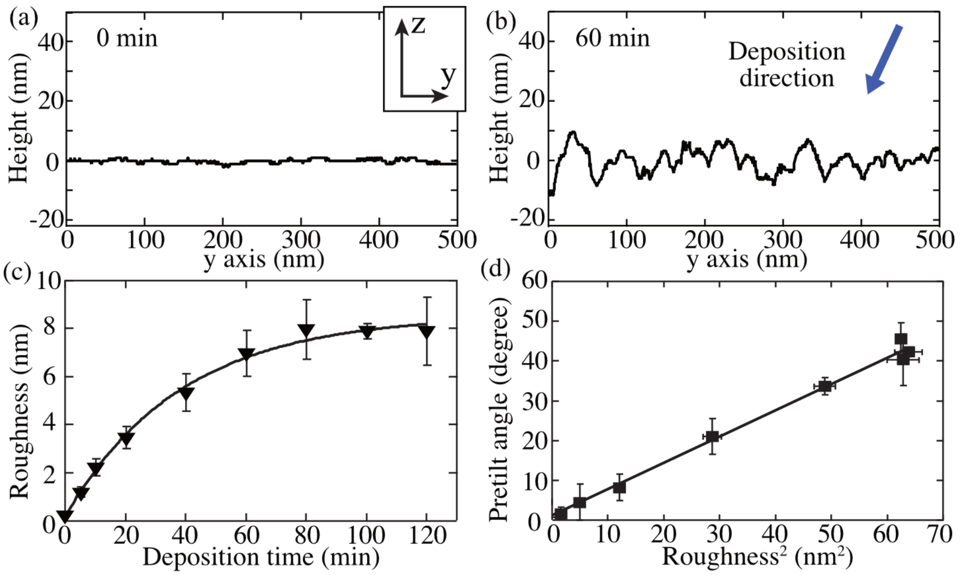

Figure 5.3: Cross sections of substrates with (a) 0 minute and (b) 60 minutes Fe_2O_3/Cr_2O_3 deposition times. The cross section comes from the alignment plane (see Fig. 5.1). Note that because the **z** axis is expended to get clear surface information, the deposition direction in (b) is not along to 30° respect to the substrate. (c) The roughness as a function of the deposition time. (d) The pretilt angle as a function of the roughness squared. In each deposition time, three substrates were prepared and observed. The error estimation is the standard deviation of the roughness in three substrates.

of the absolute height of the AFM profiles (the baseline is the average height) as a function of the deposition time. As shown in Fig. 5.3c, the roughness of the surface profile increases with the deposition time and it saturates after 80 minutes. This strongly correlates with the pretilt angle behavior shown in Fig. 4.4. The pretilt angle and the surface roughness both increase with Fe_2O_3/Cr_2O_3 deposition time and saturate after 80 minutes. More precisely, we found that the pretilt angle θ_p is proportional to the square of the roughness R_a ($\theta_p \propto R_a^2$) (see Fig. 5.3d).

Goodman et al. reported that an obliquely deposited silicon oxide film can align LC molecules due to the specific surface shape and structure [16]. In our case, an obliquely deposited Fe_2O_3/Cr_2O_3 film on PI-coated substrate also aligns LC molecules. Moreover, they found a random parallel LC alignment on a silicon oxide film deposited in a normal direction, which is similar to our finding of the vertically depositing sample in Sec. 4.3.2. Therefore it is clear that our obliquely depositedFe_2O_3/Cr_2O_3film will have an anisotropic surface structure that is responsible for the LC alignment, though we could findno grooves in our AFM studies. However, so far, we have found a clear correlationbetween the pretilt angle and the square of the roughness. Further studies will be needed to explain this correlation.

5.4 Surface chemical nature - XPS

Here, we used XPS (PHI-1600 from Physical Electronics, Inc.) for the elemental and chemical state analysis. In a typical XPS experiment, X-rays irradiate the substrate surface and the photo-emitted electrons escaping from the top surface (1∼10 nm depth, few electron mean free paths in the substrate) are detected. By counting the number of electrons and measuring their kinetic energies, the chemical and electronic state can be characterized by the peak positions of the binding energy (BE) spectrum. The details and analysis methods of XPS were introduced in Sec. 3.4.2. For getting a better signal in the XPS investigation, the polyimide thin film was coated on the glass side of the ITO-glass to avoid the ITO signal.

5.4.1 Surface element overview

First, the elements were identified by the XPS spectrum, scanned as a function of the binding energy from 0 to 1100 eV in the survey mode with a 1 eV step size. As indicated in the yellow regions shown in Fig. 5.4a, the wide-scan XPS spectra showed

Element	Orbital State	Binding Energy (eV) in our study	Binding Energy (eV) from literatures	Reference
O	1s	530.0 - 533.2	529.8 - 533.3	[20–30]
C	1s	284.8	284.4 - 288.5	[28–32]
N	1s	400.3	400.2 - 400.6	[28, 30]
Fe	$2p_{3/2}$	711.1	706.7 - 711.5	[23, 24, 33, 34]
	$2p_{1/2}$	724.5	719.9 - 724.6	
Cr	$2p_{3/2}$	576.8	574.3 - 579.6	[25, 26, 33, 35]
	$2p_{1/2}$	586.7	583.5 - 588.7	

Table 5.2: Binding energy comparison for different elements between experimental results (see yellow regions in Fig. 5.1a) and data in relational references. The binding energy was reported in a few eV range because the binding energy of the element is shifted for different compounds. According to compare the peak position with literature data, the compound type can be identified and showed in following sections.

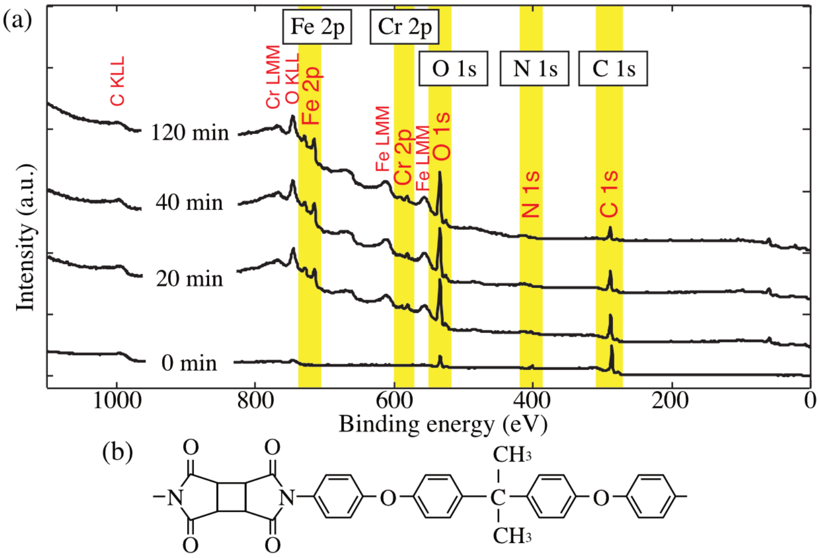

Figure 5.4: (a) XPS spectra for the substrates with different Fe_2O_3/Cr_2O_3 deposition times. For each element, the peaks can be found with different electron configurations in different binding energies. The peak positions of the main states of the elements (see Table 5.2) which is used for further analysis are marked in yellow regions. (b) Polyimide repeated unit which contains C, O, N.

that the main elements which were present on the surface for different deposition times are carbon (C), oxygen (O), nitrogen (N), iron (Fe), and chromium (Cr). The corresponding binding energies are listed in Table 5.2. In each element, the peaks can be found with different electron configurations at different binding energies. Moreover, not all peaks come from the electrons which are directly ejected by the incident photon, for instance, C KLL and Fe LMM (see Fig. 5.4a) [36]. In this thesis, we only chose the main states listed in Table 5.2 for a detailed quantitative analysis.

In Fig. 5.1a, the PI-coated sample (0 min) only has signals of C, N and O, which come from the polyimide layer (see Fig. 5.4b). On the other hand, the Fe and Cr signal only appear in the sputtering deposition substrates, which means the Fe and Cr elements were sputtered from the stainless steel.[2] To further investigate the main peaks, we rescanned the spectra of five main peak ranges (see the yellow regions in Fig. 5.4a) with a 0.2 eV step size.

---

[2] In the stainless steel, the rapid chromium oxidation plays an important role in the protection layer on the surface. The iron is isolated by the protective chromium oxide layer to avoid the iron reactions with oxygen and moisture. The compositions of a SUS 304 stainless steel target contains mainly iron and a 18% minimum of chromium.

Fe

First, we focused on the Fe peak signals. As listed in Table 5.3, there are several possible Fe chemical configurations in our substrate, such as Fe metal, FeO, Fe_2O_3, Fe_3O_4, $FeCO_3$ and FeOOH. As shown in Fig. 5.5, the Fe 2p peak can be fitted separately into three sub-peaks which corresponds to Fe $2p_{3/2}$ (711.1 eV), Fe $2p_{3/2,sat}$ (719.0 eV), and Fe $2p_{1/2}$ (724.5 eV). In the first step, two types of Fe (metal) and Fe_3O_4 can be excluded directly because they have no satellite peak (see the middle part in Table 5.3) which appeared in our study at 719.0 eV. More in detailed, different Fe compounds have their specific spectrum which can be identified by the center positions of the sub-peaks. After comparing the sub-peak positions with the literature data (see Table 5.3), only Fe_2O_3 is close to our data with a low binding energy difference ($\overline{|\Delta \mathrm{BE}|} = 0.2$ eV). The Fe 2p peak signal belongs to Fe_2O_3.

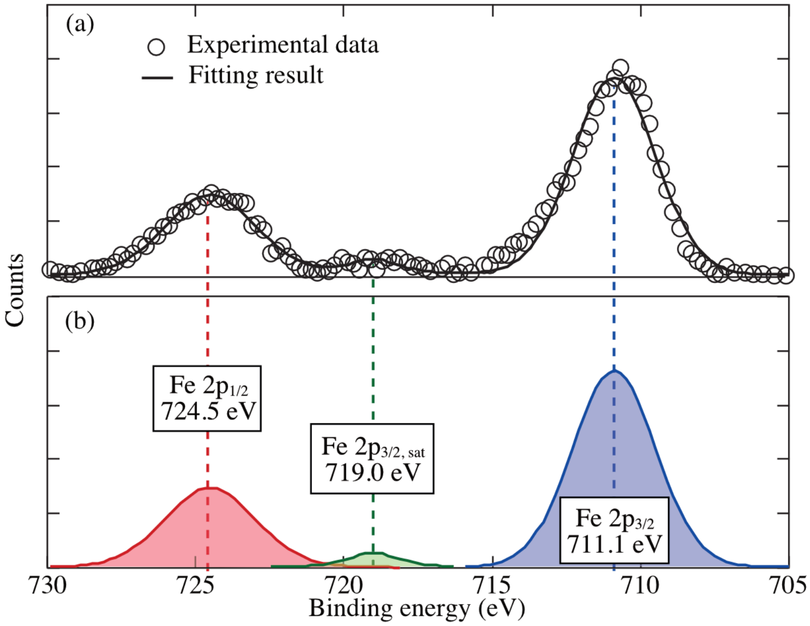

Figure 5.5: The Fe 2p XPS spectrum of (a) experimental result and the summation of fitting peaks and (b) fitting sub-peaks. The experimental Fe 2p signal contains three peaks. According to the peak positions, they were distinguished to belong to Fe $2p_{3/2}$, Fe $2p_{3/2,sat}$ and Fe $2p_{1/2}$. Here Fe $2p_{3/2,sat}$ is the satellite line of the main photoelectron line Fe $2p_{3/2}$. More in detailed, the center positions of the peaks are located at 711.1 eV (Fe $2p_{3/2}$), 719.0 eV (Fe $2p_{3/2,sat}$), and 724.5 eV (Fe $2p_{1/2}$). By comparing the peak positions with literatures (see Table 5.3), we conclude that the Fe 2p peak signal belongs to Fe_2O_3.

Compound	$\overline{\lvert\Delta \mathrm{BE}\rvert}^{a}$	BE $(\Delta\mathrm{BE})^{b}$			Ref
		Fe $2p_{3/2}$	Fe $2p_{3/2,sat}$	Fe $2p_{1/2}$	
This study		**711.1**	**719.0**	**724.5**	
Fe_2O_3	0.2	710.9 (-0.2)	719.3 $(+0.3)$	-[c]	[24]
		710.9 (-0.2)	719.4 $(+0.4)$	-	[23]
		711.2 $(+0.1)$	719.2 $(+0.2)$	724.6 $(+0.1)$	[34]
Fe (metal)	no sat	706.7 (-4.4)	no[d]	719.9 (-4.6)	[23, 33]
		706.9 (-4.2)	no	720.0 (-4.5)	[34]
Fe_3O_4 (Fe^{3+})	no sat	710.8 (-0.3)	no	723.9 (-0.6)	[34]
		710.8 (-0.3)	no	-	[23]
		711.4 $(+0.3)$	no	-	[24]
Fe_3O_4 (Fe^{2+})	2.6	709.0 (-2.1)	714.9 (-4.1)	-	[24]
		709.5 (-1.6)	-	-	[23]
FeO	1.7	710.1 (-1.0)	715.7 (-3.3)	723.6 (-0.9)	[34]
$FeCO_3$	1.4	710.7 (-0.4)	715.2 (-3.8)	724.4 (-0.1)	[34]
FeOOH	0.4	710.4 (-0.7)	718.9 (-0.1)	724.0 (-0.5)	[34]
		710.9 (-0.2)	719.4 $(+0.4)$	-	[23]
		711.5 $(+0.4)$	719.7 $(+0.7)$	-	[24]

Table 5.3: Comparison of binding energy peak positions (in eV) of Fe between our experimental data and literature results. Large binding energy difference ΔBE (≥0.5 eV) and no signal are marked in red. The data were separated into three rows. The top row shows the data of our experimental results (This study) and the Fe_2O_3 BE literature data which is closest to our data. The middle part is the compound without Fe $2p_{3/2,sat}$ which can be excluded in our study directly [34, 37]. The bottom part gives the compounds having three peaks with larger ΔBE. All the data in this table were calibrated by the same BE reference (C 1s) at 284.80 eV.

[a] ΔBE is the binding energy difference between literature and this study.

[b] $\overline{\lvert\Delta \mathrm{BE}\rvert}$ is the absolute average of the BE differences in each compound.

[c] "-" indicates that the binding energy value was not provided in the literature.

[d] "no" means that there was no signal in this state.

Cr

According to the analysis method reported from literature [25, 35, 38], the Cr $2p_{3/2}$ and $2p_{1/2}$ signals can be roughly fitted by a sequence of sub-peaks of the different valence states (see Fig. 5.6). First, the presence of Cr metal could be excluded directly because there was no Cr metal $2p_{1/2}$ peak (583.6 eV) and $2p_{1/2}$ (574.4 eV) in our study. Furthermore, after the peak fitting, Cr^{3+} appears to be the main valence state due to the high concentrations of Cr^{3+} $2p_{3/2}$ (93.8%) and Cr^{3+} $2p_{1/2}$ (94.7%). Comparing the Cr^{3+} peak positions to different compounds (see the bottom table in Table 5.4), Cr^{3+} is associated to Cr_2O_3.

Fe_2O_3/Cr_2O_3

After the compound analysis, the deposited thin film from stainless steel sputtering was characterized as Fe_2O_3/Cr_2O_3. To get more detailed information, the XPS can also be used for a more quantitative analysis. The quantitative composition n can be

Compound	BE, Composition[a]				Reference
	Cr $2p_{3/2}$		Cr $2p_{1/2}$		
Cr (metal)	574.3	0.0%	583.5	0.0%	[33]
	574.4		583.6		[25]
Cr^{3+}	576.8	93.8%	586.7	94.7%	[35]
Cr^{6+}	579.6	6.2%	588.7	5.3%	[35]

Compound	BE (ΔBE)[b]				Reference
	Cr $2p_{3/2}$		Cr $2p_{1/2}$		
This study	**576.8**		**586.7**		
Cr_2O_3	576.8	(0.0)	586.5	(−0.2)	[26]
CrO_2	578.3	(+1.5)	587.0	(+0.3)	[26]

Table 5.4: Comparison of Cr binding energy (in eV) between our experimental data and literature results. Large binding energy difference ΔBE (≥0.5 eV) is marked in red. The upper table is the fitting results from Fig. 5.6 and the normalised compositions in $2p_{3/2}$ and $2p_{1/2}$, respectively. The bottom table gives the compounds and their binding energy information. All the data in this table were corrected by the same binding energy reference (C 1s) at 284.80 eV.

[a] Composition is given by the relative areas ratio in each valence state (see Fig. 5.6).

[b] ΔBE is the binding energy difference between literature and this study.

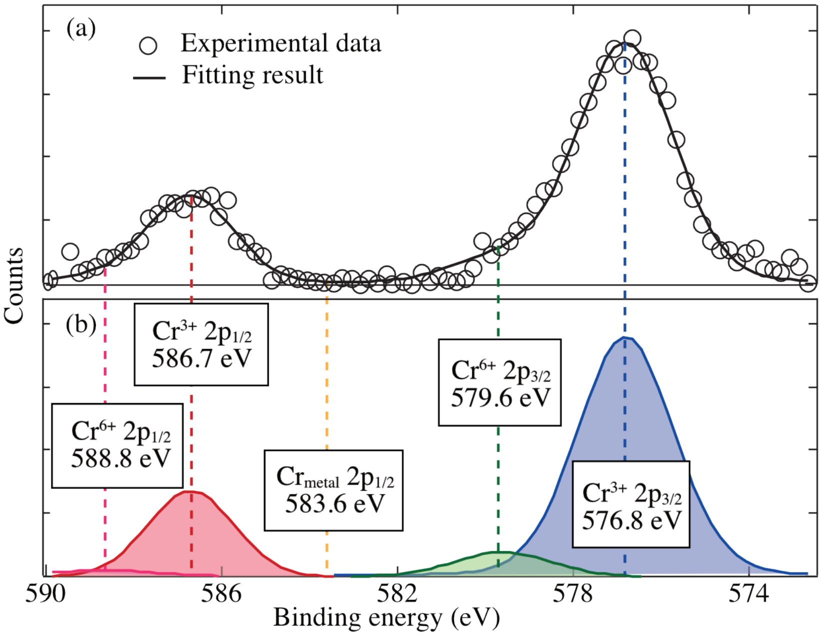

Figure 5.6: The Cr 2p XPS spectrum of (a) experimental result and the summation of fitting peaks and (b) fitting sub-peaks. Cr 2p signal can be roughly fitted by a sequence of sub-peaks of the different valence states, including Cr metal, Cr^{3+}, and Cr^{6+} (see upper table in Table 5.3). Cr metal can be excluded because there is no Cr metal $2p_{1/2}$ peak (orange dashed line at 583.6 eV). After the peak fitting, Cr^3+ results as the main valence state (blue area and red area).

obtained by the following equation

$$n = \mathrm{c}\,\frac{A}{S} \tag{5.1}$$

Here, c is a constant, A is the peak area in the XPS spectrum and S is the relative sensitivity factor [12]. According to literature data, the XPS relative sensitivity factors were 2.0 (Fe $2p_{3/2}$) and 1.5 (Cr $2p_{3/2}$) in relation to F 1s = 1.00 [12]. We analyzed the Fe_2O_3 and Cr_2O_3 compositions of the substrates for different deposition times ($t_d = 10 \sim 120$ min). The average of the normalized compositions was

$$n_{Fe} : n_{Cr} = \frac{A_{Fe}}{S_{Fe}} : \frac{A_{Cr}}{S_{Cr}} = 75\% : 25\% \tag{5.2}$$

with a low standard deviation ($\sim 3\%$).

5.4.2 Chemical bond change of polyimide

During the Fe_2O_3/Cr_2O_3 deposition process, the stainless steel pad was sputtered by the argon ions and deposits Fe_2O_3/Cr_2O_3 on the PI-coated substrate (see Fig. 4.2a). Meanwhile, the generated electron current or deposited Fe_2O_3/Cr_2O_3 particles may modify the PI layer; this may cause the carbon double or triple bonds in polyimide to change which can influence the LC alignment [6]. Thus, the possible carbon compound changes with various deposition times needed to be further investigated.

The deconvolution of the core-level 1s spectrum of carbon (C 1s) was used to observe the chemical bond changes of the surface polyimide in this study. The central position of the C 1s peak is around 284.8 eV. The fine binding energy peak position is slightly shifted depending on the different neighboring atoms (see Table 5.5). The detected C 1s line is the superposition of sub-peaks from various carbon compounds. Following the line of this finding, we identified the compound types and amounts by using the peak-fitting method with the package software (XPSPEAK 4.1). In this case, the C 1s XPS spectrum contains eight binding states (see Fig. 5.7a) which come from the polyimide. Because the full width at half maximum of the C 1s peak of a specific compound ranges from 0.9 to 1.2 eV [30], some carbon compound BE

Group	BE^a (eV)	Compound	BS^b	BE^c (eV)	Reference
Carbon A	284.6	H-Benzene	C1	284.4	[29]
				284.5	[28]
				284.8	[30]
		C (-C) 3(-H)	C2	284.8	[30–32]
Carbon B	285.4	C 3(-C)-H	C3	285.2	[32]
		N-Benzene	C4	285.4	[29]
				285.6	[30]
		C 4(-C)	C5	285.4	[32]
		C-Benzene	C6	285.5	[29]
Carbon C	286.3	O-Benzene	C7	286.2	[29]
				286.4	[30]
Carbon D	288.4	N-C(-C)=O	C8	288.3	[28, 29]
				288.5	[30]

Table 5.5: Binding energies of the C 1s group belonging to different chemical states related to PI.

^{a} Binding energy we used in this study. ^{b} Binding state (see Fig. 5.4a). ^{c} Collected binding energy from literature.

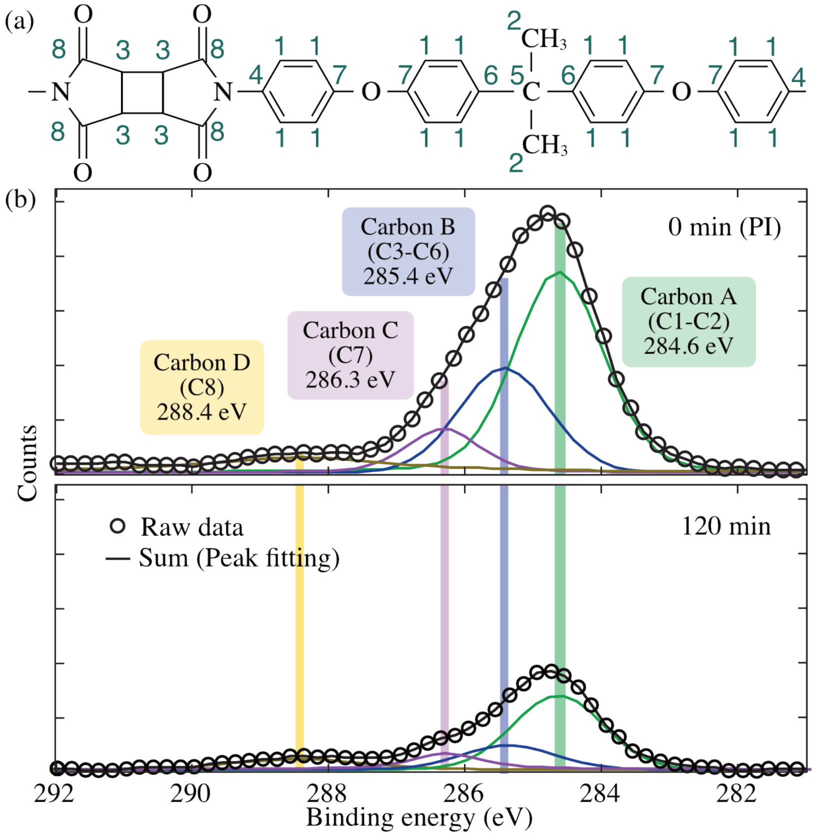

Figure 5.7: (a) Polyimide repeated unit and the binding states of the carbon atoms (C1-C8). (b) XPS spectra of C 1s peak before (0 min) and after (120 min) Fe_2O_3/Cr_2O_3 deposition process. The coloured lines are the peak positions of each carbon group (see Carbon A to D in Table 5.6). The open squares are the experimental data and the black line is the summation of peaks of four carbon groups. The line shapes and the carbon binding energy positions do not seem to change between the polyimide substrate (0 min) and the long Fe_2O_3/Cr_2O_3 deposition time substrate (120 min).

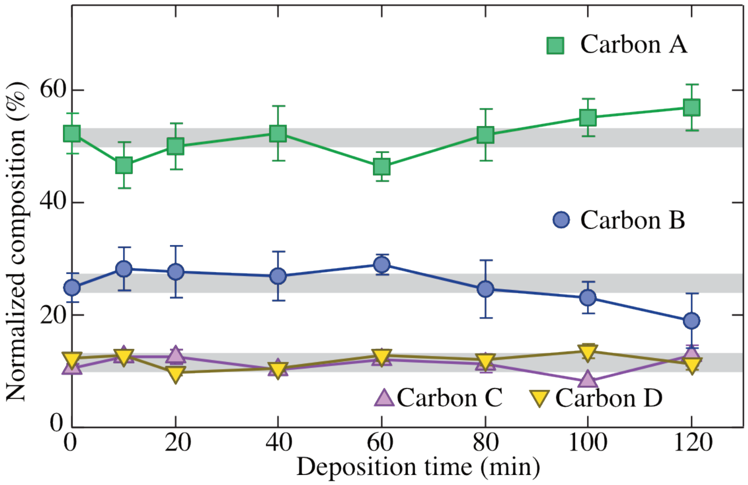

Figure 5.8: The composition changes of the four carbon groups as function of deposition time. The grey thick lines are the normalised compositions of polyimide nominal stoichiometry (see Fig. 5.4a). In group carbon A (C1-C2), there are 18 carbon atoms (51.4%). In group carbon B (C3-C6), there are 9 carbon atoms (25.7%). Group carbon C (C7) and D (C8) both have 4 carbon atoms (11.4%). No significant composition change was found in Carbon XPS analysis

peaks are too close to be separated by the peak fitting [28]. Therefore, eight carbon compound types were classified into four groups, Carbon A to D (see Table 5.5).

As shown in Fig. 5.7b, the line shapes of C 1s do not seem to be changed between the polyimide substrate (0 min) and the long Fe_2O_3/Cr_2O_3 deposition time substrate (120 min). Furthermore, we analyzed the composition change as a function of the deposition time for each carbon group. As shown in Fig. 5.8, there is no significant composition change in all groups. The generated electron current and deposited Fe_2O_3/Cr_2O_3 particles may not have enough energy to substantially alter the surface compositions of the carbon bonds.

5.4.3 Surface composition

The pretilt angle change can be associated with the surface material change from PI to Fe_2O_3/Cr_2O_3. Before Fe_2O_3/Cr_2O_3 deposition, the substrate was coated with polyimide which is widely used for planar LC alignment. As the deposition time increases, we expected that the substrate surface would be changed from polyimide to Fe_2O_3/Cr_2O_3 with more and more Fe_2O_3/Cr_2O_3 deposited. To study the cor-

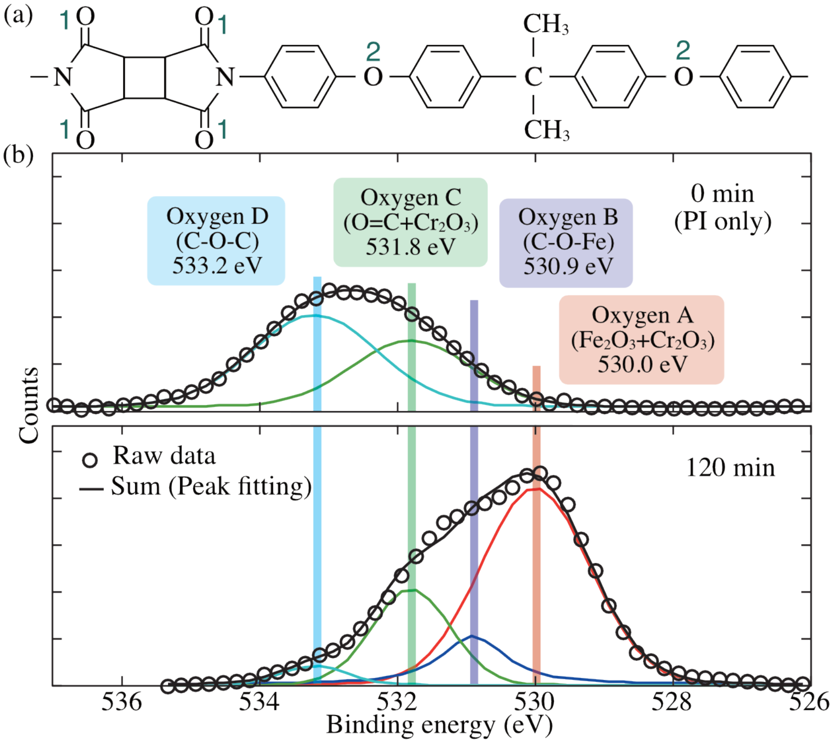

Figure 5.9: (a) Polyimide repeat unit and the binding states of the oxygen atoms. (b) Comparison of XPS spectra change of the O 1s peak before and after Fe_2O_3/Cr_2O_3 deposition process. The coloured lines are the peak positions of each oxygen group (see Table 5.6). The open circles are the experimental data and the black line is the summation of peaks of four oxygen groups. After the Fe_2O_3/Cr_2O_3 deposited (120 min), C-O-C peak almost disappeared and Fe_2O_3/Cr_2O_3 peak increased. It showed thatmore Fe_2O_3/Cr_2O_3 covered above the PI layer after the thin film deposition from stainless steel sputtering.

relation between the pretilt angle and the surface composition, we investigated the surface composition change by analyzing the O 1s signal which characterizes both the Fe_2O_3/Cr_2O_3 and polyimide.

The central position of the O 1s peak is around 531 eV. The fine binding energy peak position shifts with different neighboring atoms (see Table 5.6). The detected O 1s line is the superposition of the sub-peaks of the various oxygen compounds. By using the same analysis method of C 1s in Sec. 5.4.2, the compound types and amounts could be identified by using the peak-fitting method. Some of BE peaks cannot be distinguished due to resolution limit. We classified the six oxygen types into four groups, Oxygen A, B, C, and D in Table 5.6. The O 1s peak shape can be regarded as a superposition of four different peaks (see Fig. 5.9b and Table 5.6) with the binding energies collected from the literature [28, 30]. The Oxygen A peak can be associated with the Fe_2O_3/Cr_2O_3 signal because based on the discussion in Sec. 5.4.1, the signals of Fe_2O_3 (532.9 eV) and Cr_2O_3 (530.3 eV) were both from stainless steel sputtering. In contrast, the Oxygen D (C-O-C) peak can be associated with the polyimide (O2 in Fig. 5.9a).

The intensity evolutions of the O 1s peak related to Fe_2O_3/Cr_2O_3 (Oxygen A) and PI (Oxygen D) are plotted as a function of the deposition time in Fig. 5.10, showing that Fe_2O_3/Cr_2O_3 reached almost 100% after 40 minutes while the PI decreased in the same period, as expected. Comparing this composition evolution with the pretilt angle behavior as a function of the deposition time (see Fig. 4.4), we can see that the pretilt angle increases up to 80 minutes deposition time while the full Fe_2O_3/Cr_2O_3 coverage was reached in 40 minutes deposition time. This shows that the pretilt angle is not simply related to the Fe_2O_3/Cr_2O_3 coverage.

Group	BE^a (eV)	Compound^b	BE^c (eV)	Reference
Oxygen A	530.0	Fe_2O_3	529.8	[20]
			529.9	[21, 22]
			530.0	[23, 24]
		Cr_2O_3	530.1	[20, 21]
			530.2	[25]
			530.5	[26]
Oxygen B	530.9	C-O-Fe	530.9	[27]
Oxygen C	531.8	O=C (O1)	531.7	[28, 29]
			532.0	[30]
		Cr_2O_3	531.8	[25]
Oxygen D	533.2	C-O-C (O2)	533.0	[28, 29]
			533.3	[30]

Table 5.6: Binding energies of the O 1s group belonging to different chemical states. ^{a} Binding energy we used in this study. ^{b} To see O1 and O2, refer to the binding states of the oxygen atoms in Fig. 5.6. ^{c} Collected binding energies from literature.

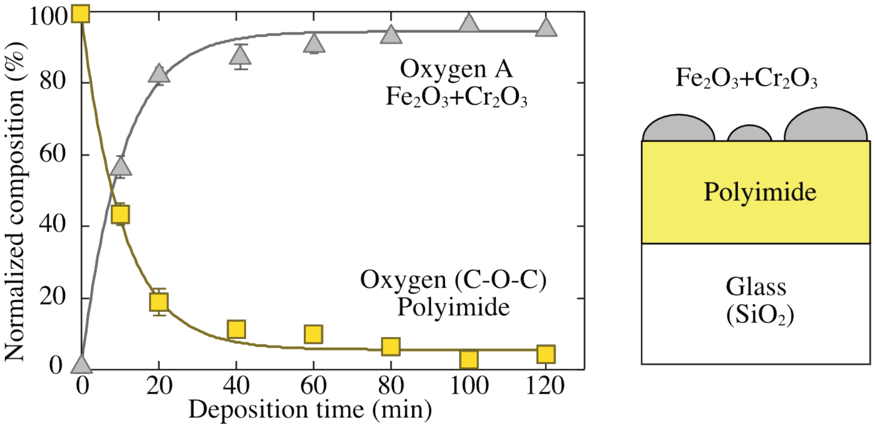

Figure 5.10: The normalised compositions of the Fe_2O_3/Cr_2O_3 (Oxygen A) and polyimide (Oxygen D) as the function of the deposition time. The lines are the exponential fitting results.

5.5 Conclusion

We have investigated the possible LC alignment mechanism by using two different physical and chemical surface characterization methods which are AFM and XPS. According to these studies, we come to the following findings:

- AFM images showed the deposited film is a roughed surface and a linear correlation was observed between the pretilt angle and the roughness squared.
- The wide-scan XPS spectra indicated that the main elements which are present on the surface for different deposition times were carbon (C), oxygen (O), nitrogen (N), iron (Fe), and chromium (Cr).
- After the comparison between the experimental Fe $2p_{3/2}$ and Cr $2p_{3/2}$ XPS peaks and the data from literature reports, the deposited thin film was identified as Fe_2O_3/Cr_2O_3 in a ratio of 75%/25%.
- No chemical bond change was found from the C 1s XPS study.
- The multi-peak fitting of the XPS O 1s peak which characterizes both the Fe_2O_3/Cr_2O_3 and polyimide showed that the Fe_2O_3/Cr_2O_3 coverage reached almost 100% after 40 minutes deposition time, while the pretilt angle increased until 80 minutes deposition time.

References

[1] Y. B. Kim, H. Olin, S. Y. Park, J. W. Choi, L. Komitov, M. Matuszczyk, and S. T. Lagerwall, Applied Physics Letters **66**, 2218 (1995).

[2] A. Rastegar, M. Škarabot, B. Blij, and T. Rasing, Journal of Applied Physics **89**, 960 (2001).

[3] D. W. Berreman, Physical Review Letters **28**, 1683 (1972).

[4] D. C. Flanders, D. C. Shaver, and H. I. Smith, Applied Physics Letters **32**, 597 (1978).

[5] M. Nakamura and M. Ura, Journal of Applied Physics **52**, 210 (1981).

[6] J. Stöhr, M. G. Samant, J. Lüning, A. C. Callegari, P. Chaudhari, J. P. Doyle, J. A. Lacey, S. A. Lien, S. Purushothaman, and J. L. Speidell, Science **292**, 2299 (2001).

[7] P. Chaudhari, J. Lacey, J. Doyle, E. Galligan, S. Lien, J. Lacey, J. Doyle, E. Galligan, S.-C. A. Lien, A. Callegari, G. Hougham, N. D. Lang, P. S. Andry, R. John, K.-H. Yang, M. Lu, C. Cai, J. Speidell, S. Purushothaman, J. Ritsko, M. Samant, J. S. hr, Y. Nakagawa, Y. Katoh, Y. Saitoh, K. Sakai, H. Satoh, S. Odahara, H. Nakano, J. Nakagaki, and Y. Shiota, Nature **411**, 56 (2001).

[8] F. J. Kahn, Applied Physics Letters **22**, 386 (1973).

[9] Y.-J. Lee, J. S. Gwag, Y.-K. Kim, S. I. Jo, S.-G. Kang, Y. R. Park, and J.-H. Kim, Applied Physics Letters **94**, 041113 (2009).

[10] J.-H. Son and W.-C. Zin, Applied Physics Letters **97**, 243306 (2010).

[11] K. Takatoh, M. Hasegawa, M. Koden, N. Itoh, R. Hasegawa, and M. Sakamoto, *Alignment Technology and Applications of Liquid Crystal Devices* (CRC Press, 2005).

[12] C. D. Wagner, L. E. Davis, M. V. Zeller, J. A. Taylor, R. H. Raymond, and L. H. Gale, Surface and Interface Analysis **3**, 211 (1981).

[13] T. Rasing and I. Musevic, *Surfaces and Interfaces of Liquid Crystals* (Springer Science & Business Media, 2013).

[14] P. G. de Gennes and J. Prost, *The Physics of Liquid Crystals* (Oxford University Press, 1993).

[15] A. J. Pidduck, G. B. Brown, S. Haslam, R. Bannister, I. Kitely, T. J. McMaster, and L. Boogaard, Journal of Vacuum Science & Technology A **14**, 1723 (1996).

[16] L. A. Goodman, J. T. McGinn, C. H. Anderson, and F. DiGeronimo, Electron Devices, IEEE Transactions on **24**, 795 (1977).

[17] J.-Y. Hwang, Y.-M. Jo, D.-S. Seo, S. J. Rho, D. K. Lee, and H. K. Baik, Japanese Journal of Applied Physics **41**, L654 (2002).

[18] H.-Y. Wu, C.-C. Wang, R.-P. Pan, T.-T. Tang, S.-J. Chang, and J.-C. Hwang, Molecular Crystals and Liquid Crystals **475**, 45 (2007).

[19] H.-Y. Wu and R.-P. Pan, Applied Physics Letters **91**, 074102 (2007).

[20] E. Paparazzo, Journalof Electron Spectroscopy and Related Phenomena **43**, 97 (1987).

[21] M. C. Biesinger, B. P. Payne, A. P. Grosvenor, L. W. M. Lau, A. R. Gerson, and R. S. C. Smart, Applied Surface Science **257**, 2717 (2011).

[22] N. S. McIntyre and D. G. Zetaruk, Analytical Chemistry **49**, 1521 (1977).

[23] C. R. Brundle, T. J. Chuang, and K. Wandelt, Surface Science **68**, 459 (1977).

[24] A. P. Grosvenor, B. A. Kobe, M. C. Biesinger, and N. S. McIntyre, Surface and Interface Analysis **36**, 1564 (2004).

[25] A. M. Salvi, J. E. Castle, J. F. Watts, and E. Desimoni, Applied Surface Science **90**, 333 (1995).

[26] G. C. Allen, M. T. Curtis, A. J. Hooper, and P. M. Tucker, Journal of the Chemical Society, Dalton Transactions , 1675 (1973).

[27] C. Fu, G. Zhao, H. Zhang, and S. Li, Internaltional Journal of Electrochemical Science (2014).

[28] D. Wolany, T. Fladung, L. Duda, J. W. Lee, T. Gantenfort, L. Wiedmann, and A. Benninghoven, Surface and Interface Analysis **27**, 609 (1999).

[29] G. Beamson and D. Briggs, *High Resolution XPS of Organic Polymers*, The Scienta ESCA300 Database (Wiley, 1992).

[30] A. M. Ektessabi and S. Hakamata, Thin Solid Films **377-378**, 621 (2000).

[31] U. Gelius, P. F. Heden, J. Hedman, B. J. Lindberg, R. Manne, R. Nordberg, C. Nordling, and K. Siegbahn, Physica Scripta **2**, 70 (1970).

[32] D. Briggs and G. Beamson, Analytical Chemistry **64**, 1729 (1992).

[33] A. Lebugle, U. Axelsson, R. Nyholm, and N. Mårtensson, Physica Scripta **23**, 825 (1981).

[34] M. Descostes, F. Mercier, N. Thromat, C. Beaucaire, and M. Gautier-Soyer, Applied Surface Science **165**, 288 (2000).

[35] M. Aronniemi, J. Sainio, and J. Lahtinen, Surface Science **578**, 108 (2005).

[36] T. Carlson, *Photoelectron and Auger Spectroscopy* (Springer Science & Business Media, Boston, MA, 2013).

[37] Y. Gao and S. A. Chambers, Journal of Crystal Growth **174**, 446 (1997).

[38] B. Stypula and J. Stoch, Corrosion Science **36**, 2159 (1994).

CHAPTER 6

Pretilt Angle Dependence of Electro-Optical LC Properties

6.1 Introduction

Liquid crystals (LCs) are widely used for display applications because their electro-optical properties can be easily controlled by an external electric field [1]. In liquid crystal displays (LCDs), several specifications, such as contrast ratio, response time and viewing angle, are very important [2–4]. To achieve better static and dynamic performances, several typical LCD modes, such as twist nematic (TN), vertical alignment (VA), and in-plane switching (IPS) modes, were developed and designed with different electrode patterns and LC alignment types [5–7]. As described in the introductions of the advantages and disadvantages for each LCD mode in Sec. 2.3, no single type of LCD is perfect for everything. Many studies have reported methods to improve the LCD performances by designing different cell structures and electrode patterns [8–10].

The response time is an important feature which describes the speed of the LC rotation [11]. If the response time for going from the bright state to the dark state is not fast enough, after the screen refreshes, the screen still shows or mixes with the previous displayed image, which is called the ghost image effect [12]. For both IPS and VA modes (see the operating principles introduced in Sec. 2.3.2 and 2.3.3), the response time for going from the bright state to the dark state depends on the time it takes for the LC molecules to relax back to the initial state after switching off the driving voltage. This response speed is limited by the nature of the LC relaxation to the initial orientation. In contrast to IPS and VA modes, in our parallel alignment (PA) cell (see Sec. 2.2.2), the response time to go from the bright state to the dark state can be faster by just applying a higher driving voltage.

Moreover, F S Yeung et al. and X Nie et al. reported the dependence of the static and dynamic LC properties on the pretilt angle [13, 14]. The pretilt angle is the angle between the substrate and the LC long axis in the surface layer. Therefore, we are interested in how to improve the LC cell performances by preparing a cell with an optimum pretilt angle. Based on the experimental findings, we want to find an LC cell with better performances: a higher contrast ratio and a faster response time.[1]

We also aim to develop two specific LCD applications. For a reflective black and white LCD watch, a low energy consumption and a low driving voltage can save the battery life [15]. Therefore, we design an LC cell with a lower driving voltage and maintaining the same response time and contrast ratio. The other specific LCD application is a welding goggle. An auto shade LCD goggle is used to protect eyes from the strong ultraviolet light that accompanies with a welding procedure. By detecting the light from the welding, an auto shade LCD goggle should switch very fast from the transparent state to the blocked state. The key point of this type LCD is how dark and how fast can be switched to the blocked state. We found that by preparing a cell with an optimum pretilt angle, a low transmittance at the blocking

---

[1] The viewing angle dependence is investigated in Ch. 8 by preparing a multi-domain LC cell.

state and a fast switching time can be achieved for applying the same driving voltage.

In this chapter, we used the previously presented pretilt angle control (see Ch. 4) to investigate the dependence of the static and dynamic LC properties on the pretilt angle. In studies of static LC properties, the contrast ratio and the threshold voltage was measured and discussed, in Sec. 6.3.1 and 6.3.2, respectively. In studies of the dynamic LC properties in Sec. 6.4, we discovered how to achieve a faster response time by designing a cell with an optimum pretilt angle. According to the experimental results, we found an optimum pretilt angle for a better performance LCD. In addition, for the specific applications, a low driving voltage LCD and an extremely fast blocking speed were demonstrated in Sec. 6.5.1 and 6.5.2, respectively, for cells with suitable pretilt angles.

6.2 Sample and experimental details

Samples were prepared following the pretilt angle control method described in Sec. 3.2. In this Ch. 6, the sputtering voltage and ion beam current were fixed at 560 V and 5 mA, respectively. Several samples were prepared under various Fe_2O_3/Cr_2O_3 deposition times to obtain corresponding LC pretilt angle substrates. Two Fe_2O_3/Cr_2O_3-deposited substrates were combined as an anti-parallel alignment cell and sandwiched with Mylar thin film or glass ball spacers. All of the empty cells were filled with 4'-n-pentyl-4-cyanobiphenyl (5CB, Merck) at 60°C and annealed to room temperature. All the static and dynamic LC properties were studied by using the electro-optical measurement setup introduced in Sec. 3.3.3.

Fig. 6.1a shows a parallel alignment (PA) mode LCD, sandwiched between a pair of crossed polarizers. In the bright state, the LC molecules align parallel or tilted to the substrate with a pretilt angle $\theta_p < 45°$. By applying a vertical external electric field and using a positive dielectric anisotropy LC, the LC director reorients to close to 90° to reach the dark state. Therefore, the bright and dark states are switched by applying 0 V and a high enough driving voltage, respectively. The relation between the transmittance, the phase retardation, and the LC director was detailedly introduced in Sec. 2.2.2. For cells with different cell thicknesses, the transmittance of the dark state does not change because no phase retardation can be generated while the LC molecules are perpendicular to the polarizers. However, in the bright state, the transmittance changes for different cell thickness because of the thickness-dependent phase retardation. Figure 6.1b shows the transmittance of the bright state as a function of the cell thickness for a cell with 0° pretilt angle. For zero cell thickness, no phase retardation can be generated ($\Delta\phi = 0$) which means that the transmittance is dark ($T = 0$). With increasing cell thickness, the transmittance will increase to the maximum ($T = 1$) while the phase retardation goes to $\Delta\phi = \pi$. However, with further increasing cell thickness, the transmittance will decrease to $T = 0$ while the phase retardation goes from $\Delta\phi = \pi$ to $\Delta\phi = 2\pi$. To design a 0° pretilt angle cell

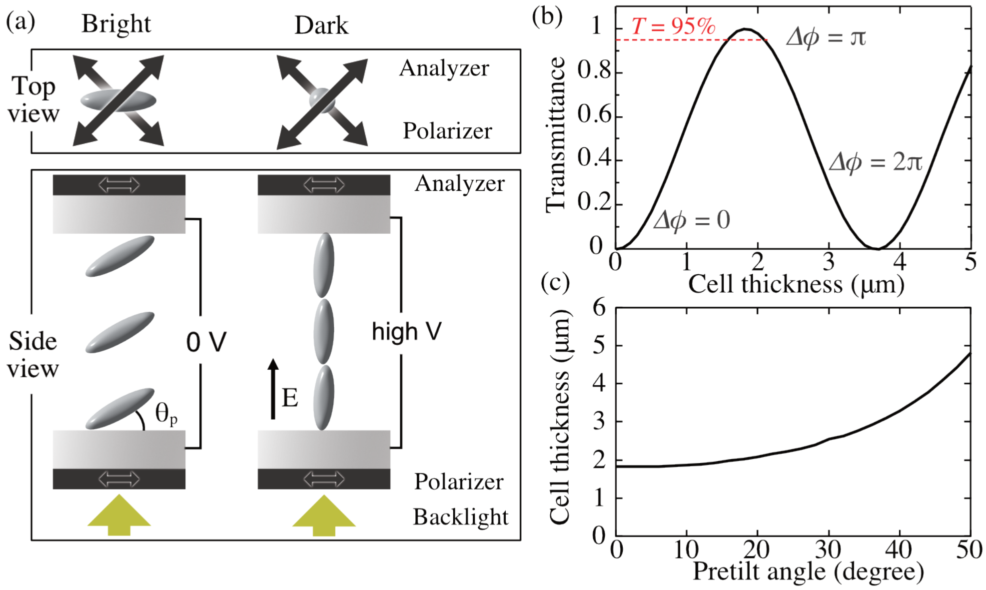

Figure 6.1: (a) Schematic representation of the bright and the dark states for a PA mode. (b) The transmittance as a function of the cell thickness for a 5CB cell with a 0° pretilt angle. (c) The cell thickness to reach a phase retardation $\Delta\phi = \pi$ in the bright state as a function of the pretilt angle.

with the bright state at $\Delta\phi = \pi$, the cell thickness has to be controlled at 1.83 ± 0.26 µm for reaching at least 95% transmittance of the bright state (red dashed line in Fig. 6.1b). Moreover, for cells with different pretilt angles to have a bright state at $\Delta\phi = \pi$, the corresponding cell thickness was calculated by Eq. 2.2 and shown in Fig. 6.1c.

In general, for a cell which is sandwiched with commercial spacers, the cell thickness can be controlled by choosing a specific spacer thickness; for instance 4, 6, and 12 µm. However, in our case, thicknesses of LC cells with different pretilt angles had to be controlled more precisely. For instance, cells with 10° and 30° pretilt angles had to be prepared with 1.87 and 2.57 µm cell thicknesses for reaching the π phase retardation in the bright state. To overcome the problem of the finite thickness control, as shown in Fig. 6.2a, a wedge cell was prepared by sandwiching a d_m thick spacer on one side and no spacer on the other side of the cell. As the experimental setup shown in Sec. 3.3.3, the transmittance of a cell was measured by using a He-Ne laser, being a backlight in an LCD. Therefore, in a wedge cell, the specific cell thickness d_l can be found by just shifting the laser measured position (y-axis in Fig. 6.1a). To measure the LC properties in a uniform thickness area, the laser beam was focused

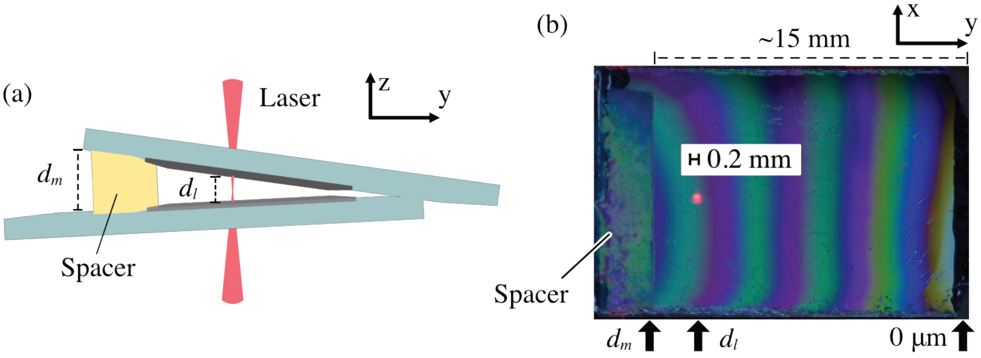

Figure 6.2: Cell structure and measured size. (a) Schematic diagram of the wedge cell and focused laser beam. d_m indicates the thickness of the mylar spacer, which d_l indicates the cell thickness at the laser spot. (b) Dimensions of the cell and the beam size.

to a small spot size ~ 0.2 mm (the red spot in Fig. 6.2b). For a cell with 4 µm spacer on one side, the accuracy of the cell thickness is ± 0.03 µm in the laser spot region. Moreover, for a wedge cell and a standard parallel cell under the same cell preparation condition, their pretilt angles and voltage-dependent phase retardation curves were measured The LC alignment effects for both types cells were identical.

6.3 Static studies

First, the studies are focused on the dependence of the static LC properties on the pretilt angle with two subjects, the contrast ratio and the threshold voltage, by measuring and analyzing the voltage-dependent transmittance. Fig. 6.3a presents the transmittance as a function of the driving voltage for cells with different pretilt angles. All cells were designed to have the correct cell thickness (Fig. 6.1c) to reach the phase retardation of π in the bright state. The transmittance decreases with increasing driving voltage from the maximum $T = 1$ to the minimum $T = 0$. The experimental results roughly demonstrate that the bright and dark states of LC cells with different pretilt angles all can be switched between 0 V and 15 V, respectively.[2]

6.3.1 Contrast ratio

The contrast ratio is an important LCD property defined as the ratio of the transmittance of the bright state relative to that of the dark state. An LCD with a good and

---

[2] Because the performances of our cell have to be compared with the other LCD modes, we choose a 15 V driving voltage which is in the voltage range commonly used in a large size LCD (10 ~ 20 V) [8].

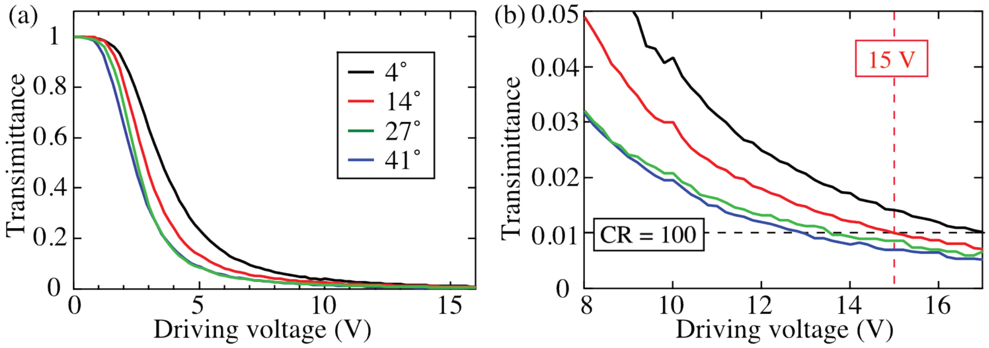

Figure 6.3: (a) The transmittance as a function of the driving voltage for the cells with different pretilt angles. (b) The transmittance of the dark state in the high driving voltage region.

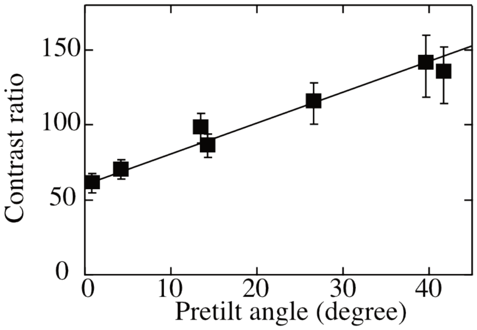

Figure 6.4: The contrast ratio of the cells with different pretilt angles. Here the driving voltage is applied between 0 V and 15 V for the bright and the dark states, respectively.

proper contrast ratio can present more image details, especially in the brightest and the darkest regions. In this thesis, the contrast ratio CR is defined in the following way:

$$CR = \frac{T_{bright}}{T_{dark}} = \frac{T(0\text{ V})}{T\,(V_d)} \tag{6.1}$$

where T_{bright} is the transmittance of the bright state which is the initial state with no driving voltage (0 V). T_{dark} is the transmittance of the dark state while a high driving voltage V_d is applied.

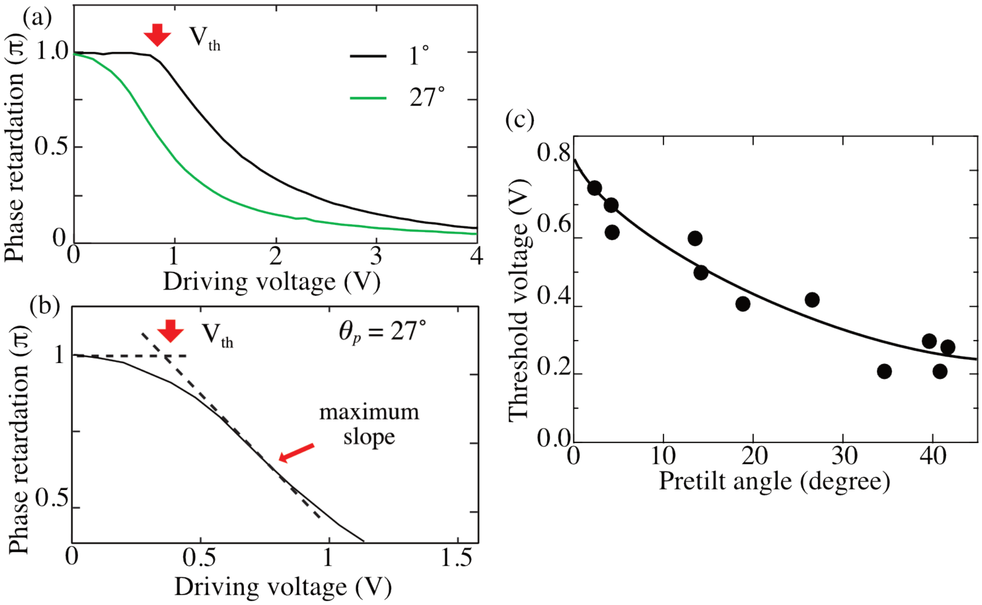

Figure 6.5: The phase retardation change as a function of the driving voltage for the cells with (a) low (1°) and high (22°) pretilt angles. (b) Zoomed figure of (a) in the low driving voltage region and the definition of the threshold voltage for a cell with a high pretilt angle. (c) The threshold voltage as a function of the pretilt angle.

6.3.2 Threshold voltage

For a cell with a pretilt angle of 1° in Fig. 6.2a, the phase retardation does not change before a certain threshold voltage is reached.[3] In other words, the threshold voltage is the minimum voltage to start to rotate the LC molecules. This threshold voltage can be derived from the Freedericksz transition threshold voltage V_{th} [16]

$$V_{th} = \pi\sqrt{\frac{K_1}{\epsilon_0 \Delta\epsilon}} \tag{6.2}$$

where K_1 is the splay elastic constant and the $\Delta\epsilon$ is the dielectric anisotropy of the LC. According to this equation, in our case for 5CB with $K_1 = 6.1 \times 10^{-12}$ N [17]

---

[3] The threshold voltage is determined by analyzing the phase retardation curve, instead of the transmittance curve. For instance, in order to measure the pretilt angle precisely in Ch. 4, a cell was prepared with a thicker cell thickness of 23 µm. In this cell, the phase retardation goes from 0 to $\sim 12\pi$ while a driving voltage switches from a high enough voltage to 0 V. Meanwhile, the transmittance curve decreases and increases while the phase retardation goes through odd and even π. Therefore, analyzing a voltage-dependent phase retardation is a better method to find the threshold voltage.

and $\Delta\epsilon = 10$ [18], the threshold voltage is calculated as 0.83 V, which is in agreement with the data in Fig. 6.2a.

In a planar cell, the threshold voltage can be clearly defined as the turning point where the phase retardation abruptly changes. However, in Fig. 6.5a, for a cell with high pretilt angle (green line), a flat area and a clear turning point in the phase retardation could not be found. F S Yeung et al. reported a similar finding that the LC threshold voltage no longer exists for a cell with a nonzero pretilt angle [13]. Moreover, they defined and measured the threshold voltage of a cell with a high pretilt angle by observing the transmittance change while a driving voltage is applied. Before the threshold voltage, it takes a few minutes for the change of the transmittance. By applying a driving voltage which is slightly higher than the threshold voltage, the transmittance changed in a few seconds or less. However, this threshold voltage measurement method and definition are improper because the experimental result can be influenced by the increasing step of the driving voltage and the waiting time to determine the change of the transmittance.

Fig. 6.5b is a zoomed figure of Fig. 6.5a in a low driving voltage region. The phase retardation decreases smoothly at the onset of increasing driving voltage (< 0.5 V); and then the phase retardation decreases rapidly. When the driving voltage is higher, the slope of the phase retardation decreases again (see the high driving voltage region in Fig. 6.5a). This threshold-like behavior in the voltage-dependent phase retardation still appears. Therefore, as shown in Fig. 6.5b, we defined the threshold voltage as the cross point from the line of the maximum slope of the curve to the level of the initial phase retardation $\Delta\phi = \pi$.

The threshold voltages for cells with different pretilt angles are plotted in Fig. 6.5c, showing that the threshold voltage decreases with increasing pretilt angle. The threshold voltage is an important parameter which influences the LC static and dynamic properties [13, 19]. A lower threshold voltage means that a lower driving voltage is needed to start to rotate the LC molecules. It is the reason why, under the same driving voltage of 15 V, a lower transmittance was found in a cell with a higher pretilt angle (see the red vertical dashed line in Fig. 6.3b).

6.4 Dynamic Studies

Motion blur is a well-known problem for LCDs which is due to the fact that the optical response does not change rapidly enough when the image changes to the next frame. The response time is a standard specification to indicate how quickly the image can be changed on LCDs. Two of the important dynamic parameters, turn on time t_{on} and turn off time t_{off}, were investigated. The turn off and turn on times are defined as the optical response time for the change of the transmittance from 10% to 90% and 90% to 10%, respectively.

In a PA cell, the bright and dark states are operated between 0 V and V_d driving

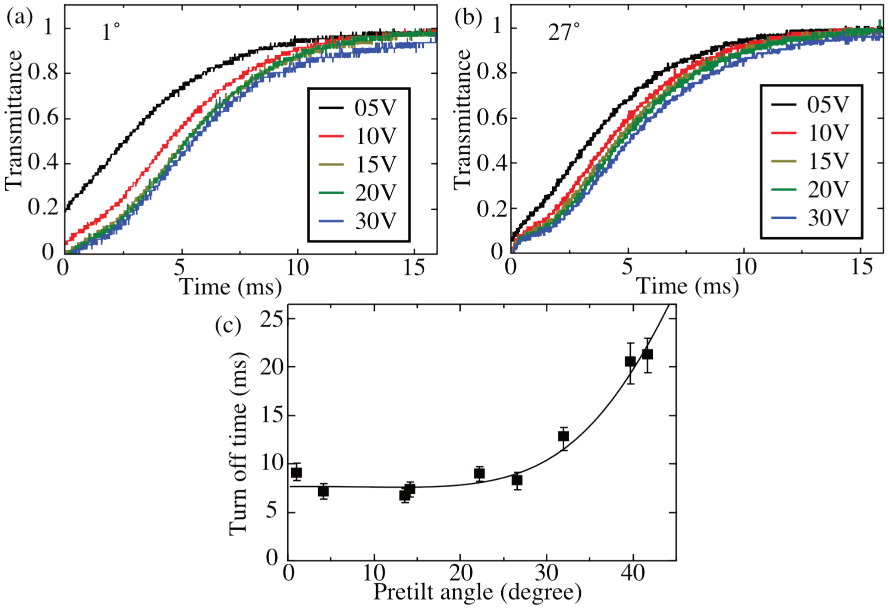

Figure 6.6: Turn off time. The time dependent transmittance for different driving voltages for the cells with (a) 1° and (b) 27° pretilt angle. The driving voltage was turned off from 15 V to 0 V at time $t = 0$. (c) The dependence of the turn off time on the pretilt angle.

voltage, respectively. When the driving voltage is "switched off" from V_d to 0 V, the LCD "switches on" from a dark state to a bright state (see Fig. 6.6a and b). On the other hand, when the driving voltage is "switched on" from 0 V to V_d, the LCD "switches off" from a bright state to a dark state (see Fig. 6.7a and b). Note that, in this thesis, the turn on and turn off times are measured from the real-time optical response; but the words, turn on and turn off, are related to describe the behavior of the driving voltage switching, instead of the optical switching.

6.4.1 Turn off time

As shown in Fig. 6.6a and b, the driving voltage was switched off from different V_d to 0 V at $t = 0$ of cells with 1° and 27° pretilt angles, respectively. First of all, for the cell with a 1° pretilt angle, the transmittance did not increase from $T = 0$ for a 5 V driving voltage (see the black curve in Fig, 6.6a) because the initial driving voltage is not high enough to keep the director of the LC molecules close to 90°. For the cell with 27° pretilt angle (see Fig. 6.6b), the transmittance of the initial dark state was closer to $T = 0$ than for the cell with a 1° pretilt angle. For a cell with a higher pretilt angle, a lower threshold voltage allows the LC molecules to rotate closer to 90° which results in a lower transmittance.

The turn off time was measured by switching off the driving voltage from 15 V to 0 V and plotted in Fig. 6.6c. For a cell with a pretilt angle less than 30°, no dependence of the turn off time on the pretilt angle was found. For a cell with a pretilt angle larger than 30°, the turn off time increased with pretilt angle increasing. This pretilt angle effect of the turn off time will be theoretically discussed in Sec. 7.5.

In the static LC studies of Sec. 6.3.1, we found that a cell with a higher pretilt angle ($\theta_p > 20°$) had a better contrast ratio (see Fig. 6.4) than a cell with a lower pretilt angle ($\theta_p > 5°$). To get a better contrast ratio and keep a similar turn off time, the LCD should be designed with a ∼25° pretilt angle. As the experimental result of Fig. 6.6c shown, the turn off times of cells with 1° and 27° pretilt angles were very close being, 9.1 ms and 8.4 ms, respectively.

6.4.2 Turn on time

As shown in Fig 6.7a and b, the driving voltage was switched on from 0 V to different V_d of cells with 1° and 27° pretilt angles, respectively. As the discussion of the turn off time in previous Sec. 6.4.1, for the cell with a 1° pretilt angle, the transmittance did not decrease to $T = 0$ with a 5 V driving voltage (see the black curve in Fig, 6.7a) because the driving voltage is not high enough to rotate the LC molecules close to 90°. For the cell with a 27° pretilt angle in Fig. 6.7b, the transmittance of the dark state was closer to $T = 0$ than the cell with a 1° pretilt angle because of the lower threshold voltage.

The turn on time was measured by switching on the driving voltage form 0 V to 15 V and plotted in Fig. 6.7c. The turn on time decreases for decreasing pretilt angle until ∼25°; and then it increases for a cell with a higher pretilt angle larger than ∼25°. This pretilt angle effect of the turn on time will be theoretically discussed in Sec. 7.5. In the previous section 6.4.1, we mentioned that a cell with a ∼ 25° pretilt angle has good performances; in Fig. 6.7, a cell with a ∼ 25° pretilt angle also has the fastest turn on time. The turn on time for a cell with a 27° pretilt angle ($t_{on} = 0.15$ ms) is three times faster than the turn on time for a cell with a 1° pretilt angle ($t_{on} = 0.47$ ms).

In summary, a cell with ∼ 25° pretilt angle is the best choice for a general LCD application. We listed a table to compare the static and dynamic LCD properties for cells with 1° and 27° pretilt angles (see Table 6.1). To obtain a higher contrast ratio larger than 500, a higher driving voltage of 25 V is applied to a cell with a 27° pretilt angle. According to the experimental results of static and dynamic LCD properties, a better performances LCD can be achieved by designing an LC cell with a higher pretilt angle (θ_p ∼25°).

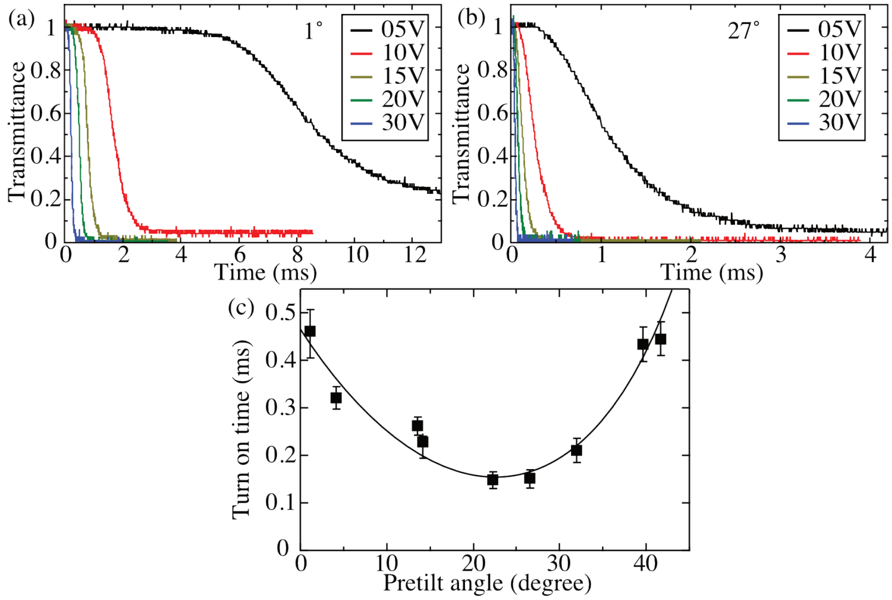

Figure 6.7: Turn on time. The time dependent transmittance for different driving voltages for the cells with (a) 1° and (b) 27° pretilt angle. The driving voltage was switched on to 15 V at time $t = 0$ s. (c) The dependence of the turn on time on the pretilt angle.

LCD property	1°	27°	27°
	(0V/15V)		(0V/25 V)
Contrast ratio	63:1	116:1	535:1
t_{off} (ms)	9.1	8.4	9.3
t_{on} (ms)	0.47	0.15	0.05

Table 6.1: Comparison of the static and dynamic LCD properties for cells with 1° and 27° pretilt angles. Here the general bright and dark state of LCDs were operated between 0 V and 15 V, respectively. For a higher contrast ratio (>500), the bright and dark state of LCDs were operated between 0 V and 25 V, respectively.

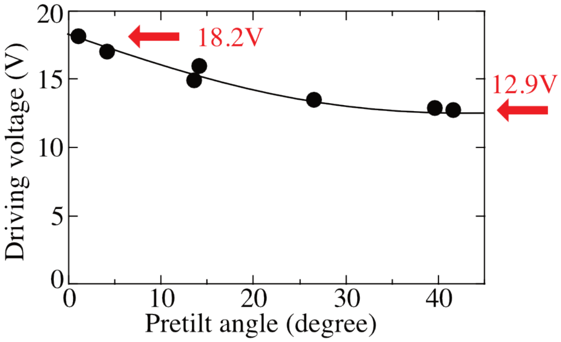

Figure 6.8: The driving voltage of the dark state to achieve a contrast ratio of 100 for the cells with different pretilt angles.

6.5 Specific LCD applications

6.5.1 Low driving voltage

To achieve an energy saving LCD, it is a fundamental requirement to keep driving voltages as low as possible and maintain all the other performances [15]. In Sec. 6.3.1, the experimental results showed that a cell with a higher pretilt angle has a higher contrast ratio by applying 0 V and 15 V driving voltages to reach bright and dark states, respectively. On the other hand, lower driving voltages may be required to reach the same contrast ratio for a cell with a higher pretilt angle.

To find the driving voltage dependence on the pretilt angle, we set the bright and dark states operating at 0 V and V_d driving voltages, respectively, to just reach a standard contrast ratio $CR = 100$ of a typical IPS mode. The transmittance of the bright state is set as $T = 1$; so, to reach $CR = 100$, the transmittance of the dark state is $T = 0.01$ (see the black dashed line in Fig. 6.3b). The driving voltages to the dark state with different pretilt angles are plotted in Fig. 6.8. The experimental results showed that the driving voltage of the cell with a high pretilt angle (12.9 V) is two times lower than a cell with a low pretilt angle (18.2 V). In the turn on and turn off times studies (Sec. 6.4), we found that a cell with a very high pretilt angle ($< 30°$) has slow turn on and turn off times (see Fig. 6.6c and 6.7c). Therefore a cell with 27° pretilt angle was chosen to compare the driving voltage and the dynamic performances with a 1° pretilt angle cell. The LCD properties between these two cells are listed in Table 6.2. First, the driving voltage to reach a standard contrast ratio $CR = 100$ of the 27° pretilt angle cell (13.5 V) is lower than of the 1° pretilt angle cell (18.2 V). The turn off times of the cells with 1° and 27° pretilt angles were measured by switching off the driving voltage from 18.2 V and 13.5 V, respectively. The turn on times of the cells with 1° and 27° pretilt angles were measured by switching on the

Low driving voltage LCD Property	1°	27°
Driving voltage (V)	18.2	13.5
t_{off} (ms)	9.2	8.3
t_{on} (ms)	0.30	0.18

Table 6.2: Comparison of LCD static and dynamic properties for cells with 1° and 27° pretilt angles. Here the bright and dark state of LCDs were operated between 0 V and 15 V, respectively.

driving voltage from 0 V to 18.2 V and 13.5 V, respectively. As the measured LCD properties shown in Table 6.2, to design a low driving voltage LCD, the LCD should be designed with a 27° pretilt angle which still has the similar turn off and turn on times as a cell with 1° pretilt angle

6.5.2 Faster response time

An important application for an LCD with a fast response time is in the area of eye protection during welding [20]. For this purpose, auto shade goggles have been developed to improve the shortcoming of traditional fixed UV filter plates that are too dark to see the environment when the welding apparatus is off. By detecting the light strength from the welding, an auto shade goggle switches automatically from a transparent (bright) state to a blocked (dark) state by working as an LCD to block its backlight. Two key points of this goggle are a suitable shade number (transmittance of the blocking state) and a fast switching time at the onset of a welding process. For instance, a commercial auto shade goggle (Grand GDS, Balder) has a switch-on time of 0.15 ms [21].

In the contrast ratio study of Sec. 6.3.1, by switching on the driving voltage to 25 V, a cell with a high (27°) pretilt angle has a low transmittance of a dark state (0.18%). By following the daily maximum permissible UV exposure of 3000 $\mu W/cm^2 \cdot s$, for a welding worker with this 99.91% blocking goggle[4], they can work 80 minutes per day with a 700 $\mu W/cm^2$ argon-shielded metal inert gas welding for 1 m far distance [22].

In the LC dynamic studies of Sec. 6.4.2, we found that a cell with a ~25° pretilt angle had a fast turn on time of 0.18ms which is comparable to the commercial value.

In general, the definition of a turn on time is defined as a time for a transmittance change from 90% to 10%. However, as shown in Fig. 6.9a, after the driving voltage is applied at $t = 0$, there is a time delay of the response of the transmittance from

---

[4] The first polarizer at least blocks 50% light intensity from an unpolarised light source, so the passed light intensity is 0.09%.

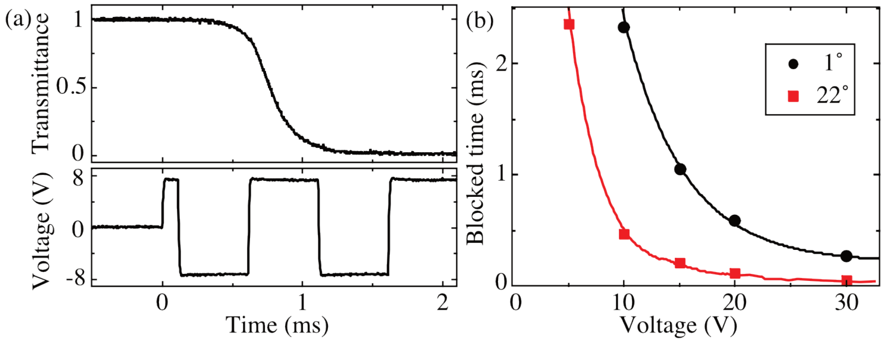

Figure 6.9: (a) The turn on transmittance (black line) and the driving voltage (red line). The driving voltage was switched on at time $t = 0$ s. (b) Turn on time of the transmittance change from 100% to 10% for the cells with 1° and 27° pretilt angle.

100% to 90%. The long time delay was found especially in a cell with a lower driving voltage and a lower pretilt angle (see Fig. 6.7a and b). This effect can not be ignored for a welding goggle, because the time delay appears at the highest light intensity region ($T = 90 \sim 100\%$) which can cause severe eye damage. Therefore, in this Sec. 6.5.2, we redefined the turn on time as a transmittance change from 100% to 10% and called it "blocking time."

As shown in Fig. 6.9b, the blocking time of a cell with a 27° pretilt angle is always at least five times faster than a cell with a 1° pretilt angle. Moreover, by giving a 30 V driving voltage, the strong light can be blocked very fast (60 µs).[5] Therefore, a high blocking (> 99.91%) and fast response (60 µs) welding google can be designed by preparing an LC cell with a ~25° pretilt angle and a 30 V switching voltage.

6.6 Conclusion

Using our new pretilt angle control, the dependence of the static and dynamic LC properties on the pretilt angle was investigated. According to the experimental results, to operate an LCD with the same driving voltage, we come to the following conclusions:

- A cell with a higher pretilt angle has a higher contrast ratio. This is because a lower threshold voltage was found in a cell with a higher pretilt angle.
- For a cell with a pretilt angle larger than 30°, the turn off time increases with increasing pretilt angle; for a cell with a pretilt angle less than 30°, no pretilt angle dependence of the turn off time is found.

---

[5] The limited voltage response of our voltage amplifier is ~10 µs.

- The turn on time decreases for a cell with a higher pretilt angle until ~25°; and then the turn on time increases for a cell with a higher pretilt angle larger than ~25°.

According to the above findings, a cell with a 27° pretilt angle has an optimal LCD performance as listed in Table 6.1.

If we design a low driving voltage LCD while keeping the same contrast ratio, a driving voltage of a cell with a higher pretilt angle ($\theta_p > 20°$) is lower than for a cell with a lower pretilt angle ($\theta_p \sim 0°$) with the same response time. Moreover, a cell with a high pretilt angle can be switched fast (~ 60 µs) from 100% to 10% transmittance for a welding goggle application.

References

[1] F. J. Kahn, Applied Physics Letters **20**, 199 (1972).

[2] K. Takatoh, M. Hasegawa, M. Koden, N. Itoh, R. Hasegawa, and M. Sakamoto, *Alignment Technology and Applications of Liquid Crystal Devices* (CRC Press, 2005).

[3] H.-S. Kwok, S. Naemura, and H. L. Ong, *Progress in Liquid Crystal Science and Technology*, In Honor of Shunsuke Kobayashi's 80th Birthday (World Scientific, 2013).

[4] G. Meier, E. Sackmann, and J. G. Grabmaier, *Applications of Liquid Crystals* (Springer Science & Business Media, 2012).

[5] M. Schadt and W. Helfrich, Applied Physics Letters **18**, 127 (1971).

[6] M. F. Schiekel and K. Fahrenschon, Applied Physics Letters **19**, 391 (1971).

[7] M. Oh-e and K. Kondo, Applied Physics Letters **67**, 3895 (1995).

[8] T.-L. Ting, C.-Y. Chen, S.-W. Tsao, M.-J. Lu, Y.-Y. Kung, W.-H. Hsu, and J.-J. Su, Journal of Display Technology **9**, 832 (2013).

[9] S. H. Lee, S. S. Bhattacharyya, H.-S. Jin, and K.-U. Jeong, Journal of Materials Chemistry **22**, 11893 (2012).

[10] S.-W. Kang, Y. E. Choi, B. H. Lee, J. H. Lee, S. Kundu, H.-S. Jin, Y. K. Yun, S. H. Lee, and L. Komitov, Liquid Crystals **41**, 552 (2013).

[11] D. H. Kim, Y. J. Lim, D. E. Kim, H. Ren, S. H. Ahn, and S. H. Lee, Journal of Information Display **15**, 99 (2014).

[12] C. C. Lin, C. Ye, H. L. Hou, C. Y. Lee, R. Xie, G. Chen, and F. Yang, SID Symposium Digest of Technical Papers **43**, 965 (2012).

[13] F. S. Yeung, Y. W. Li, and H.-S. Kwok, Applied Physics Letters **88**, 041108 (2006).

[14] X. Nie, H. Xianyu, R. Lu, T. X. Wu, and S.-T. Wu, Journal of Display Technology **3**, 280 (2007).

[15] A. Golemme, S. Zumer, J. W. Doane, and M. E. Neubert, Physical Review A **37**, 559 (1988).

[16] V. Fréedericksz and V. Zolina, Transactions of the Faraday Society **29**, 919 (1933).

[17] J. D. Bunning, T. E. Faber, and P. L. Sherrell, Journal de Physique **42**, 1175 (1981).

[18] B. R. Ratna and R. Shashidhar, Pramana **6**, 278 (1976).

[19] X. Nie, R. Lu, H. Xianyu, T. X. Wu, and S.-T. Wu, Journal of Applied Physics **101**, 103110 (2007).

[20] G. P. Brittain, British journal of ophthalmology **72**, 570 (1988).

[21] *Technical manual - GRAND GDS*, Balder Ltd. (2011).

[22] T. N. McManus and A. N. Haddad, International Journal of Open Scientific Research **1**, 15 (2013).

CHAPTER 7

Numerical Investigation of the LC Switching Dynamics

7.1 Introduction

In Ch. 6, we demonstrated that a high liquid crystal display (LCD) performance, such as a high contrast ratio and a fast response time, can be achieved by preparing a parallel alignment (PA) cell with a proper pretilt angle. To find the corresponding pretilt angle for the best LCD performance, the dependence of the performance on the pretilt angle was investigated by making and examining a series of test liquid crystal (LC) cells. Actually, a reliable theoretical analysis would be an easier method to predict the most suitable cell parameters for the best LCD performance.

Some literature reports also investigated the dependence of LCD performances on the pretilt angle via an experiment and a theoretical analysis [1, 2] However, so far, LCD performances can only be theoretically studied by computer simulations or by calculation methods using a small angle approximation [3–5]. Therefore, the experimental results can only accurately be confirmed by computer simulations; but the simulation results can not intuitively explain the LC properties.

In this chapter, a new improved calculation method will be presented which can predict the static and dynamic LC director distribution for a wide variety of PA cells. In Sec. 7.3, the correctness of our calculation method was confirmed by comparing the calculation results of the LC director distribution with simulation results. In Sec. 7.4, the calculated LC director distribution was transformed to a phase retardation to be compared with the experimental phase retardation. In Sec. 7.5, for the dynamic studies, the relaxation time of the LC director is presented first and then expressed in terms of the phase retardation. The same has been done for the rise time. All the calculations regarding the phenomena investigated in Ch. 6 show excellent agreements with the experiments.

7.2 From LC to LCD

In most LCDs, the brightness (transmittance) of the pixels is controlled via the LC electro-optical properties [6, 7]. LC molecules can be easily reorientated by the balance between a surface alignment and an external electric field [8, 9]. For two extreme cases of a PA cell with a 0° pretilt angle, all LC molecules align parallel or perpendicular to the substrate at 0 V and a high enough driving voltage, respectively (see Fig. 7.1a and c). As shown in Fig. 7.1b, under a pair of crossed polarizers oriented 45° with respect to the surface alignment direction, the LC cell presents bright and dark states at 0 V and a high enough driving voltage, with a phase retardation of $\Delta\phi = \pi$ and $\Delta\phi = 0$, respectively [10]. The optical response and the operating principle of the PA mode were explained in detail in Sec. 2.2.3.

The phase retardation $\Delta\phi$ can be derived from the integration of the birefringence effect over the whole LC layer and depends on the LC director distribution: $\Delta\phi = \int_d^0 \Delta n_{eff}(\theta)\ k\ dz$. In a PA cell, the transmittance depends on the phase retar-

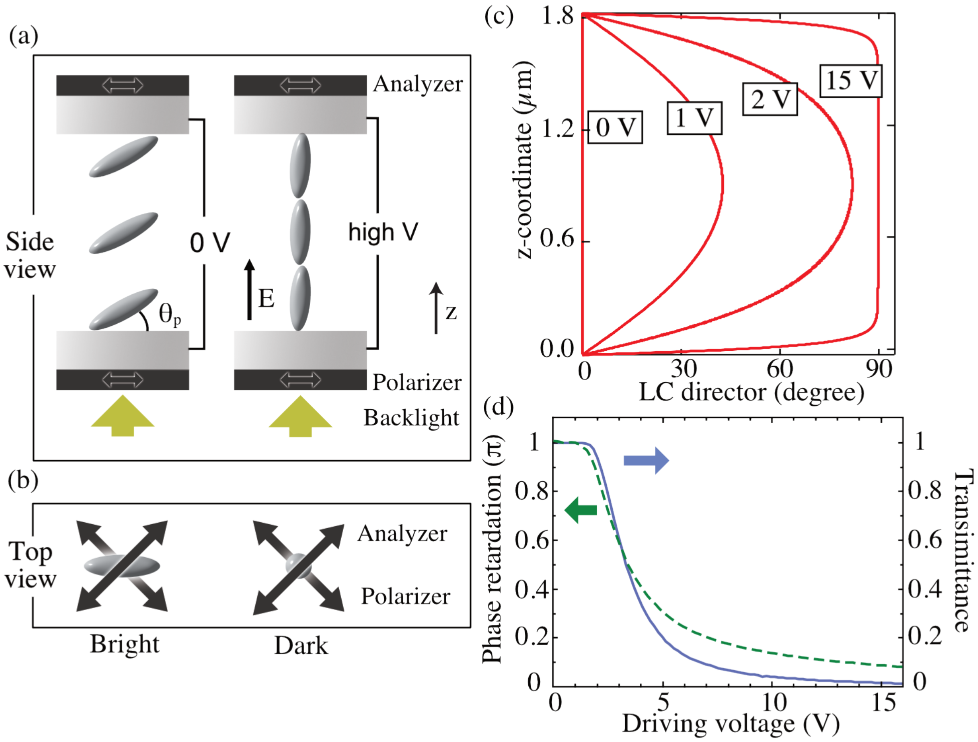

Figure 7.1: From LC to LCD. The schematic representation of a PA cell in (a) side view and (b) top view. (c) LC director distributions for different driving voltages. (d) Phase retardation (green dashed curve) and transmittance (blue curve) as a function of the driving voltage.

dation which follows from $T = sin^2(\Delta\phi/2)$. So the transmittance of a PA LCD can be controlled by changing the LC director distribution by applying different driving voltages (see Fig. 7.1c and d). Therefore, to calculate the transmittance of an LC cell, the first step of the theoretical study is to find out the relation between the LC director distribution and the cell conditions, such as the pretilt angle and the driving voltage.

For both the simulations and the calculations, the LC director distribution can be derived by finding the minimum of the LC distortion and electric free energies (see Sec. 2.2.3). Based on a PA cell structure of Fig. 7.1a, the LC director distribution $\theta(z)$ can be derived following the time-dependent Ericksen-Leslie's equation where back-flow and inertial effects are neglected:

$$\left(K_1 \sin^2\theta + K_3 \cos^2\theta\right)\frac{\partial^2\theta}{\partial z^2} + (K_3 - K_1)\sin\theta\cos\theta\left(\frac{\partial\theta}{\partial z}\right)^2 + \epsilon_0\Delta\epsilon \mathrm{E}^2 \sin\theta\cos\theta = \gamma\frac{\partial\theta}{\partial t} \tag{7.1}$$

where K_1 and K_3 are the splay and bend distortion constants, respectively, $\Delta\epsilon$ is the LC dielectric anisotropy, E is the external electric field which is perpendicular to the substrate, and γ is the rotational viscosity. The LC director $\theta(z)$, also called LC tilt angle, is defined as the angle between the LC long axis at position z and the substrate plate (see **z**-axis in Fig. 7.1a).

7.3 Static studies - LC director distribution

Now we will demonstrate how to obtain the LC director distribution by solving the above partial differential equation via a computer simulation, an existing calculation method with a small angle approximation and our new calculation method.

7.3.1 Simulation

A simulation is a good and reliable method to investigate LC properties with adjustable cell conditions, by numerically solving the free energy equation. Here we used a finite element method (FEM) package software named Multiphysics (COMSOL Multiphysics) to numerically solve the Ericksen-Leslie's equation (Eq. 7.1). The values of the 5CB LC constants are listed in Table 7.1 at the end of this chapter.

In a PA cell, the boundary condition was restricted to the pretilt angle $\theta(z) = \theta_p$ at $z = 0$ and at $z = d$, under a strong anchoring strength assumption. Here d is the thickness of the LC layer, also called the cell gap. To design a PA cell operating between dark state at $\Delta\phi = 0$ and bright state at $\Delta\phi = \pi$, the LC thickness has to be controlled well for reaching $\Delta\phi = \pi$ in the initial state without any driving voltage. Therefore, different LC thicknesses d were used for cells with different pretilt angles θ_p (see Fig. 6.1c).

As the curves shown in Fig. 7.2a and b, by applying a driving voltage, the LC molecules are reoriented into the direction of the external electric field ($\theta = 90°$) in the center of the cell and this orientation gradually changes to the surface alignment direction ($\theta = 0°$) at both boundaries. The LC molecules in the center of the cell can easier be reoriented because they are far from both substrates. At a higher driving voltage, the LC molecules prefer to align close to 90°. It is also possible to simulate cells with nonzero pretilt angle boundary conditions. Fig. 7.2c and d give the LC director distributions of cells with different pretilt angles under a 1.5 V driving voltage.

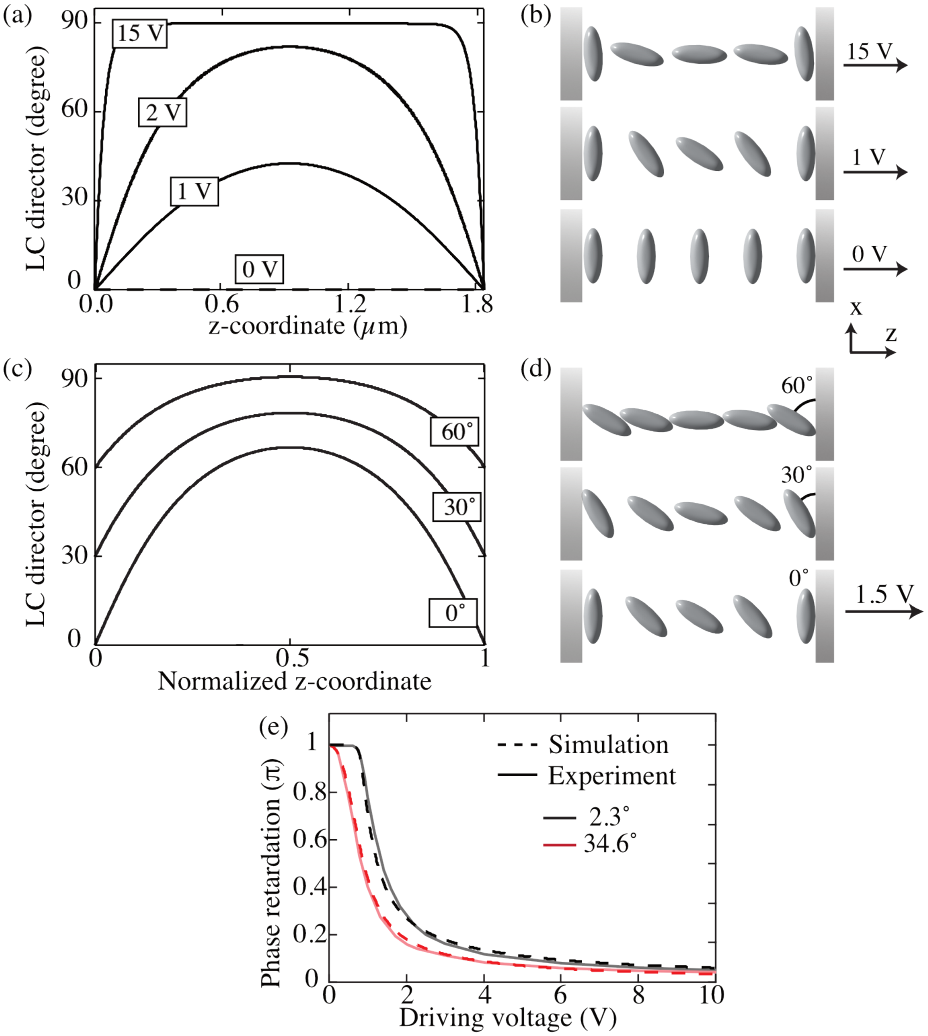

Figure 7.2: Simulation results. (a) The LC director distribution and (b) the schematic LC orientation distribution under different applied voltages for a cell with a 0° pretilt angle. (c) The LC director distribution and (d) the schematic LC orientation distribution for different pretilt angles under a 1.5 V applied voltage. (e) Comparison between the phase retardation curve of the simulation results and the experimental data.

The reliability of the simulation result can be examined by comparing it with the experimental data. As shown in Fig. 7.2e, the simulated phase retardation curves (dashed lines) of cells with different pretilt angles are in good agreement with the experimental date (solid lines). This simulation is therefore a good and reliable method for the investigation of LCD properties.

7.3.2 Existing calculation method

The simulation can provide reliable results for theoretical studies of LC effects, but in order to explain the observed results intuitively, we aim to derive the LC director distribution directly from the free energy equation. Generally, the LC director distribution can not be derived directly from Ericksen-Leslie's equation (Eq. 7.1). To solve this partial differential equation, a calculation method had been developed by simplifying the Ericksen-Leslie's equation with two approximations: one elastic constant and a small tilt angle [5].

One elastic constant

In the one elastic constant approximation, the splay and bend constants are regarded as the same constant ($K = K_1 = K_3$). By using this approximation, the first and second terms of Ericksen-Leslie's equation (Eq. 7.1) are combined and the simplified equation is rewritten as follows.[1]

$$K\frac{\partial^2\theta}{\partial z^2} + \epsilon_0\Delta\epsilon \mathrm{E}^2 \sin\theta\cos\theta = 0 \tag{7.2}$$

For 5CB at room temperature, the splay and bend constants are 6.1×10^{-22} and 8.4×10^{-22} N, respectively. So, we used as the average of the splay and bend constants $K = 7.25 \times 10^{-22}$ N.

Small angle approximation

However, the second order electric field term of Eq. 7.2 is another obstruction for solving Ericksen-Leslie's equation. To simplify the equation, existing studies are limited to LC small tilt angles ($\sin\theta\cos\theta \sim \theta$). By using the small angle approximation [5], the Ericksen-Leslie's equation is simplified as follows:

$$K\frac{\partial^2\theta}{\partial z^2} + \epsilon_0\Delta\epsilon \mathrm{E}^2\theta = 0 \tag{7.3}$$

Under the spatial symmetry and the boundary conditions $\theta(z) = 0$ at $z = 0$ and $z =$ d, the LC director distribution can be derived as

$$\theta\left(z\right) = \theta_m \sin\left(\frac{\pi}{d}z\right) \tag{7.4}$$

---

[1] In this section, we focus on the static properties and neglect the dynamic term $\gamma\frac{\partial\theta}{\partial t}$.

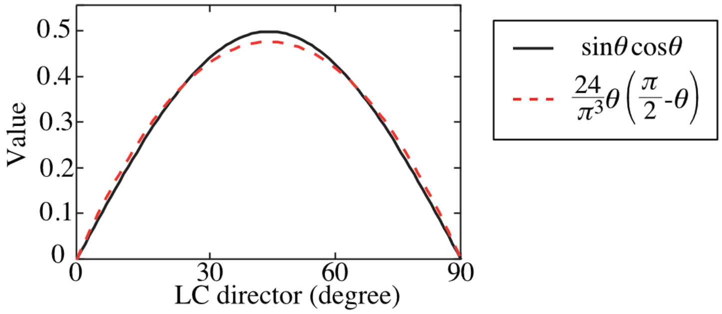

Figure 7.3: The value of $\sin\theta\cos\theta$ (black solid line) and $\frac{\pi^3}{24}\theta(\frac{\pi}{2}-\theta)$ (red dashed line).

where θ_m is the maximum of the LC tilt angle occurring at the center of the cell $z = d/2$.

The solution is simple and clear but with two main problems: (1) The solution is limited to small LC tilt angles. For large LC tilt angles $\theta > 45°$, the electric term $sin\theta cos\theta$ will go to zero for $\theta \to 90°$ while the small angle approximation goes to $\pi/2$. In the previous studies in Ch. 6, the dependence of the static and dynamic LC properties on the pretilt angle was clearly demonstrated but this can not be calculated by this existing calculated method.

7.3.3 New calculation method

To properly derive the LC director distribution, we developed a new calculation method with an improved approximation, based on a full tilt angle range while crossed terms are neglected.

Full tilt angle range

To overcome the small LC tilt angle limitation of the small angle approximation, we improved the simplified equation. Here the electric term $\sin\theta\cos\theta$ is simplified as $\frac{24}{\pi^3}\theta(\frac{\pi}{2}-\theta)$ which vanishes at $\theta = 0$ and $\pi/2$. The normalized constant $\frac{24}{\pi^3}$ is added to achieve the same integral area of both equations from $\theta = 0$ to $\frac{\pi}{2}$. As shown in Fig. 7.3, $\sin\theta\cos\theta$ and $\frac{24}{\pi^3}\theta(\frac{\pi}{2}-\theta)$ have a similar profile. This approximation allows that the calculation follows the full range of the LC director from 0° to 90°.

Base on this improved approximation and the one constant approximation, the static Ericksen-Leslie's equation can be rewritten as

$$K\frac{\partial^2\theta}{\partial z^2} + \epsilon_0\Delta\epsilon \mathrm{E}^2\frac{24}{\pi^3}\theta\left(\frac{\pi}{2}-\theta\right) = 0 \tag{7.5}$$

In a PA cell, the LC pretilt angles on both substrates are the same. Maintaining the spatial symmetry and under the boundary conditions $\theta(z) = \theta_p$ at $z = 0$ and $z =$ d, a general solution of the LC director distribution can be presented as a Fourier series which involves the pretilt angle θ_p as [11]

$$\theta\left(z\right) = \sum_{n\ is\ odd} \mathrm{C}_n \sin\left(\frac{n\pi}{d}z\right) + \theta_p \tag{7.6}$$

where C_n are the Fourier coefficients with index n. The solution has no even index n and no cosine terms because the LC director distribution is symmetric in the center of the cell $z = d/2$.

Crossed term neglected

To derive the Fourier coefficient C_n, the Fourier series (Eq. 7.6) is introduced into the simplified Ericksen-Leslie's equation (Eq. 7.5) as follows.

$$\begin{aligned} & K\frac{\partial^2}{\partial z^2}\left(\sum_{n\ is\ odd}^{\infty} \mathrm{C}_n \sin\left(\frac{n\pi}{d}z\right) + \theta_p\right) \\ & +\epsilon_0\Delta\epsilon \mathrm{E}^2\frac{24}{\pi^3}\left(\sum_{n\ is\ odd}^{\infty} \mathrm{C}_n \sin\left(\frac{n\pi}{d}z\right) + \theta_p\right)\left(\frac{\pi}{2} - \left(\sum_{n\ is\ odd}^{\infty} \mathrm{C}_n \sin\left(\frac{n\pi}{d}z\right) + \theta_p\right)\right) = 0 \end{aligned} \tag{7.7}$$

However, this equation is too complex to directly derive the Fourier coefficients. The equation includes the summation $\sum \mathrm{C}_n$, squared summation $\sum \mathrm{C}_n^2$, crossed summation $\sum\sum \mathrm{C}_m\mathrm{C}_n$ $(m \neq n)$ and constant terms. This equation was solved as follows. First, the crossed summation term $\sum\sum \mathrm{C}_m\mathrm{C}_n$ are eliminated by integrating Eq. 7.7 over the whole LC cell from $z = 0$ to $z =$ d:

$$\begin{aligned} & \int_0^d K\frac{\partial^2}{\partial z^2}\left(\sum_{n\ is\ odd}^{\infty} \mathrm{C}_n \sin\left(\frac{n\pi}{d}z\right) + \theta_p\right) \\ & +\epsilon_0\Delta\epsilon \mathrm{E}^2\frac{24}{\pi^3}\left(\sum_{n\ is\ odd}^{\infty} \mathrm{C}_n \sin\left(\frac{n\pi}{d}z\right) + \theta_p\right)\left(\frac{\pi}{2} - \left(\sum_{n\ is\ odd}^{\infty} \mathrm{C}_n \sin\left(\frac{n\pi}{d}z\right) + \theta_p\right)\right)dz = 0 \end{aligned} \tag{7.8}$$

The cross terms between the different indices n can be excluded, because $m \neq n$, $\int_0^d \mathrm{C}_m \sin\left(\frac{m\pi}{d}z\right) \mathrm{C}_n \sin\left(\frac{n\pi}{d}z\right) dz = \mathrm{C}_m\mathrm{C}_n \int_0^d \sin\left(\frac{m\pi}{d}z\right) \sin\left(\frac{n\pi}{d}z\right) dz = 0$. We call this "crossed terms neglected approximation."

After integration, Eq. 7.8 is reduced to:

$$\sum_{n\ is\ odd}^{\infty} \mathrm{C}_n^2 - \sum_{n\ is\ odd}^{\infty} \frac{4}{n\pi}\alpha_n \mathrm{C}_n \ -\ 2\theta_p\left(\frac{\pi}{2} - \theta_p\right) = 0 \tag{7.9}$$

with

$$\alpha_n = \left(\frac{\pi}{2} - 2\theta_p\right) - K'\frac{n^2}{V_d^2}, \qquad K' = \frac{K\pi^5}{24\epsilon_0\Delta\epsilon}$$

where V_d is the driving voltage which is the integration of the electric field $V_d = Ed$.

To separate the elements in the summation equation, the constant term $2\theta_p(\frac{\pi}{2}-\theta_p)$ is replaced by a summation term $\sum_{n\ is\ odd}^{\infty} \frac{16}{\pi^2 n^2}\theta_p\left(\frac{\pi}{2}-\theta_p\right)$. Now, Eq. 7.9 is rewritten as follows.

$$\sum_{n\ is\ odd}^{\infty}\left[\mathrm{C}_n^2 - \frac{4}{n\pi}\alpha_n \mathrm{C}_n \ - \ \frac{16}{\pi^2 n^2}\theta_p\left(\frac{\pi}{2}-\theta_p\right)\right] = 0 \tag{7.10}$$

Finally, the solution of the Fourier coefficient C_n can be obtained by just solving a simple quadratic equation. Here, we only consider a positive quadratic formula.

$$\mathrm{C}_n = \frac{2}{n\pi}\left(\alpha_n + \sqrt{{\alpha_n}^2 + 4\theta_p\left(\frac{\pi}{2}-\theta_p\right)}\right) \tag{7.11}$$

By introducing Eq. 7.11 into Eq. 7.6, a general solution of the LC director distribution is completely derived from Ericksen-Leslie's equation. The LC director distribution is a superposition of sine waves with the Fourier coefficients C_n.

Here we want to compare the correctness of the calculation results between the existing method and our new method. The LC director distribution cannot be directly measured from an experiment, so the calculation result can only be compared with the simulation result. It should be noticed that both the simulation and calculation results are derived from the Ericksen-Leslie's equation for minimizing the LC distortion and electric free energies.

The LC director distributions calculated by the existing and our new method are plotted in Fig. 7.4a and b, respectively. For the existing calculation result, the LC director distribution is calculated based on Eq. 7.4 and the maximum of the LC tilt angle θ_m obtained from the simulation results. For the new calculation results, the LC director distribution is calculated based on Eq. 7.6 and the Fourier coefficients C_n are obtained from Eq. 7.11. Obviously, the calculation results by using the new calculation method (red solid line) hava a better agreement with the simulation results (dashed line) than the existing calculation method (green solid line), in particular for large voltages.

In a cell with a high driving voltage, most LC molecules prefer to align parallel to the electric field direction. For the existing calculation method, the LC director distribution can only be presented as a half range sine function which means that the LC director decays from 90° in the middle of the cell to 0° at the boundaries. For the new calculation method, if an infinitely large driving voltage is introduced into the Fourier coefficient C_n of Eq. 7.11, then the LC director distribution of Eq. 7.6

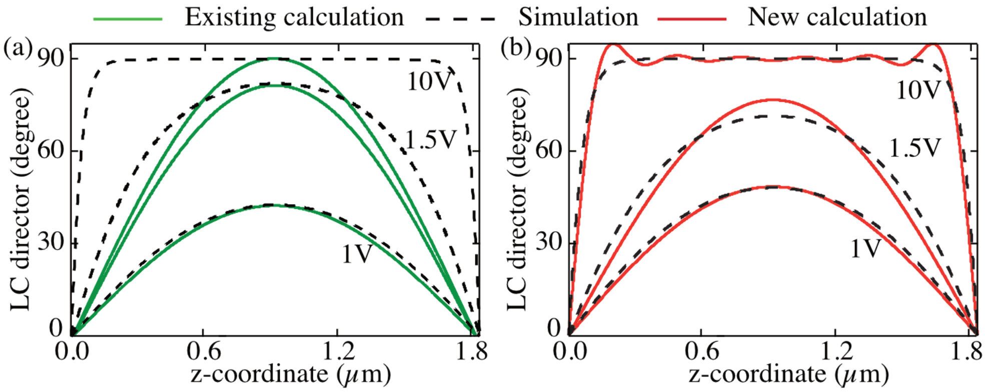

Figure 7.4: (a) Simulation results (black dash lines) and sine function fits (green lines). (b) Simulation results (black dash lines) and the generalised solutions (red lines). The applied voltages are 1, 1.5, and 10V.

becomes the following Fourier series.

$$\theta(z) = \frac{\pi}{2} \sum_{n\ is\ odd} \frac{4}{n\pi} \sin\left(\frac{n\pi}{d} z\right) \tag{7.12}$$

This is a Fourier series of a square function.

$$\theta = \begin{cases} \frac{\pi}{2} & \text{if } 0 < z < d \\ 0 & \text{if } z = 0 \text{ and } d \end{cases}$$

It represents the real LC behavior for which the LC molecules are all parallel to the electric field direction for an extremely high driving voltage.

7.4 Static studies - phase retardation and transmittance

To compare the calculation result with the experimental data, the LC director distribution has to be converted to the phase retardation. Before the conversion, we found that the dependence of the threshold voltage on the pretilt angle can be explained in terms of the LC director distribution. In this section, three LCD properties are discussed subsequently: the threshold voltage, the phase retardation and the contrast ratio.

7.4.1 Threshold voltage

In Ch. 6, we demonstrated the dependence of the LCD performance parameters, such as contrast ratio and response time, on the pretilt angle. Furthermore, the LCD performance parameters are related to the threshold voltage, that indicates when LC molecules can be reoriented by an external electric field.

As is clear from the experimental results of Sec. 6.3.3, for a PA cell with a low pretilt angle, the phase retardation does not change before the driving voltage reaches the threshold voltage. In other words, the threshold voltage is the minimum driving voltage to reorient the LC molecules. However, we found that the flat area and clear turning point in the phase retardation could not be found for the cells with higher pretilt angles. Moreover, according to our definition of the threshold voltage, the threshold voltage exponentially decayed with increasing pretilt angle. Here, we attempt to find a similar pattern from our new calculation method.

In our calculation method, the general solution of the LC director distribution was represented (see Eq. 7.6) as a Fourier series. For the boundary condition and the spatial symmetry, the Fourier basis used the sine function with odd indices. The Fourier coefficient C_n is the amplitude of each basis function. In Fig. 7.5a, the Fourier coefficients C_n are plotted as a function of the driving voltage for a cell with a 0° pretilt angle. Before the driving voltage reaches 0.81 V, all of the Fourier coefficients C_n are zero. In other words, the LC director in the whole cell is 0° and it only starts to rotate above 0.81 V driving voltage. This perfectly corresponds to the threshold voltage we found in the phase retardation experiment.

As shown in Fig. 7.5a, a higher index n comes with a higher threshold voltage of C_n. Therefore, to derive the experimentally observed threshold voltage, only the threshold voltage in the first Fourier coefficient C_1 has to be taken into account. For a planar cell ($\theta_p = 0°$), the first Fourier coefficient of Eq. 7.11 can be rewritten as follows:

$$\mathrm{C}_1 = \frac{2}{\pi}\left(\alpha_1 + \sqrt{\alpha_1^2}\right) = \begin{cases} \frac{4}{\pi}\alpha_1 & \text{if } \alpha_1 > 0 \\ 0 & \text{if } \alpha_1 \leq 0 \end{cases} \tag{7.13}$$

where

$$\alpha_1 = \frac{\pi}{2} - \frac{K'}{V_d^2}\,, \qquad K' = \frac{K\pi^5}{24\epsilon_0\Delta\epsilon} \tag{7.14}$$

Eq. 7.13 indicates that the first Fourier coefficient C_1 stays at zero while $\alpha_n \leq 0$. Therefore, the threshold voltage V_{th} can be obtained from Eq. 7.14 for $\alpha_1 = 0$.

$$V_{th} = \sqrt{\frac{\pi^4}{12}}\sqrt{\frac{K}{\epsilon_0\,\Delta\epsilon}} \tag{7.15}$$

where K is the splay (bend) elastic constant and the $\Delta\epsilon$ is the dielectric anisotropy of the LC. In our case for 5CB with $K = 7.25 \times 10^{-12}$ N and $\Delta\epsilon = 10$, the threshold voltage is calculated as 0.81 V, which is in perfect agreement with the experimental

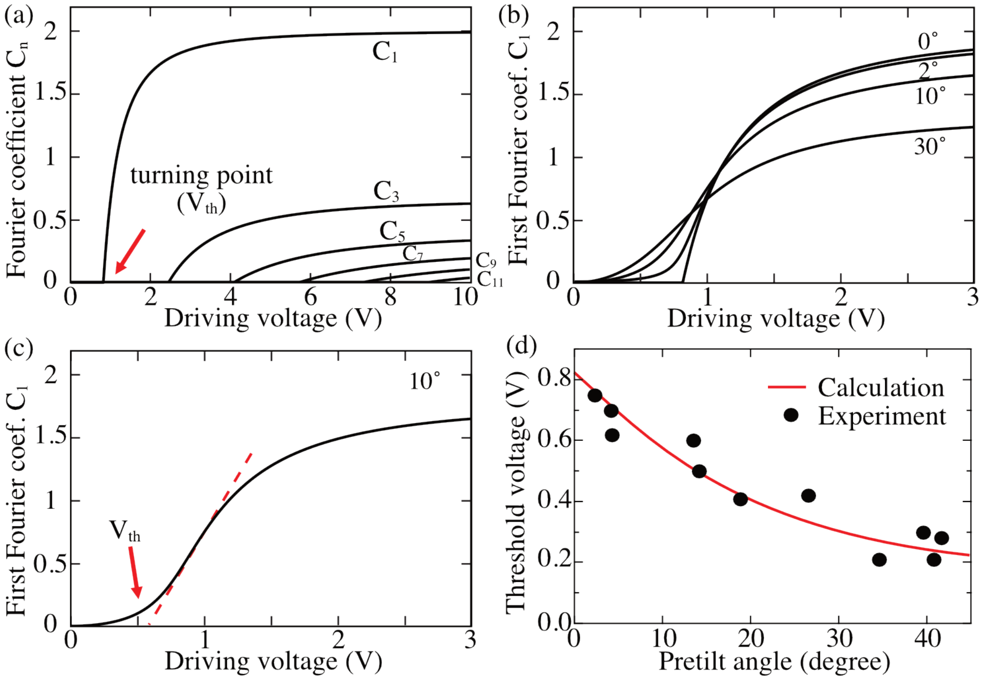

Figure 7.5: (a) C_n for different indices n for the 0° pretilt angle. (b) C_1 for different pretilt angles. (c) C_1 with low pretilt angles; the inset gives the definition of the threshold voltage. (d) Threshold voltages under different pretilt angles. The circles are the experimental data (same as Fig. 6.3c) and the red line is from calculations.

data of Fig. 7.5d. The threshold voltage derived from our calculation method is similar to the Freedericksz transition threshold voltage discussed in Sec. 6.3.2, $V_{th} = \pi\sqrt{\frac{K_1}{\epsilon_0\,\Delta\epsilon}}$ $= 0.83$ V [12, 13].

To investigate the dependence of the threshold voltage on the pretilt angle, the first Fourier coefficients C_1 of cells with different pretilt angles were plotted as a function of driving voltage in Fig. 7.5b. Like the phase retardation curves shown in Fig. 6.3b, the flat area and clear turning point in the first Fourier coefficient cannot be found in a cell with a high pretilt angle. Unexpectedly, even for a cell with a low pretilt angle, such as 2°, the turning point of the threshold voltage also cannot be found.

This phenomenon of the disappearance of a clear turning point in the first Fourier coefficient can be explained by Eq. 7.11. For a cell with a non-zero pretilt angle ($\theta_p > 0°$), the second term $\sqrt{\alpha_n^2 + 4\theta_p\left(\frac{\pi}{2} - \theta_p\right)}$ is always larger than the first term

α_n. Therefore, the Fourier coefficients C_n are always larger than zero if the pretilt angle is larger than zero except the point at 0 V driving voltage. This explains why a clear turning point in the phase retardation experiment in Ch. 6 was not found.

Moreover, using a similar threshold voltage definition of the experimental data in Sec. 6.3.3, we defined the threshold voltage as the cross point from the line of the maximum slope of the curve to the voltage axis (voltage-intercept) (see Fig. 7.5c). As shown in Fig. 7.5d, the calculated result (red line) and the experimental data (circles) are in good agreement. The threshold voltage in the phase retardation can be easily related to the threshold voltage in the first Fourier coefficient. The static calculation method provides a good explanation of the dependence of the threshold voltage on the pretilt angle.

7.4.2 Phase retardation

To compare the calculation results with experimental data from Ch. 6, the LC director distribution has to be derived from the phase retardation which can be measured via the experiment. The relation between the LC director distribution and the phase retardation can be simplified by using several approximations [5, 14]. Here, in order to accurately examine the reliability of the new calculation method, the phase retardation is computed without any approximation and we use the complete geometrical optics relation between the phase retardation $\Delta\phi$ and the LC director distribution $\theta(z)$ as follows:

$$\Delta\phi = \int_0^d \Delta n_{eff}\ k\ dz \tag{7.16}$$

where $\Delta n_{eff} = n_{eff} - n_o$ and $k = \frac{2\pi}{\lambda}$ is the wave number. n_{eff} is the effective refractive index

$$n_{eff} = \left(\frac{\sin^2\theta}{n_o^2} + \frac{\cos^2\theta}{n_e^2} \right)^{-\frac{1}{2}} \tag{7.17}$$

where n_e and n_o are the extraordinary and ordinary refractive indices, respectively [15]. All values and units of constants are listed in Table 7.1 at the end of this chapter.

As shown in Fig. 7.6a, the calculated phase retardation curves for different pretilt angles are in good agreement with the experimental results. It indicates that our new calculation method is indeed reliable for a full range of LC static studies.

7.4.3 Transmittance

The transmittance of the PA cell can be obtained from the phase retardation by using the following equation.

$$T = T_0\ \sin^2\left(\frac{\Delta\phi}{2}\right) \tag{7.18}$$

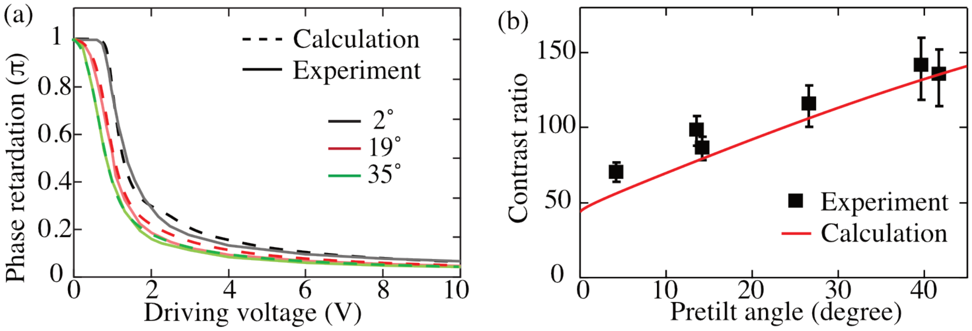

Figure 7.6: (a) The phase retardation of the calculation (dashed line) and experimental result (solid line) for cells with different pretilt angles. (b) The calculation and experimental phase retardations with different pretilt angles.

In Sec. 6.3.1, we demonstrated a high contrast ratio LCD can be achieved by preparing a cell with a higher pretilt angle. Here we used the same contrast ratio definition and cell condition in our calculation method. As shown in Fig. 7.6, the calculation results and experimental data are in good agreement. The calculation results confirm that a cell with a higher pretilt angle indeed gives rise to a high contrast ratio.

7.5 Dynamic studies - response time

For static LC studies, a new and proper calculation method was demonstrated in the previous section, which provides a solution for a wide range of LC tilt angles. In this section, the time dependence is added into our calculation method to compare with the LC dynamic studies. The LC dynamic effects are mainly classified into two types: turn off and turn on times, which depend on the LC director change and optical response.

The switching times of the optical response are obtained by transmittance measurements. It was also investigated in Ch. 6 and the turn off and turn on times are noted as t_{off} and t_{on}, respectively. In the definitions of Sec. 6.4, the words, turn on and turn off, were related to describing the behavior of the driving voltage switching, instead of the optical switching.

The response times of the LC director are used in the theoretical studies to describe the reorientation speed of LC molecules. To avoid the confusion with the switching times of the optical response, we call them rise and relaxation times of the LC director and note them as τ_{rise} and τ_{relax}, respectively. Here the words, rise and relax, were related to describing the behavior of the LC director. For a PA cell operating between 0 V and 15 V, rise and relaxation represent the LC director from θ_p to $\sim 90°$ and from ∼ 90° to θ_p, respectively. Here θ_p is the pretilt angle which is the initial LC tilt angle without applying any driving voltage.

Firstly, in Sec. 7.5.1, we derive the rise time τ_{rise} and relaxation time τ_{relax} and compare the calculated time-dependent LC director distributions with simulated results. Then, in Sec. 7.5.2, to derive the relations between the optical response time and the pretilt angle, the phase retardation equation is simplified by using a uniform LC director distribution approximation. In Sec. 7.5.3, the calculated turn off time t_{off} and turn on time t_{on} are derived and compared with the experimental data of Sec. 6.4.1 and 6.4.2.

7.5.1 Relaxation time and rise time

To study the dynamic properties, we also start from the Ericksen-Leslie's equation. The time dependence is added into the simplified static Ericksen-Leslie's equation (Eq. 7.5).

$$K\frac{\partial^2\theta}{\partial z^2}+\epsilon_0\Delta\epsilon \mathrm{E}^2\frac{24}{\pi^3}\theta\left(\frac{\pi}{2}-\theta\right)=\gamma\frac{\partial\theta}{\partial t} \tag{7.19}$$

Here we used the same method as used in the static calculation in Sec. 7.3.3: one elastic constant and a full tilt angle range.

Relaxation time

For the relaxation time calculation, the driving voltage is switched off from V_d to 0 V at time $t = 0$. Then the LC director relaxes from $\theta(V_d)$ to the initial angle θ_p. Because no electric field is involved ($E = 0$), the Ericksen-Leslie's equation (Eq. 7.19) is simplified to

$$K\frac{\partial^2\theta}{\partial z^2}=\gamma\frac{\partial\theta}{\partial t} \tag{7.20}$$

According to the well-known solution of this partial differential equation, the LC director distribution can be simply derived as

$$\theta\left(z\right)=\sum_{n\ is\ odd}^{\infty}\mathrm{C}_n\sin\left(\frac{n\pi}{d}z\right)e^{-\frac{n^2t}{\tau_{relax}}}+\theta_p \tag{7.21}$$

with the relaxation time constant τ_{relax}

$$\tau_{relax}=\frac{\gamma d^2}{K\pi^2}$$

where C_n are the Fourier coefficients of the static calculation (Eq. 7.11). In an exponential decay function, the relaxation time τ_{relax} stands for the relaxation speed that the LC director reduces to $e^{-1} = 0.37$ times its initial value. The corresponding parameters were listed in Table 7.1 at the end of this chapter.

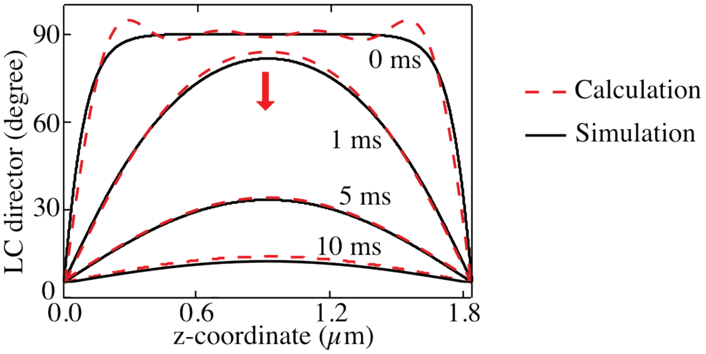

Figure 7.7: The LC director distribution of the calculation (red dashed line) and simulation (black solid line) which are switched off from 15 V for cells with the 5° pretilt angle.

Fig. 7.7 gives an example of a cell with a 5° pretilt angle, showing how the LC director distribution relaxes from 15 V. The calculated result is in good agreement with the simulation result. For the relaxation time derivation (see Eq. 7.20), only the one constant approximation is used because no electric term is involved. It is the reason why the calculation result has such a good agreement with the simulation results in Fig. 7.7.

Rise time

To derive the rise time, we use the same approximations as those used in the static study. The dynamic LC orientation can be obtained by solving the simplified Ericksen-Leslie's equation (Eq. 7.19) with the separation of variables method. The LC orientation can be regarded as the product of the LC director spatial distribution and its time dependence:

$$\theta\left(z\right)=\sum_{n\ is\ odd}^{\infty}\mathrm{C}_n\sin\left(\frac{n\pi}{d}z\right)A_n\left(t\right)+\theta_p \tag{7.22}$$

By using the "crossed term neglected approximation" introduced in Sec. 7.3.3, the simplified Ericksen-Leslie's equation (Eq. 7.19) becomes

$$\sum_{n\ is\ odd}^{\infty}\mathrm{C}_n^2A_n^2-\sum_{n\ is\ odd}^{\infty}\frac{4}{n\pi}\alpha_n\mathrm{C}_nA_n+\sum_{n\ is\ odd}^{\infty}\frac{4}{n\pi}\beta\mathrm{C}_n\frac{\partial A_n}{\partial t}-2\theta_p\left(\frac{\pi}{2}-\theta_p\right)=0 \tag{7.23}$$

with

$$\beta=\frac{\gamma}{\epsilon_0\Delta\epsilon E^2}\frac{\pi^3}{24} \tag{7.24}$$

By solving the above equation, the time-dependent part $A_n(t)$ is obtained as follows.

$$A_n\left(t\right) = \frac{2}{n\pi}\frac{1}{\mathrm{C}_n}\left(\alpha_n + \sqrt{{\alpha_n}^2 + 4\theta_p\left(\frac{\pi}{2} - \theta_p\right)}\tanh\left(\frac{1}{2}\frac{t - t_{0,n}}{\tau_{rise}}\right)\right) \tag{7.25}$$

with

$$\tau_{rise} = \frac{\beta}{\sqrt{{\alpha_n}^2 + 4\theta_p\left(\frac{\pi}{2} - \theta_p\right)}} \tag{7.26}$$

where τ_{rise} is the rise time constant, which is related to the response speed of the LC director change, and t_0 is the delay time. For a $\tanh(x)$ function, the maximum slope appears at $x = 0$. This means the LC director changes most rapidly at the delay time $t = t_0$.

At the moment $t = 0$, no driving voltage is applied. The time dependent term $A_n\left(t\right)$ equals to zero because all the LC molecules align along the pretilt angle direction. By giving an initial value of the time dependent term $A_n\left(t = 0\right) = 0$, the delay time constant t_0 can be derived as

$$t_0 = 2\tau_{rise}\tanh^{-1}\left(\frac{\alpha_n\left(V_a\right)}{\sqrt{\alpha_n\left(V_a\right)^2 + 4\theta_p\left(\frac{\pi}{2} - \theta_p\right)}}\right) \tag{7.27}$$

Fig. 7.8 shows the dynamic change of the LC director distribution from calculations and simulations. The driving voltage is switched on from 0 V to 15 V at $t = 0$. The calculated curves correspond to simplified Ericksen-Leslie's equation (Eq. 7.19) and the simulated ones are the solution of original Ericksen-Leslie's equation (Eq. 7.1). The calculation method is shown to be highly reliable given the good agreement with the simulation results.

7.5.2 Simplified phase retardation

So far, in order to accurately examine the reliability of the new calculation method, the phase retardation and the transmittance are computed from the LC director distribution by using the equations without any approximation (Eq. 7.16 and 7.18). However, to directly represent the relations between the LCD properties and the pretilt angle, the phase retardation equation has to be simplified. The expression for the phase retardation can be simplified by assuming the LC director distribution to uniformly align with an LC average director θ_{avg} in the whole cell (see Fig. 7.9a). The average director θ_{avg} is defined as follows.

$$\theta_{avg} = \frac{1}{d}\int_0^d \theta\left(z\right)dz \tag{7.28}$$

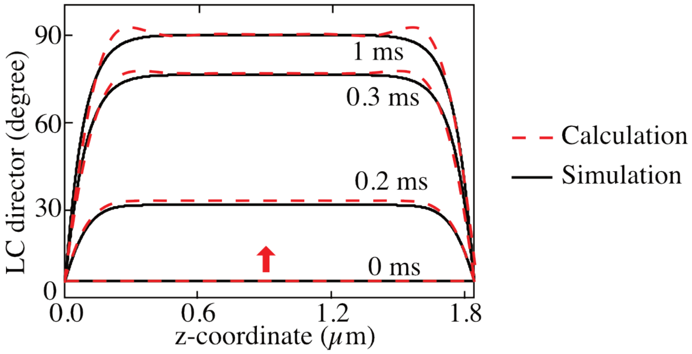

Figure 7.8: The LC director distribution of the calculation (red dashed line) and simulation (black solid line) which are switched on from 0 V to 15 V for cells with the 5° pretilt angle.

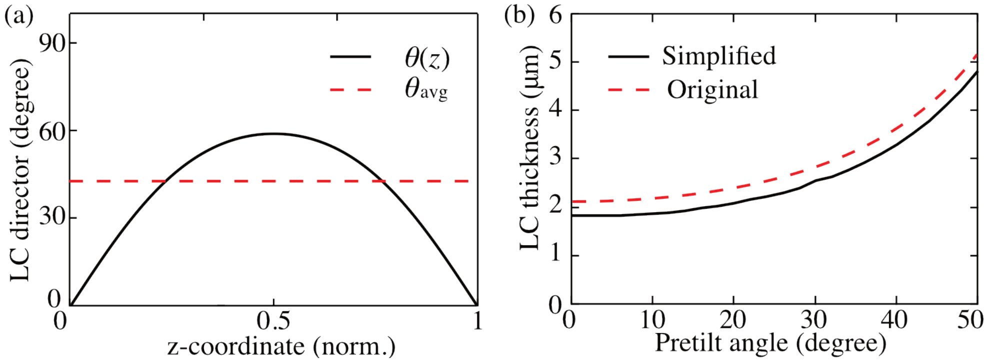

Figure 7.9: (a) The average LC director for the phase retardation simplification. (b) The calculated LC thickness as a function of the pretilt angle to reach the phase retardation $\Delta\phi = \pi$. The red dashed line is based on Eq. 7.22 which is derived from the simplified phase retardation. The black solid line is from the calculation without any approximation.

For a cell with a uniform LC director θ_{avg}, the integration of the phase retardation equation (Eq. 7.16) is then simplified to:

$$\begin{aligned}\Delta\phi \sim\ & \Delta n_{eff}\left(\theta_{avg}\right)\ k\ d \\ =\ & n_o\ \left(\left(1-n'\ \cos^2\theta_{avg}\right)^{-\frac{1}{2}}-1\right)\ k\ d\end{aligned} \tag{7.29}$$

where $n' = \frac{n_e^2-n_o^2}{n_e^2} = 0.195$. Because the term $n'\ \cos^2\theta_{avg}$ is much smaller than 1, the phase retardation equation can be simplified again:[2]

$$\Delta\phi\ =\ \frac{1}{2}\,n_0\,n'\ \cos^2\theta_{avg}\ k\ d \tag{7.30}$$

On the other hand, according to the above equation, the required LC thickness for a PA cell can be derived by putting the phase retardation $\Delta\phi = \pi$.

$$d = \frac{\pi}{n_o k}\left(\left(1-n'\cdot\cos^2\theta_p\right)^{-\frac{1}{2}}-1\right)^{-1} \tag{7.31}$$

As shown in Fig. 7.9b, the LC thickness calculated with the simplified phase retardation (red dashed line) is in good agreement with the LC thickness calculated without any approximation (black solid line). This simplified LC thickness calculation method will be used in the LC dynamic studies.

7.5.3 Turn off time and turn on time

Turn off time

Now we go further to investigate the calculation for the turn off time on the transmittance. The final goal is to find out the correlation between the turn off time and the pretilt angle. In the experiments, the turn off time is defined as the time that the transmittance increases from $T = 10\%$ to $T = 90\%$. In the calculation, the turn on time can be derived based on the calculation result of the LC director relaxation time. It is simple to derive the phase retardation $\Delta\phi$ from the LC director distribution $\theta(z)$ by using Eq. 7.16. However, it is too difficult to derive the equations because the effective refractive index (Eq. 7.17) is too complex for the integration (Eq. 7.16), especially when the LC director distribution is represented as a Fourier series which is a summation of sine functions (Eq. 7.6). In order to derive the phase retardation, we need to simplify the equations.

In Sec. 6.4.1, LC cells were operated by applying the driving voltage between 0 V and 15 V. As shown by the experimental result in Fig. 7.6a, the phase retardation almost goes to zero at a 15 V driving voltage, which means that most LC molecules

---

[2] If $a << 1$, $(1+a)^{-\frac{1}{2}} \sim 1-\frac{1}{2}a$

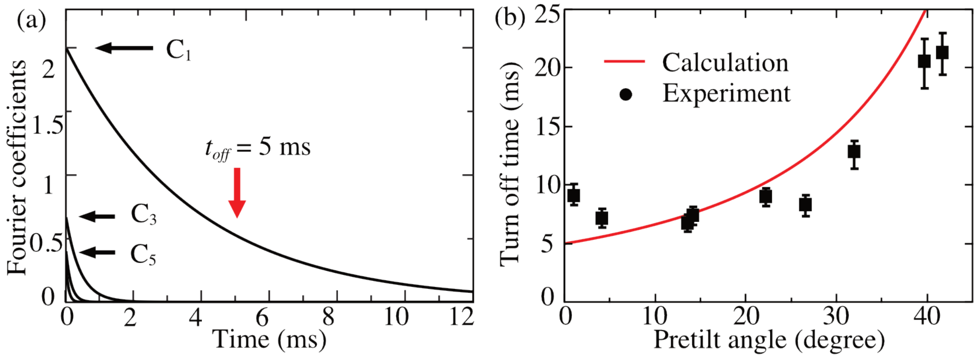

Figure 7.10: (a) The time-dependent Fourier coefficients C_n change for different indices n. (b) Comparison of calculation results and experimental data of the turn off times for cells with different pretilt angle.

align to 90°. Therefore, we assume that the LC director distribution at a 15 V driving voltage can be presented as a square function of the Fourier series (Eq. 7.12). If a high enough driving voltage is applied, the time-dependent LC director distribution (Eq. 7.21) can be simplified as follows.

$$\theta\left(z\right) \; = \; \sum_{n\ is\ odd}^{\infty} \frac{4}{n\pi}\left(\frac{\pi}{2}-\theta_p\right)\,\sin\left(\frac{n\pi}{d}z\right)\; e^{-\frac{t}{n^2\,\tau_{relax}}} + \theta_p \tag{7.32}$$

In both calculated and experimental results, the time for the transmittance change from 0% to 10% is so fast that it can be neglected. A simplified turn on time is calculated as the time for the transmittance change from 0% to 90% to replace the experimental definition from 10% to 90%. While the transmittance increases from 0% to 90%, the LC director decays from 90° to $\sim\theta_p$. By examining the equation of the LC director distribution (Eq. 7.32), the LC director dynamic behavior can be explained by how the Fourier coefficient decays from the maximum at $t = 0$ to zero at $t = \infty$. The relaxation time term $\frac{\tau_{relax}}{n^2}$ implies that the Fourier coefficient C_n for a higher index ($n \leq 3$) decays n^2 times faster than the first Fourier coefficient C_1. As the calculation results of the time-dependent Fourier coefficient C_n shown in Fig. 7.10a, the Fourier coefficient with a higher index ($n \leq 3$) decreases to zero very fast. At the measured turn off time t_{off} of a cell with a low pretilt angle ($\sim$ 5 ms), only the first Fourier coefficient C_1 has to be taken into account in the calculation. To calculate the time for $T = 90\%$, the calculation can be simplified by only calculating the first index $n = 1$ as follows.

$$\theta\left(z\right) \; = \; \frac{4}{\pi}\left(\frac{\pi}{2}-\theta_p\right)\,\sin\left(\frac{\pi}{d}z\right)\; e^{-\frac{t}{\tau_{relax}}} + \theta_p \tag{7.33}$$

According to the simplified method of the phase retardation in Sec. 7.5.2, the LC director distribution $\theta(z)$ (Eq. 7.33) is simplified to be a uniform average LC director θ_{avg}.

$$\theta_{avg} \;=\; \frac{8}{\pi^2}\left(\frac{\pi}{2}-\theta_p\right)\; e^{-\frac{t}{n^2\;\tau_{relax}}} \;+\; \theta_p \tag{7.34}$$

According to the relation between the transmittance and the phase retardation (Eq. 7.18), the phase retardation equals to $\Delta\phi_{90\%} = 0.795$ for the transmittance $T = 90\%$. By introducing the LC average director (Eq. 7.34) into the simplified phase retardation (Eq. 7.30) and solving it with $\Delta\phi_{90\%} = 0.795$, the relation between the turn off time and the pretilt angle is derived.

$$t_{off} \;=\; \tau_{relax}\;\ln\left(\frac{\pi}{8}\,\frac{\cos^{-1}\left(\sqrt{\Delta\phi_{90\%}}\;\cos\theta_p\right)-\theta_p}{\frac{\pi}{2}-\theta_p}\right) \tag{7.35}$$

Note that the relaxation time τ_{relax} is also dependent on the pretilt angle because the cells with different pretilt angles are prepared with different LC thicknesses (Eq. 7.31).

$$\tau_{relax} = \frac{\gamma d^2}{K\pi^2} = \frac{\gamma}{K\pi^2}\left(\frac{\pi}{\frac{1}{2}k\;n_0\;n'\cos\theta_p}\right)^2 \tag{7.36}$$

In Fig. 7.10b, the calculation result based on Eq. 7.35 has a good agreement with experimental data of Sec. 6.4.1. Moreover, the calculation method (Eq. 7.35) provides a good explanation why the turn off time increases with the pretilt angle.

Turn on time

For the turn on time calculation, we use the similar method as in the turn off time section. To derive the phase retardation from the LC director distribution, first, we use the average director approximation (Sec. 7.5.2). By using the definition of the average director (Eq. 7.28), the rise time of the LC director distribution (Eq. 7.22) can be simplified as follows.

$$\theta_{avg} = \sum_{n\ is\ odd}^{\infty}\frac{4}{n^2\pi^2}\left(\alpha_n+\sqrt{\alpha_n^2+4\theta_p\left(\frac{\pi}{2}-\theta_p\right)}\tanh\left(\frac{1}{2}\frac{t+t_0}{\tau_{rise}}\right)\right)+\theta_p \tag{7.37}$$

For a large index n, the contribution of $\frac{1}{n^2}$ is very small. Therefore, the average director is simplified by only taking the low index n into account. Moreover, the square of the driving voltage V_d^2 is much larger than the square of the low index n^2, the term α_n is simplified by neglecting the voltage dependence.[3].

$$\alpha_n = \left(\frac{\pi}{2} - 2\theta_p\right) - K' \frac{n^2}{V_d^2} \sim \frac{\pi}{2} - 2\theta_p \tag{7.38}$$

Therefore, Eq. 7.37 can be further simplified.[4]

$$\theta_{avg} = \frac{\pi}{4}\left(1 + \tanh\left(\frac{1}{2}\frac{t + t_0}{\tau_{rise}}\right)\right) \tag{7.39}$$

By introducing the LC average director (Eq. 7.39) into the simplified phase retardation (Eq. 7.30), the relation between the turn on time for reaching a transmittance $T = x\%$ and the pretilt angle is derived.

$$t_{on,\,T} = 2\,\tau_{rise} \tanh^{-1}\Big(\frac{4}{\pi}\cos^{-1}(\sqrt{\Delta\phi_T}\ \cos\theta_p) - 1\Big) + t_0 \tag{7.40}$$

Here we want to calculate the turn on time which is defined as the time for the transmittance change from $T = 10\%$ to $T = 90\%$. Following Eq. 7.40, the turn on time can be derived as follows.

$$\begin{aligned} t_{on} &= t_{on,\,10\%} - t_{on,\,90\%} \\ &= 2\,\tau_{rise}\Bigg[\tanh^{-1}\Big(\frac{4}{\pi}\cos^{-1}(\sqrt{\Delta\phi_{10\%}}\ \cos\theta_p) - 1\Big) \\ &\qquad - \tanh^{-1}\Big(\frac{4}{\pi}\cos^{-1}(\sqrt{\Delta\phi_{90\%}}\ \cos\theta_p) - 1\Big)\Bigg] \end{aligned} \tag{7.41}$$

According to the relation between the transmittance and the phase retardation (Eq. 7.18), the phase retardation is changed from $\Delta\phi_{10\%} = 0.205$ to $\Delta\phi_{90\%} = 0.795$.

Fig. 7.11a is the calculation result based on Eq. 7.41. In the high pretilt angle region, the calculation result has a good agreement with the experimental data. However, in the low pretilt angle region, the calculation result is lower than the experimental data. As shown in Fig. 7.11b, we further plot the times for reaching the transmittances $T = 10\%$ and $T = 90\%$ by using Eq. 7.40. In Fig. 7.11b, the transmittances both increase rapidly while the pretilt angle decreases to around zero. According to Eq. 7.41, the weight of the rise time constant τ_{rise} becomes much larger for a low pretilt angle. The uncertainty which is generated during the simplified calculation method is enlarged. Therefore in the low pretilt angle region, the calculation result does not perfectly fit to the experimental data.

---

[3] In the experiments, a square wave with a peak-to-peak 15 V driving voltage was applied for a dark state of a LC cell. It equals to a root mean square 7.5 V driving voltage used in the calculation.

[4] $\sum_{n\ is\ odd}^{\infty} \frac{4}{n^2\pi^2} = \frac{1}{2}$

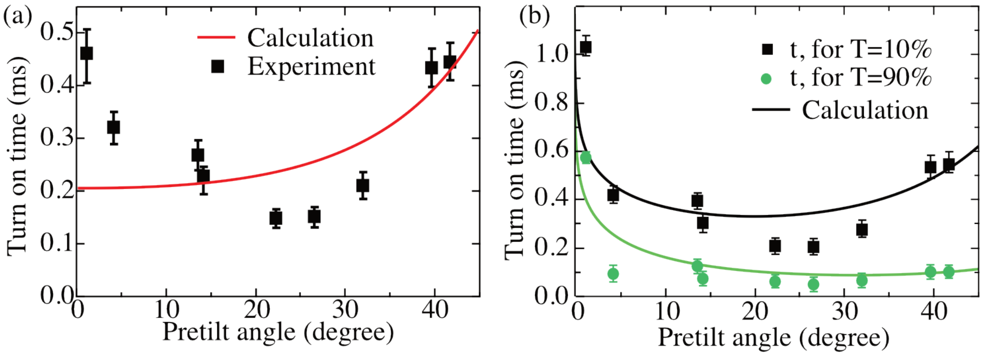

Figure 7.11: (a) Comparison between calculated results and experimental data of the turn on times for cells with different pretilt angles. (b) Comparison between calculated results and experimental data of the switching time to reach the transmittance $T = 10\%$ and $T = 90\%$ for cells with different pretilt angles.

7.6 Summary

A new improved calculation method has been developed for the static and dynamic LC studies that includes the pretilt angle and goes beyond the small angle approximation. In both static and dynamic LC studies, the calculation results are in good agreement with the experimental results demonstrated in Ch. 6. The calculation is a reliable method to predict the static and dynamic performances, such as contrast ratio and response time, for a wide range of PA cells.

Constant	Symbol	Value	Unit (SI)	Note	Ref
Distortion	K_1	6.1×10^{-12}	N	splay	[16]
	K_3	8.4×10^{-12}	N	bend	[16]
	K	7.25×10^{-12}	N	$\frac{1}{2}(K_1+K_3)$	[16]
Dielectric anisotropy	$\Delta\epsilon$	10			[17]
Refractive index	n_e	1.707		extraordinary	[15, 18]
	n_o	1.532		ordinary	[15, 18]
Rotational viscosity	γ	0.08	Pa·s		[19]

Table 7.1: The 5CB constants used in this study for simulation and calculation.

References

[1] L. Weng, P.-C. Liao, C.-C. Lin, T.-L. Ting, W.-H. Hsu, J.-J. Su, and L.-C. Chien, AIP Advances **5**, 097218 (2015).

[2] X. Nie, H. Xianyu, R. Lu, T. X. Wu, and S.-T. Wu, Journal of Display Technology **3**, 280 (2007).

[3] D.-K. Yang and S.-T. Wu, *Fundamentals of Liquid Crystal Devices* (John Wiley & Sons, 2014).

[4] G. Meier, E. Sackmann, and J. G. Grabmaier, *Applications of Liquid Crystals* (Springer Science & Business Media, 2012).

[5] S.-T. Wu and C.-S. Wu, Applied Physics Letters **53**, 1794 (1988).

[6] M. Schadt and F. Muller, Electron Devices, IEEE Transactions on **25**, 1125 (1978).

[7] A. V. Zakharov and R. Y. Dong, Physical Review E **64**, 031701 (2001).

[8] F. J. Kahn, Applied Physics Letters **20**, 199 (1972).

[9] T. Rasing and I. Musevic, *Surfaces and Interfaces of Liquid Crystals* (Springer Science & Business Media, 2013).

[10] I. Dierking, *Textures of Liquid Crystals* (John Wiley & Sons, 2006).

[11] J. W. Dettman, *Mathematical Methods in Physics and Engineering* (Courier Corporation, 2013).

[12] V. Fréedericksz and V. Zolina, Transactions of the Faraday Society **29**, 919 (1933).

[13] P. G. de Gennes and J. Prost, *The Physics of Liquid Crystals* (Oxford University Press, 1993).

[14] S.-T. Wu and C. S. Wu, Physical Review A **42**, 2219 (1990).

[15] R. G. Horn, Journal de Physique **39**, 105 (1978).

[16] J. D. Bunning, T. E. Faber, and P. L. Sherrell, Journal de Physique **42**, 1175 (1981).

[17] B. R. Ratna and R. Shashidhar, Pramana **6**, 278 (1976).

[18] J. Li, C. H. Wen, S. Gauza, R. Lu, and S. T. Wu, Journal of Display Technology **1**, 51 (2005).

[19] H. Kneppe, F. Schneider, and N. K. Sharma, The Journal of Chemical Physics **77**, 3203 (1982).

CHAPTER 8

Multi-domain System

8.1 Introduction

In liquid crystal displays (LCDs), the viewing angle is one of the important properties, in particular for large screen applications. In order to reach the maximum angle at which a display can be observed with proper contrast ratio and gray scale, the viewing angle has to be designed as wide as possible [1]. To achieve a wider viewing angle, two main technologies had been developed: front diffusing film [2–4] and multi-domain liquid crystal (LC) orientation [5]. For the diffuser technology, a diffusing film is attached on the front surface of LCDs to diffuse the light into various angles. A diffusing film can reduce the viewing angle dependence, but it also causes a blur of the image [6]. For a multi-domain LC orientation system, the LC molecules align into different directions in different domains in the sub-pixels; the viewing angle dependence in each pixel is compensated by averaging the transmittance over domains (see the introduction in Sec. 2.3.4). Several multi-domain modes had been developed, such as multi-domain vertical alignment (MVA) [7–9] and multi-domain twisted nematic [10–12]. The key technological challenge of a multi-domain mode is how to control the LC pretilt angle precisely in each domain. The pretilt angle is defined as the angle between the substrate and the LC long axis in the surface layer.

The LC surface alignment layer which determines the LC pretilt angle is a crucial

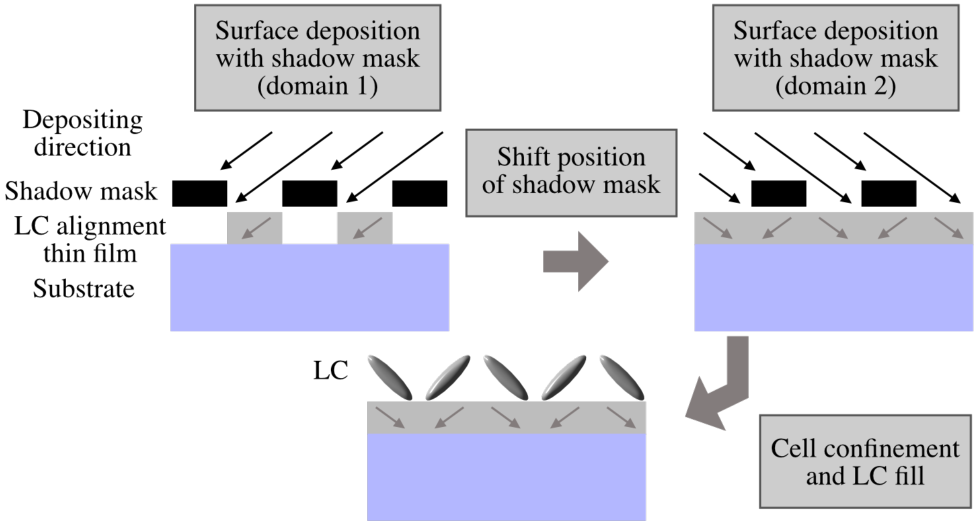

Figure 8.1: The concepts of a dual-domain LC alignment layer by depositing LC alignment layer with shadow masks. The arrows in the LC alignment thin film are used to present the depositing direction. Note that the pretilt angle may not equal to the depositing angle.

part of an LCD. The velvet rubbing treatment is the simplest and low-cost alignment technology with advantages of high transparency and chemical stability [13, 14]. By rubbing the substrate which is coated with a polyimide (PI) thin film, a liquid crystal molecule can be oriented by this surface. The rubbed polyimide thin film presents a planar alignment in which the LC molecules are oriented parallel to the substrate and along the rubbing direction. However, for a multi-domain system, complicated lithography processes have to be applied to control different LC alignment directions in each domain [10]. Moreover, a rubbing treatment cannot be used for a wide pretilt angle control. Therefore, we aim to find an LC surface alignment method that can control the pretilt angle and this method can be simply applied to a multi-domain system.

In Ch. 4, we presented a reliable surface alignment method; by obliquely depositing a Fe_2O_3/Cr_2O_3 thin film on a PI-coated substrate, this substrate can control the LC pretilt angle precisely from 0° to 45°. In Ch. 6, comparing to the vertical alignment (VA) mode, we showed an inversely voltage operation LCD mode called "parallel alignment (PA) mode with pretilt angle controlled." We demonstrated that good LCD performances, such as the contrast ratio and response time, can be achieved for a PA cell with a proper pretilt angle. Depositing a thin film is a suitable LC alignment technology [15–17] which can also be applied to a multi-domain system by using a shadow mask lithography technology [18]. As the concepts shown in Fig. 8.1, an LC alignment layer can be physically deposited by evaporation [15] or sputtering [19, 20] through the shadow mask onto a selective area of a substrate. In this way, a small domain LC control can be achieved, resulting in a simpler fabrication with two steps film deposition comparing with a complex photolithographic process in a dual-domain PI system [10].

In this chapter, we demonstrate how to achieve a wider viewing angle by making a dual-domain cell with the surface alignment method demonstrated in Ch. 4. First, the sample preparation and measurement methods are introduced in Sec. 8.2. In Sec. 8.3, we observe the pretilt angle behavior in this dual-domain system. In Sec. 8.4, the dependence of the transmittance and the contrast ratio on the viewing angle for a dual-domain cell are measured. To examine the improvement of the viewing angle, the experimental results of a dual-domain cell are compared with a single-domain cell.

8.2 Sample

Following the sample preparation steps in Sec. 3.2, we first spin-coated polyimide on a cleaned 1×2 cm^2 ITO-glass and the thickness of the PI layer measured by ellipsometer was c.a. 300 nm. To obtain a dual-domain alignment layer, a PI-coated substrate was covered with a 1 mm thick shadow mask (MACOR, Corning) during the

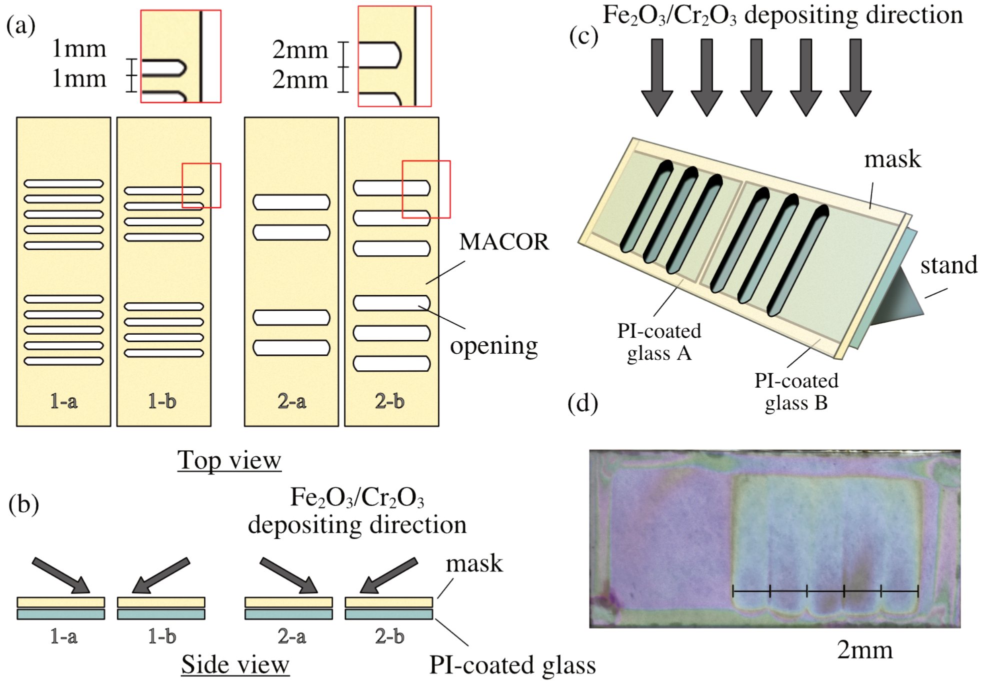

Figure 8.2: The shadow masks and the substrate preparation. (a) The shadow masks and their dimensions. There were two pairs of masks with 1mm and 2mm domain widths. (b) The shadow mask a and b with different Fe_2O_3/Cr_2O_3 depositing directions (gray arrows). (c) Setup of the substrate fabrication. (d) Dual-domain substrate with a 2 mm domain width.

alignment layer depositing process.[1] As shown in Fig. 8.2c, a shadow mask and two PI-coated substrates (A and B) were set on the anode (bottom electrode) with a stand for keeping the sample at 60° with respect to the horizontal. Then a thin film was obliquely deposited on the substrate through the selective opening areas by sputtering the stainless steel target (SUS 304, EIKO Engineering Co., Ltd.). The composition of the deposited thin film was identified as Fe_2O_3/Cr_2O_3 by X-ray photoemission spectroscopy (see Sec. 5.3.1).

In this study, for 1 mm and 2 mm domain widths, two pairs of masks were prepared (see 1-a/1-b and 2-a/2-b in Fig. 8.2a).[2] For each domain width, two masks were used

---

[1] MACOR is an electric insulator and remains stable at 800°C.

[2] Note that the domain width of our hand-made shadow mask was limited to the resolution of our milling machine (1 mm). Nowadays, shadow mask is a mature technology which can be used for a

to cover different regions for different Fe_2O_3/Cr_2O_3 depositing directions (see Fig. 8.2b). For instance, in a dual-domain substrate preparation for a 2 mm width and a 30 minute depositing time, we set the mask 2-a on two substrates (see Fig. 8.2c) and deposited the thin film in 30 minutes. Then we swapped the positions and changed the directions of the two substrates. The substrates were covered with the mask 2-b to deposit Fe_2O_3/Cr_2O_3 on the other areas of the substrates with the different depositing direction (see Fig. 8.2b) in 30 minutes. After the two steps deposition, as shown in Fig. 8.2d, the dual-domain substrates were prepared for a 2 mm domain width. In this chapter, all of the substrates were prepared under the same ion beam currents and sputter voltages at 5 mA and 560 V, respectively.

Then two Fe_2O_3/Cr_2O_3-deposited substrates were combined as an anti-parallel alignment cell and sandwiched with Mylar spacers. Here top and bottom substrates had to be aligned well to make sure that the alignment layer was anti-parallel in each domain. The empty cells were filled with 4'-n-pentyl-4-cyanobiphenyl (5CB, Merck) at 60°C and annealed to room temperature.

In the PA mode, the cell was operated between 0 V and V_d driving voltages for the bright and the dark states, respectively, The cell thickness had to be designed in such a way to reach an initial phase retardation of π which is the bright state without any driving voltage. For a dual-domain measurement, such as the viewing angle dependence, the laser beam had to cover at least two domains. The laser beam was expanded to 2 mm or 4 mm spot size for the measurement of the 1 mm or 2 mm domain width cell, respectively (see Fig. 8.3a and d). With a spot size larger than 2 mm, the LC thickness in the measured area was not uniform anymore for a wedge cell, which is used for a thickness control of a single-domain cell in Ch. 6. We found a solution by adding two clips on the cell inside the Mylar positions (see Fig. 8.3b). Due to the force from the clips, the substrates were slightly bent and the LC thickness at the center of the cell d_c was smaller than the Mylar thickness d_m. By shifting the positions of the two clips, we could make a uniform LC thickness in two domains and the thickness cell be controlled for achieving the initial phase retardation of π. Moreover, to examine the improvement of the viewing angle dependence, we also measured LC properties for a single-domain by using a focused laser beam (see Fig. 8.3a and c).

8.3 Pretilt angles on a dual-domain alignment surface

A polarizing optical microscope (POM) is widely used for the LC alignment investigation by observing the texture of a cell between a pair of crossed polarizers (see Sec. 3.3.1) [23, 24]. The uniformity and the type of the alignment layer can be observed

---

small domain deposition with a feature size ≤ 20 µm [21]. The resolution of this line width is high enough for a sub-pixel of a practical multi-domain LCD (180 µm × 500 µm) [22].

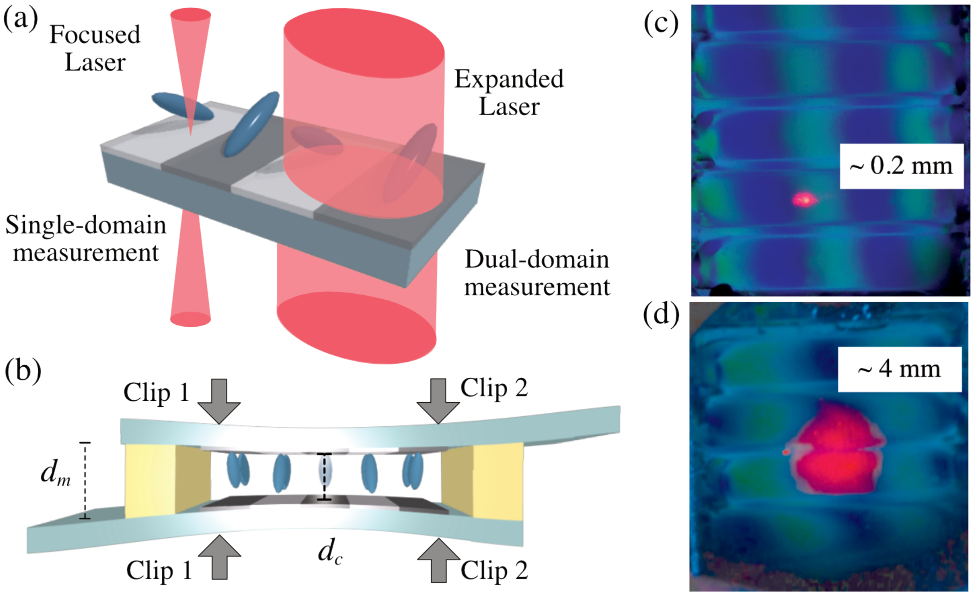

Figure 8.3: Cell structure and measured area. (a) Schematic diagram of the cell structure and laser beam sizes. In every experiment, we only measured one spot of the cell by using focused "or" expanded laser. Here two laser beams were showed together on one cell for the beam size comparison. (b) The thickness tuneable cell structure with two clips. The images of the cells with (c) focused laser for single-domain measurement and (d) expanded laser for dual-domain measurement.

based on the bright and dark states textures while the orientation of the cell is at 45° and 0° relative to the crossed polarizers. In Fig. 8.4a, the clear boundaries in the bright state texture showed that a dual-domain state was obtained in our cells. In cells prepared with a 1 mm or 2 mm domain width mask, the LC cells presented a uniform alignment in each domain (see stripes in Fig. 8.4a).

Furthermore, the pretilt angles were measured and analyzed by using the "crystal rotation method" (see Sec. 3.3.2) [25]. First, the geometrical construction of the pretilt angle direction and the pattern of the dual-domain system had to be described. In our substrate preparation setup (see Fig. 8.2c), the projection of the depositing direction onto the substrate is parallel to the short axis of the substrate (**x**-axis in Fig. 8.4b). According to this dual-domain substrate preparation method, the pretilt angle was in the **x**-**z** plane (see Fig. 8.4b). To investigate the pretilt angle change between each domain, we measured pretilt angles in different positions along the **y** direction. Fig. 8.4c was the result of the pretilt angle changes of 1 mm and 2 mm domain width cells for different positions **y**. Their measured areas are shown as red squares in Fig.

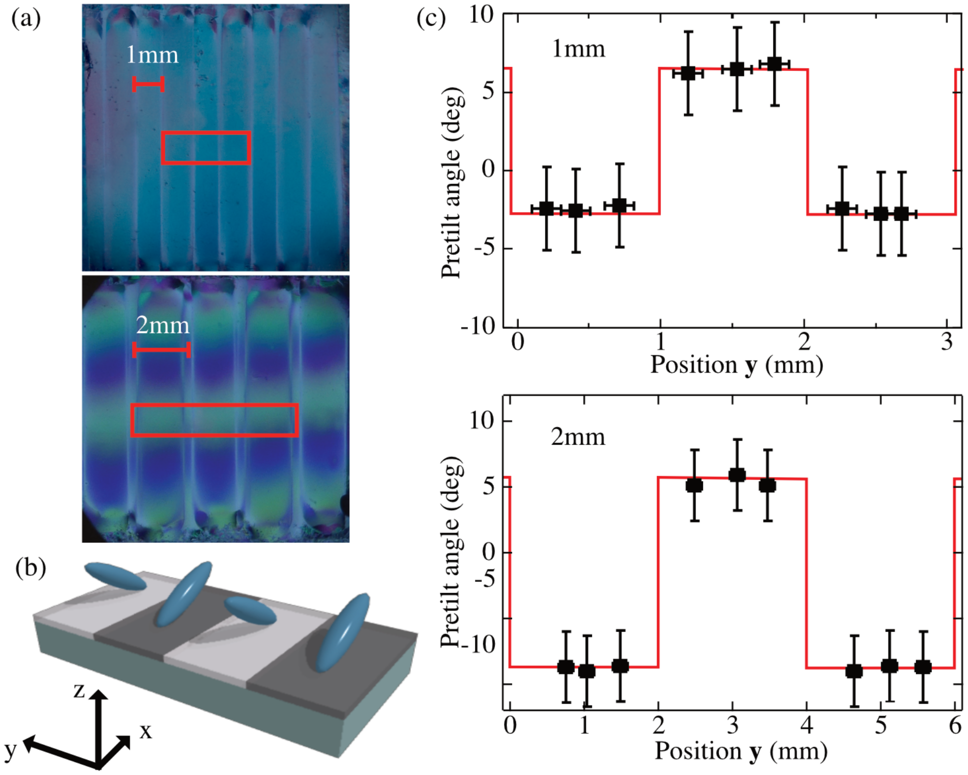

Figure 8.4: The pretilt angle in a dual-domain system. (a) POM images of cells with 1 mm and 2 mm domain widths. (b) Schematic diagram of the directions of LC molecules. (c) Pretilt angles at different positions of 1 mm and 2 mm domain width cells.

8.4a. The results showed that the pretilt angles were very uniform in each domain. Because of opposite Fe_2O_3/Cr_2O_3 depositing directions, the pretilt angles were in opposite directions in neighboring domains.[3]

We also tried to determine the pretilt angle in the boundary areas. However, the results could not be analyzed well. The possible reasons include (1) the measured area was not small enough which may contain two different pretilt angle domains and (2) top and bottom substrates (see Fig. 8.3a) may not be aligned perfectly which means that the pretilt angles on top and bottom were different in the boundary region. Compared to the domain width, the width of the boundary is very thin. The transmittance effect from the boundary region was neglected in this study.

---

[3] Fe_2O_3/Cr_2O_3 depositing directions were not really opposite (see Fig. 8.2b), but their projections

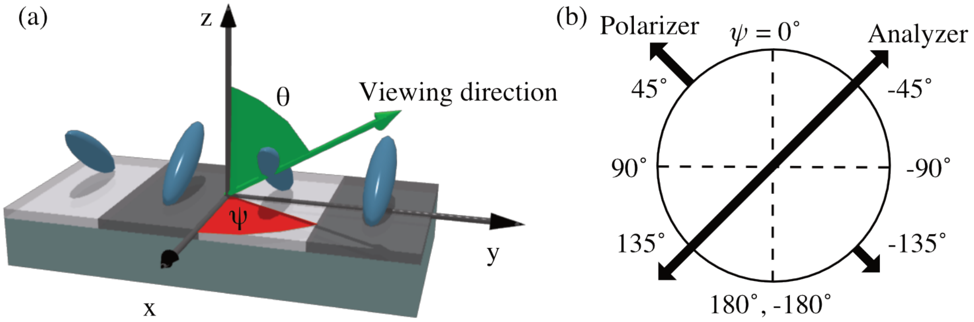

Figure 8.5: Schematic diagram of the definition of (a) the viewing direction (green arrow) at the azimuthal angle ψ and the polar angle θ. (b) Polarizer and analyzer directions and the azimuthal angle definition in the polar figure.

8.4 Viewing angle

In this section, the viewing angle dependence between single- and dual-domain were investigated and compared in two ways: (1) the transmittances in the bright and the dark states; (2) the contrast ratio. Before starting the discussion of the results, the viewing angle coordinates have to be explained. As shown in Fig. 8.5a, we defined the viewing angle in a spherical coordinate system using the polar angle θ (green plane) and the azimuthal angle ψ (red plane). Our cell had a mirror symmetry along the projection of the LC long axis on the substrate (defined as the x-axis). We defined the axes of symmetry as the azimuthal reference direction. The polar and azimuthal angles were restricted to the intervals $0^\circ \leq \theta \leq 90^\circ$ (see Fig. 8.5a) and $-180^\circ \leq \psi \leq 180^\circ$ (see Fig. 8.5b), respectively. In our setup, the cell was sandwiched between a pair of crossed polarizers. As shown in Fig. 8.5b, the polarizations of the polarizer and analyzer were at $\psi = 45^\circ$ and $\psi = -45^\circ$, respectively. In this chapter, all the viewing angle results were presented by polar figures with the azimuthal angle definition shown in Fig. 8.5b.

8.4.1 Transmittances in bright and dark states

Figure 8.6a shows the viewing angle dependence of the normalized transmittance in a single-domain cell. First, the transmittance, no matter in the bright or the dark state, has the same mirror symmetry along to the azimuthal angle $\psi = 0^\circ$ which is the pretilt angle direction. In the bright state (yellow polar figure), the high transmittance ($> 80\%$) is mostly located in the top area of the polar figure ($\psi = -90^\circ$ to 90°) because all LC molecules were aligned parallel to the pretilt angle which is in the plane $\psi = 0^\circ$

---

onto the substrate were opposite.

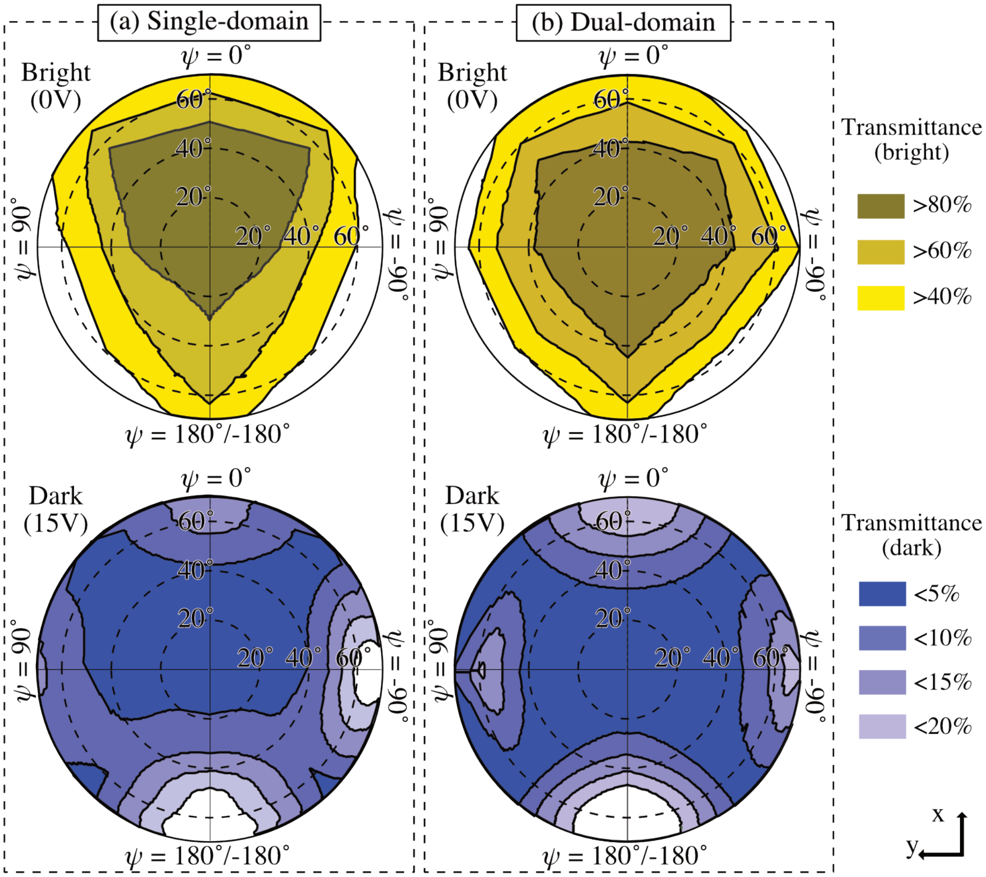

Figure 8.6: Measured polar figures of viewing angle dependences of transmittances in (a) single-domain and (b) dual-domain cells. The dashed circles are the polar angles and the ψ is the azimuthal angle (see the viewing angle definition in Fig. 8.5a). Top yellow and bottom blue polar figures are the measured transmittance of the bright state and the dark state, respectively.

(see the single-domain cell in Fig. 8.7a). If giving a high enough driving voltage, the LC molecules will be rotated along the external field direction which is perpendicular to the substrate. In this ideal case, the minimum transmittance will appear in the normal direction ($\theta = 0°$). Moreover, the transmittance of the dark state will be kept at 0 for the azimuthal angles $\psi = 45°$ and $-45°$ because no phase retardation is generated when the LC molecules are parallel to the polarizer direction (see Fig. 8.7b).

However, in the real case, not all LC molecules can be rotated to 90° with a 15 V driving voltage. Instead, the LC molecules will be rotated between the pretilt angle and 90°. For instance, if most of the LC molecules are rotated to 85°, the minimum of the transmittance will appear at $\theta = 5°$ and $\psi = 0°$ while the viewing direction is parallel to the LC molecules.[4] Therefore, the low-transmittance area ($< 5\%$) in the dark state in Fig. 8.6a (blue polar figure) is located in the top area.

Fig. 8.6b shows the viewing angle dependence of the normalised transmittance for a dual-domain cell. Comparing to the transmittances of the single-domain cell in Fig. 8.6a, the transmittance of the dual-domain cell is more uniform in both bright and dark states.[5] In the dark state, the dual-domain cell provided a large dark viewing angle ($T < 5\%$), especially for azimuthal angles $\psi = 45°/-135°$ and $\psi = -45°/135°$.

---

[4] Here we gave an example of an ideal LC director distribution. In general, the LC director is not uniform but varies between the pretilt angle and 90° between the substrate and the center of the cell, respectively.

[5] The transmittance was not perfectly symmetric in the azimuthal angles $\psi = 0°$ and $\psi = 180°$ because the pretilt angles were not exactly the same in the two domains. As the 2 mm domain width cell shown in Fig. 8.4c, the pretilt angles were $\sim 9°$ and $\sim 6°$ in position regions 0∼2 mm and 2∼4 mm, respectively.

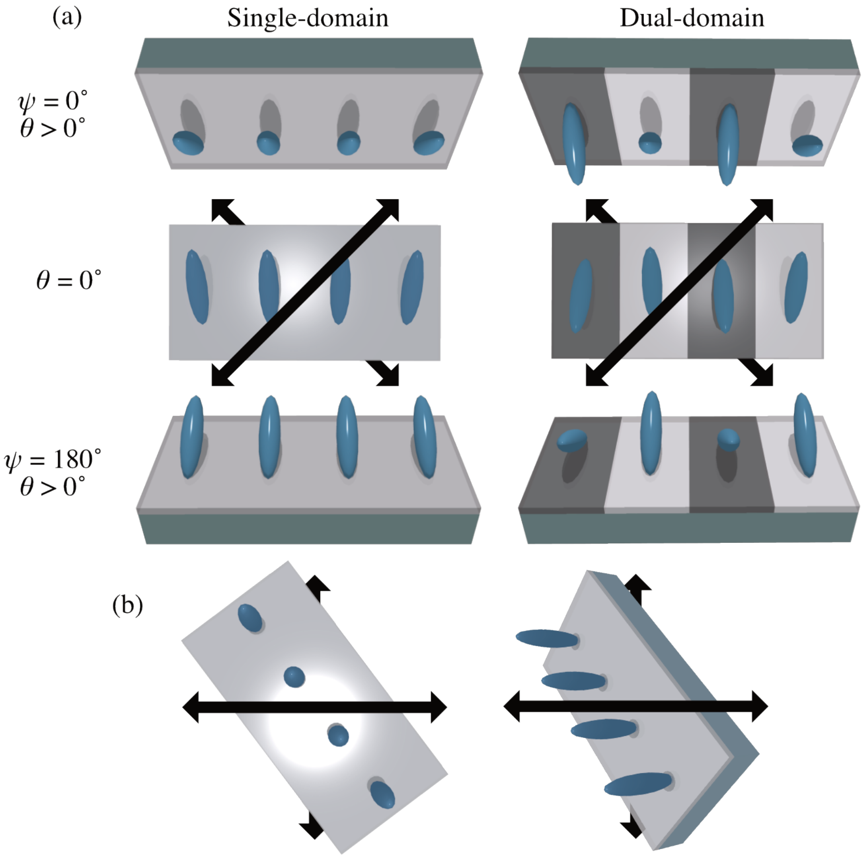

Figure 8.7: (a) Single- and dual-domain cells for the azimuthal angles $\psi = 0^\circ$ and 180°. The symmetry of the dual-domain cell can compensate the viewing angle dependence in the azimuthal angle $\psi = 0^\circ$ and 180°. (b) A normal and $\psi = 45^\circ$ views. In an ideal dark state, the transmittance stays at 0 for the azimuthal angle $\psi = 45^\circ$ because the LC director is always parallel to the polarizer or the analyzer.

8.4.2 Contrast ratio

The viewing angle dependence is generally given by the angle range for a contrast ratio larger than 10 or 50. In our case, the contrast ratio (CR) can be obtained by the following equation:

$$\mathrm{CR} = \frac{T(\text{Bright state})}{T(\text{Dark state})} = \frac{T(0\ \mathrm{V})}{T(V_d)} \tag{8.1}$$

Here, $T(0\ \mathrm{V})$ is the transmittance at a 0 V driving voltage which gives the bright state. $T(V_d)$ is the transmittance at a V_d driving voltage which gives the dark state. In this section, we gave a driving voltage of 15 V or 20 V for the dark state.[6]

Figure 8.8a gives the contrast ratio polar figures of single- and dual-domain cells with a 15 V driving voltage for the dark state. In the single-domain cell, the high contrast ratio (> 50) is located in the top part of the polar figure. Comparing the transmittances of the bright and the dark states (see Fig. 8.6a), this can be explained because the high transmittance area of the bright state and the low transmittance area of the dark state both appeared in the top regions of the polar figures. As shown in the bottom part of Fig. 8.8a, the dual-domain cell provided a wider and more symmetric contrast ratio distribution. In particular, the dual-domain cell had a wider viewing angle, especially for the azimuthal angles $\psi = 45°/-135°$ and $-45°/135°$. In general, people watch a TV in the same horizontal place. So an LCD TV can be designed by setting the polarizer or analyzer horizontally to achieve a larger viewing angle (see Fig. 8.7b).

In an ideal case when all LC molecules align vertically to the substrate in the dark state, the transmittance is 0 at the azimuthal angles $\psi = 45°/-135°$ and $\psi = -45°/135°$. In other words, the contrast ratio, which is inversely proportional to the transmittance of the dark state, is infinitely large at the azimuthal angles $\psi = 45°/-135°$ and $\psi = -45°/135°$. However, for a real case of a cell with a 15 V driving voltage, not all the LC molecules align to 90°, especially in the boundary regions. To achieve a higher contrast ratio and wider viewing angle, the LC molecules have to be rotated more close to 90° by giving a higher driving voltage or applying a higher dielectric anisotropy constant $\Delta\epsilon$ LC. Figure 8.8b shows that a 20 V driving voltage cell has a wider viewing angle. Especially in the dual-domain cell at the azimuthal angles $\psi = 45°/-135°$ and $-45°/135°$, the high contrast ratio region ($CR > 50$) almost covered our measured area ($\theta \leq 70°$).

---

[6] we applied a 1 KHz squared wave with a V_d peak to peak voltage.

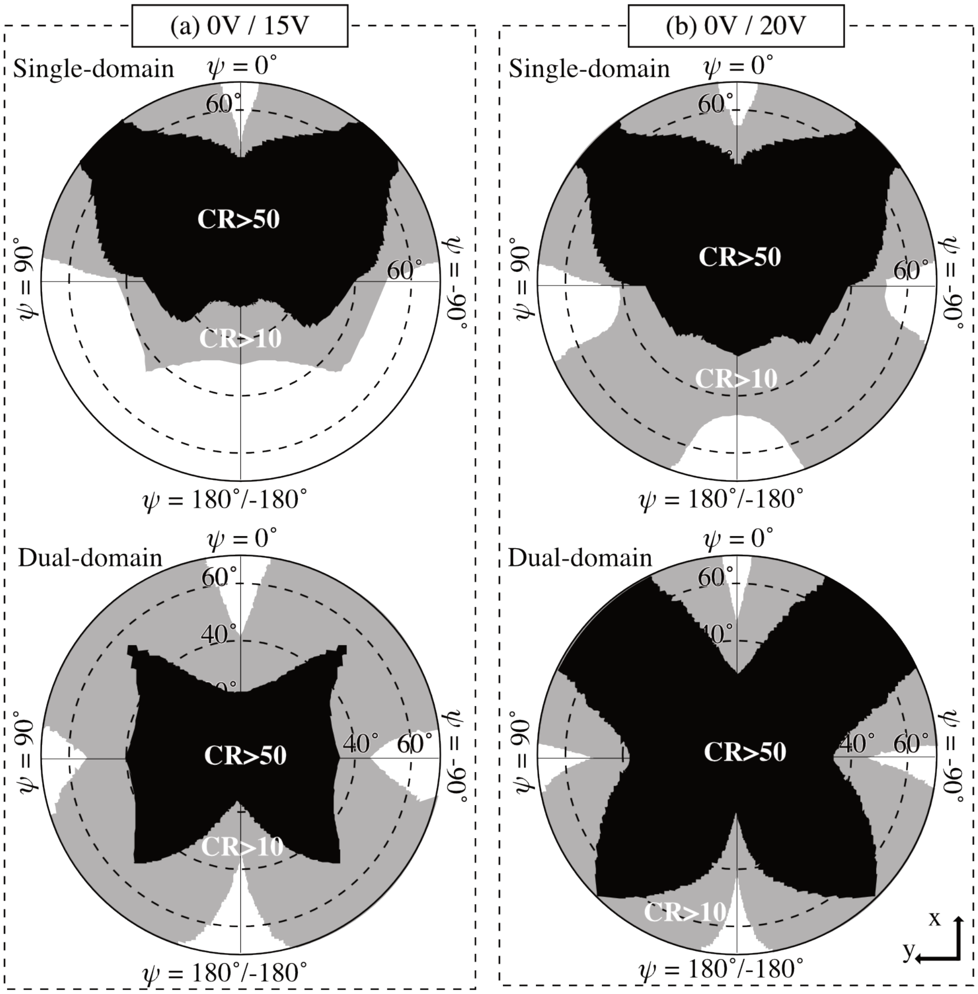

Figure 8.8: Polar figures of the measured contrast ratio of the single- and dual-domain cells for (a) bright state at 0 V / dark state at 15 V and (b) bright state at 0 V / dark state at 20 V. The dashed circles are the polar angles and the ψ is the azimuthal angle (see the viewing angle definition in Fig. 8.5a). The black and gray areas are the viewing angle with a contrast ratio larger than 50 and 10, respectively.

8.5 Conclusion

We demonstrated a dual-domain method by combining film deposition and shadow mask lithography technologies. By using different Fe_2O_3/Cr_2O_3 depositing directions with selected shadow masks, an LC cell presented a uniform alignment in each domain and opposite pretilt angles compared with neighboring domains. In the transmittances measurement, the dual-domain cell was uniform in both the bright and the dark states. Moreover, in the dark state, the dual-domain cell provided a large dark viewing angle.

In general, the viewing angle was defined as the angle region with a contrast ratio larger than 10. In the contrast ratio study, we found that the dual-domain cell provided a wider and more symmetric contrast ratio distribution. Especially in the dual-domain cell for azimuthal angles $\psi = 45^\circ/-135^\circ$ and $-45^\circ/135^\circ$, the high contrast ratio region ($CR > 50$) almost covered our measured area ($\theta < 70^\circ$) with a 20 V driving voltage. By setting the polarizer or analyzer horizontally, a larger viewing angle LCD was achieved by a dual-domain system.

References

[1] H.-S. Kwok, S. Naemura, and H. L. Ong, *Progress in Liquid Crystal Science and Technology*, In Honor of Shunsuke Kobayashi's 80th Birthday (World Scientific, 2013).

[2] T. Ishinabe, K. Kusama, and S. Shoshi, ITE Transactions on Media Technology and Applications **4**, 34 (2016).

[3] H. Takemoto, T. Fuchida, and M. Miyatake, SID Symposium Digest of Technical Papers **40**, 514 (2009).

[4] Y.-J. Wang, J.-G. Lu, W.-C. Chao, and H.-P. D. Shieh, Optics express **23**, 21443 (2015).

[5] K. Takatoh, M. Hasegawa, M. Koden, N. Itoh, R. Hasegawa, and M. Sakamoto, *Alignment Technology and Applications of Liquid Crystal Devices* (CRC Press, 2005).

[6] E. Yamamoto, H. Yui, S. Katsuta, Y. Asaoka, and T. Maeda, in *SID* (SID, 2014) pp. 385–388.

[7] K. Koike, S. Takaoka, T. Sasaki, H. Chida, H. Tsuda, A. Takeda, and K. Ohmuro, Proceedings of AM-LCD , 25 (1997).

[8] A. Takeda, S. Kataoka, T. Sasaki, H. Chida, H. Tsuda, K. Ohmuro, K. Koike, and K. Okamoto, SID Symposium Digest of Technical Papers **29**, 1077 (1998).

[9] Y. Koike and K. Okamoto, Fujitsu Science Technical Journal **35**, 221 (1999).

[10] Y. Koike, T. Kamada, K. Okamoto, M. Ohashi, I. Tomita, and M. Okabe, SID92 DIGEST **23**, 798 (1992).

[11] M. Schadt, H. Seiberle, and A. Schuster, Nature (1996).

[12] Y.-K. Moon, Y.-J. Lee, C.-J. Yu, J. Uk Heo, J.-H. Park, H. jin Lee, S. Tae Shin, and J.-H. Kim, Journal of Applied Physics **112**, 014512 (2012).

[13] C. Mauguin, Bulletin de la Société Française de Minéralogie et de Crystallographie **34**, 71 (1911).

[14] M. K. Ghosh and K. L. Mittal, *Polyimides: fundamentals and applications* (CRC Press, 1996).

[15] J. L. Janning, Applied Physics Letters **21**, 173 (1972).

[16] T. Uchida, M. Ohgawara, and M. Wada, Japanese Journal of Applied Physics **19**, 2127 (1980).

[17] L. A. Goodman, J. T. McGinn, C. H. Anderson, and F. DiGeronimo, Electron Devices, IEEE Transactions on **24**, 795 (1977).

[18] A. Tixier, Y. Mita, J. P. Gouy, and H. Fujita, Journal of Micromechanics and Microengineering **10**, 157 (2000).

[19] P. Chaudhari, J. Lacey, J. Doyle, E. Galligan, S. Lien, J. Lacey, J. Doyle, E. Galligan, S.-C. A. Lien, A. Callegari, G. Hougham, N. D. Lang, P. S. Andry, R. John, K.-H. Yang, M. Lu, C. Cai, J. Speidell, S. Purushothaman, J. Ritsko, M. Samant, J. S. hr, Y. Nakagawa, Y. Katoh, Y. Saitoh, K. Sakai, H. Satoh, S. Odahara, H. Nakano, J. Nakagaki, and Y. Shiota, Nature **411**, 56 (2001).

[20] H.-Y. Wu and R.-P. Pan, Applied Physics Letters **91**, 074102 (2007).

[21] Y. Kajiyama, K. Joseph, K. Kajiyama, S. Kudo, and H. Aziz, SPIE Organic Photonics + Electronics **8829**, 882919 (2013).

[22] J. Ma, R. Sun, X. Liu, X. Lu, L. Hu, and L. Xuan, Displays (2012).

[23] T. Scharf, *Polarized Light in Liquid Crystals and Polymers* (John Wiley & Sons, 2007).

[24] I. Dierking, *Textures of Liquid Crystals* (John Wiley & Sons, 2006).

[25] T. J. Scheffer and J. Nehring, Journal of Applied Physics **48**, 1783 (1977).

CHAPTER 9

Summary

Liquid crystal displays (LCDs) are widely used in modern life. Over the past few decades, many LCD modes, such as the twisted nematic (TN), the in-plane switching (IPS) and the vertical alignment (VA) modes, have been developed to achieve higher LCD performances. The increasing range of applications of LCD's continuously fuels the search to further improve their performance characteristics, such as faster response time for video rate applications. The contrast ratio, the response time, and the viewing angle are the three main LCD performance parameters discussed in this thesis.

In this thesis, we presented experimental and theoretical studies of how the LCD performance depends on and can be controlled by the pretilt angle, where the pretilt angle is defined as the angle between the substrate and the average long axis of the liquid crystal (LC) molecules in the surface layer. A faster response time and a wider viewing angle were achieved by preparing a dual-domain parallel alignment cell with a controllable LC pretilt angle.

The related background knowledge is introduced in Ch. 2 and 3. In Ch. 2, the basic properties of LCs and LCD technologies are introduced. In Ch. 3, all the sample and substrate preparation procedures, the experimental setups and the analytical methods we used are described.

In Ch. 4, we demonstrated a new pretilt angle controlling surface treatment method by introducing an obliquely deposited Fe_2O_3/Cr_2O_3 thin film on polyimide-coated indium tin oxide (ITO) substrates. Pretilt angles between 0° and 45° were obtained by finely tuning the Fe_2O_3/Cr_2O_3 deposition time. The two main param-

eters of the pretilt angle control were determined: (1) the Fe_2O_3/Cr_2O_3 deposition time and (2) oblique deposition. Furthermore, the concept of the electric potential energy was used to investigate the relation between the pretilt angle and the sputtering conditions.

Ch. 5 focused on the investigation of the surface LC alignment effects of Fe_2O_3/Cr_2O_3 and polyimide layers. First, atomic force microscopy (AFM) images showed the roughed surface of Fe_2O_3/Cr_2O_3, but no grooves or specific surface shapes were found on the surface. A significant correlation was found between the pretilt angle and the surface roughness. X-ray photoemission spectroscopy (XPS) was used for surface chemical analysis. By comparing the experimental Fe $2p_{3/2}$ and Cr $2p_{3/2}$ XPS peaks and the data from literature, the deposited thin film from the stainless steel sputtering was identified as 75% Fe_2O_3 / 25% Cr_2O_3. Here, only the AFM results showed explicitly a linear correlation between the pretilt angle and the roughness squared.

In Ch. 6, the experimental results led to several interesting findings, which can be used to improve LCD performances. The threshold voltage, which influences the LC static and dynamic properties, decreased with increasing pretilt angle. A cell with an optimum pretilt angle of 27° had a two times higher contrast ratio of 116:1 and three times faster turn on time of 0.2 ms compared to a cell with a low pretilt angle of 1°.

In Ch. 7, we presented a new calculation method for the LC static and dynamic studies for a full range of LC director orientation and pretilt angle. The new improved calculation method resulted in a much better agreement with the simulation results in comparison to an existing calculation method that uses a small tilt angle approximation. The calculation results are in good agreements with the experimental data and provide the explanations of specific LCD properties, such as an optical time delay found in a turn on time study.

In Ch. 8 we demonstrated a dual-domain system by combining film deposition and shadow mask lithography technologies and found that the dual-domain cell provided a wider and more symmetric contrast ratio distribution than the single-domain cell.

In summary, in this thesis, we presented a new surface treatment technology which can control the LC pretilt angle precisely and which led to a fast turn off time of 9 ms and turn on time of 0.2 ms. By combining it with the shadow mask technology, a dual-domain LC control was achieved that provided a very wide viewing angle with a high contrast ratio. Since sputtering deposition and shadow mask are well known and mature techniques, our results present the ingredients for a new technology that requires fewer fabrication steps in comparison with the more complicated lithography processes.

CHAPTER 10

Samenvatting

Liquid Crystal Displays (LCD's) zijn wijdverbreid in gebruik in de moderne wereld. In vergelijking met de ouderwetse beeldbuizen werkend op cathode ray tubes (CRT's) zijn er enorme voordelen voor LCD's: LCD's zijn dunner in afmetingen, lichter in gewicht en verbruiken minder energie. Daardoor maken LCD's meer toepassingen mogelijk, zoals het gebruik in draagbare apparaten. In de afgelopen decennia zijn vele LCD concepten ontwikkeld, zoals Twisted-Nematic (TN), In-Plane-Switching (IPS) en Vertical-Alignment (VA), met het doel om betere LCD eigenschappen te bereiken. Omdat het aantal toepassingen blijft toenemen is er ook een blijvende interesse en noodzaak om de eigenschappen van LCD's te verbeteren, zoals snellere schakeltijden voor video toepassingen. Drie belangrijke eigenschappen van LCD's werden behandeld in dit proefschrift: de contrast verhouding, de reactie tijd en de zichbaarheids-hoek. In het bijzonder werden theoretische en experimentele studies beschreven hoe de LCD eigenschappen afhangen van de orientatie hoek die de vloeibare kristal (liquid crystal) moleculen maken ten opzichte van het oppervlak van het substraat.

In hoofdstuk 2 en 3 werd de relevante achtergrond kennis gentroduceerd. Hoofdstuk 2 behandelde de basis-eigenschappen van vloeibare kristallen en de LCD technologie. In hoofdstuk 3 werden de procedures voor het geschikt maken van preparaten en vloeibare kristal materialen beschreven, alsmede de experimentele opstellingen en de gebruikte analyse methodes.

In hoofdstuk 4 werd een nieuwe manier geintroduceerd om de orientatie hoek van de moleculen te controleren via de depositie van een dunne Fe_2O_3/Cr_2O_3 laag op een indium tin oxide (ITO) oppervlak met polyimide coating. Verschillende orientaties tussen 0 en 45 graden werden verkregen door de precieze afstemming van de Fe_2O_3/Cr_2O_3 depositie tijdsduur.

Hoofstuk 5 geeft de karakterisatie van het oppervlak van de Fe_2O_3/Cr_2O_3 en polyimide lagen met behulp van X-ray photoemissie (XPS) en atomaire kracht microscopie. Er werd een duidelijke relatie gevonden tussen de orientatie hoek van de vloeibare kristal moleculen en de ruwheid van het oppervlak.

In hoofdstuk 6 werden de statische en dynamische eigenschappen van de LC materialen besproken als functie van de vloeibare kristal orientatie hoek. We vonden een hoger contrast en snellere reactietijd tot 0.2 msec bij een hogere orientatie-hoek.

In hoofdstuk 7 werd een nieuwe berekeningsmethode beschreven voor de statische en dynamische LCD studies voor willekeurige waarden van de orientatie-hoek. De nieuwe berekeningsmethode komt beter overeen met de simulaties dan de bestaande berekeningsmethode die gebruik maakt van een kleine-hoek benadering, zowel voor de statische als ook voor de dynamische eigenschappen.

Een “twee-domein” materiaal fabricage methode werd voorgesteld in hoofdstuk 8: deze techniek leidt tot een wijdere en meer symmetrische contrast verhouding dan de gebruikelijke een-domein structuur.

Samenvattend beschreef dit proefschrift een nieuwe oppervlakte behandeling, die de vloeibare kristal molecuul orientatie hoek (pretilt-angle) nauwkeurig kan controleren. Dit leidt tot snellere aan-uit schakeltijden voor een vloeibare kristal cel (0.2 msec resp. 9.0 msec). Verder werd een wijdere zicht-hoek (viewing-angle) en hoger contrast bereikt. De resultaten leveren ingredienten voor een nieuwe LCD technologie.

List of Publications

Control of Liquid Crystal Pretilt Angle by an Obliquely Deposited Fe_2O_3/Cr_2O_3 Thin Film on Polyimide
W.-T. Wu, M.-C. Huang, C.-W. Lai, C.-Y. Tai, L. Cattaneo, R.-P. Pan, and Th. Rasing (submitted).

Effect of Pretilt Angle on Liquid Crystal Contrast Ratio and Dynamics
W.-T. Wu, C.-Y. Tai, C.-W. Lai, M.-C. Huang, L. Cattaneo, R.-P. Pan, and Th. Rasing (submitted).

Dual-domain Parallel Alignment LCD by Film Deposition with Shadow Mask
W.-T. Wu, C.-Y. Tai, C.-W. Lai, M.-C. Huang, L. Cattaneo, R.-P. Pan, and Th. Rasing (in preparation).

A Novel Numerical Method for Investigating Pretilt Angle Effect on LCD Properties
W.-T. Wu, R.-P. Pan, and Th. Rasing (in preparation).

Curriculum Vitae

Name:
Wei-Ta Wu

Date of birth:
February 27, 1984

Place of birth:
Changhua, Taiwan

2002-2007	B.Sc. studies at the Department of Physics, National Tsing Hua University, Hsinchu, Taiwan.
2007-2009	M.Sc. studies at the Department of Electrophysics, National Chiao Tung University, Hsinchu, Taiwan. Supervisor: Prof. dr. Ru-Pin Pan.
2009-2011	Graduate studies at the Department of Electrophysics, National Chiao Tung University, Hsinchu, Taiwan. Supervisor: Prof. dr. Ru-Pin Pan.
2011-2016	Ph.D. studies at Radboud University Nijmegen, the Institute for Molecules and Material, The Netherlands. Supervisor: Prof. dr. Theo Rasing and Prof. dr. Ru-Pin Pan.